
Quantitative Cell Migration in 3D Compliant Hydrogel Microenvironments

Stefan Stöberl



München 2024

Quantitative Cell Migration in 3D Compliant Hydrogel Microenvironments

Stefan Stöberl

Dissertation
an der Fakultät für Physik
der Ludwig-Maximilians-Universität
München

vorgelegt von
Stefan Stöberl
aus Peißenberg

München, den 17.05.2024

Erstgutachter: Prof. Dr. Joachim O. Rädler
Zweitgutachter: Prof. Dr. Chase P. Broedersz
Tag der mündlichen Prüfung: 09.07.2024

Quantitative Zellmigration in 3D Deformierbaren Hydrogel Mikrostrukturen



Dissertation
an der Fakultät für Physik
der Ludwig-Maximilians-Universität
München

vorgelegt von
Stefan Stöberl
aus Peißenberg

München, den 17.05.2024

Zusammenfassung

Die Zellmigration ist ein fundamentaler Prozess in verschiedenen physiologischen Vorgängen, einschließlich Immunreaktionen, Wundheilung und Krebsmetastasen. In diesen Kontexten navigieren Zellen durch schmale Verengungen innerhalb der extrazellulären Matrix (EZM). In Modellen aktiver weicher Materie wird die Migration über Barrieren hinweg diskutiert. Insbesondere die Rolle des Zellkerns, als großes und steifes Organell, hat zunehmende Aufmerksamkeit als limitierender Faktor bei der Migration in engen Räumen erhalten. Vorherige Studien haben gezeigt, dass Zellen durch mikrostrukturierte Oberflächen geleitet werden können. Die Dynamik von Zellen in 2D-Hantelstrukturen kann gut durch abgeleitete Bewegungsgleichungen erfasst werden. Unter physiologischen Bedingungen migrieren Zellen jedoch typischerweise in dreidimensionalen physischen Verengungen. Dies führt zu laufenden Diskussionen über die Dynamik in 3D-Strukturen und die Mechanismen, durch die Zellen ihre Kern-Eigenschaften und Kraftgenerations-Maschinerie regulieren, um räumliche Verengungen zu überwinden.

In dieser Arbeit haben wir photolithografische Mikrofabrikationstechniken verwendet, um künstliche experimentelle Plattformen zur Untersuchung der Zellmigration in engen Räumen zu erstellen. In einer ersten Studie haben wir Hydrogel-Hydrogel-Grenzflächen, genannt 'Schwammklemmen', konstruiert, um die Invasionsdynamik von Zellen zwischen verformbaren Wänden zu untersuchen. Unsere Ergebnisse zeigten bemerkenswerte Unterschiede in der Invasionsgeschwindigkeit von Krebszelllinien in Abhängigkeit von der Spaltgröße und der Steifigkeit des Hydrogels. Im nächsten Schritt fertigten wir hantelförmige Hohlräume an, um repetitive Zellmigration durch 3D-Verengungen mit definierten Breiten zu studieren. Wir sammelten Statistiken von Hunderten Zelltrajektorien in angeordneten Hanteln und beobachteten, dass in breiten Kanälen sowohl die Übergangsraten als auch die Kern-Geschwindigkeiten mit Verschmälerung der Kanalbreite zunahmten, während die Migration bei subnuklearer Verengung behindert wurde. Um die mechanischen Eigenschaften des Zellkerns als limitierender Faktor bei der Migration in engen Räumen weiter zu erläutern, bestimmten wir den Elastizitätsmodul und die Formveränderung des Zellkerns innerhalb der hantelförmigen Hohlräume. Wir stellten sowohl vorübergehende Verformungen in oblate als auch in prolate Formen fest, zusammen mit Kernvolumenreduktionen während der Transmigration, bestimmt mithilfe konfokaler Bildgebung. Zusätzlich analysierten wir die von dem Zellkern auf die nachgiebigen Hydrogel-Wände ausgeübten Kräfte unter Verwendung von Verschiebungsfeldern eingebetteter Markerkugeln. Die gemessene Kernmorphologie in Abhängigkeit von der Breite der Verengung bildete die Grundlage für ein theoretisches Modell, das in der Broedersz-Gruppe entwickelt wurde. Die Analyse liefert eine quantitative Bewertung des Gleichgewichts zwischen Zug- und Druckkräften und deutet auf eine Anpassung der zellulären Kraftgeneration in Abhängigkeit der Verengung hin.

Insgesamt unterstreichen unsere Ergebnisse die Wirksamkeit und Vielseitigkeit von 3D-mikrofabrizierten Zellmigrations-Assays, die weiche Hydrogel-Architekturen nutzen, für die Untersuchung der Zellmechaniken.

Summary

Cell migration is a key process in various physiological settings, including immune responses, wound healing, and cancer metastasis. In these contexts, cells navigate through narrow constrictions within the extracellular matrix (ECM). In active soft matter models, the migration across barriers is under debate. In particular the role of the cell nucleus, as a large and stiff organelle, has received increasing attention as a rate-limiting factor in confined cell migration. Previous studies have shown that cells can be guided by micro-patterned surfaces. The dynamics of cells in 2D dumbbell pattern is well captured by inferred equations of motion. However, under physiological conditions, cells typically migrate in 3D physical confinement. This prompts ongoing discussions regarding the dynamics in 3D pattern and the mechanisms by which cells regulate their nuclear properties and force generation machinery to overcome spatial constrictions.

In this thesis, we utilized photo-lithographic microfabrication techniques to cast artificial experimental platforms for the study of cell migration in confinement. In a first study, we generated hydrogel-hydrogel interfaces, termed 'sponge clamps', to investigate cell invasion dynamics between deformable walls. Our results revealed notable differences in the invasion velocity of cancerous cell lines as a function of gap size and the stiffness of the hydrogel. In a next attempt, we fabricated dumbbell-shaped cavities to study repeated cell migration across 3D-constrictions with defined widths. We collected statistics from hundreds of cell trajectories in arrayed dumbbells and observed that in wider channels, both the rates of transition and nuclear velocities increase with confinement, while migration is impeded for sub-nuclear confinement. To further elucidate the mechanical aspects of the nucleus's role as a limiting factor in confined cell migration, we assessed the elastic modulus and the shape deformation of the nucleus within the dumbbell-shaped cavities. We discovered both transient deformation into oblate as well as prolate shapes along with nuclear volume reductions during transmigration as determined by confocal microscopy. Additionally, we evaluated the forces exerted by the nucleus onto compliant hydrogel walls using displacement fields of embedded marker beads. The measured nuclear morphology as a function of confinement presented the basis for a theoretical model developed by the Broedersz group. The analysis yielded a quantitative assessment of the balance between pulling and pushing forces and suggest a cellular force generation adaptation in response to confinement.

Overall, our findings highlight the efficacy and versatility of 3D-microfabricated cell migrations assays utilizing soft hydrogel architectures for the study of cell mechanics.

Contents

Zusammenfassung	i
Summary	iii
List of Publications	vii
1 Introduction	1
2 Fundamental Concepts	5
2.1 Cell Migration	5
2.1.1 Role of the Cytoskeleton and Cellular Adhesion Machinery . .	5
2.1.2 Cellular Migration Modes	7
2.1.3 Impact of 3D Confinement on Cell Migration	8
2.1.4 Guidance Mechanisms of Cell Migration	10
2.2 Theoretical Description of Cell Migration	12
2.2.1 Persistent Random Walk	13
2.2.2 Data-Driven Top-Down Approaches	13
2.2.3 Bottom-Up Mechanistic Cell Migration Models	14
2.3 Mechanics of the Cell Nucleus	15
2.3.1 Physical and Biological Properties	16
2.3.2 Mechanisms of Cellular Force Generation	17
2.3.3 Nucleus as an Internal Ruler	18
2.4 Microfabrication of Biomimetic Materials	20
2.4.1 2D and 3D Experimental Platforms	21
2.4.2 Synthetic and Naturally Derived Hydrogels	22
2.4.3 Different Microfabrication Techniques	24
2.5 Elasticity and Rheology of Extended Bodies	26
2.5.1 General Concepts	27
2.5.2 Poisson Ratio	30
2.5.3 Contact Mechanics and Hertz Model	32
3 Experimental Methods	35
3.1 Polymerization of PEG-NB Hydrogels	35
3.2 Light Microscopy	36
3.3 Atomic Force Microscopy	38

4	Cell Invasion Studies in Synthetic Hydrogel Clefts	41
4.1	Fabrication of Pressurized Migratable Hydrogel Clefts	41
4.2	Characterization of Hydrogel Swelling and Contact Profiles	43
4.3	Invasion Capacity in Hydrogel Clefts	45
4.4	Discussion	49
5	Migration of Cells in Dumbbell-shaped Hydrogel Cavities	51
5.1	Microfabrication of Hydrogel-Based 3D Assays	52
5.2	Cell Dynamics in 3D Confinement	54
5.3	Inferred Non-Linear Dynamics of the Nucleus	58
5.4	Discussion	60
6	Mechanical Properties of Cell Nuclei in Compliant Constrictions	63
6.1	Nuclear Shape Recovery of a Cancerous Cell Line	64
6.2	Quantitative Nuclear Volume Analysis	65
6.3	Analysis of the Indentation of Hydrogel Walls	68
6.4	Discussion	73
7	Adaptive Cellular Force Generation in Physical Confinement	75
7.1	Nuclear Shape Analysis Indicate Pulling and Pushing Forces	76
7.2	Perturbation of Pulling Force Generation	79
7.3	Quantification of the Cytosolic Calcium Levels	82
7.4	Modification of Actomyosin Contractility	82
7.5	Mechanistic Model for the Adaptation of Cellular Forces	85
7.6	Discussion	87
8	Conclusion and Outlook	91
A	Materials and Methods	95
A.1	Microfabrication of Hydrogel-Based Structures	95
A.2	Cell Culture	96
A.3	Transfection Procedure	97
A.4	Time-Lapse Microscopy	98
A.5	Stiffness Evaluation via AFM	99
B	Image and Data Analysis	101
B.1	Microscopy and Cell Tracking	101
B.2	Measurement of the Hydrogel-Hydrogel Gap Width	101
B.3	Cell Exclusion Criteria in 3D Dumbbells	101
B.4	Bead Displacement Analysis	102
B.5	Calcium Level Analysis	102
B.6	Nuclear Growth Analysis	102
B.7	Collected Cell Statistics	103
	Bibliography	111
	Danksagung	136

List of Publications

1. **Stefan Stöberl**, Miriam Balles, Thomas Kellerer, Joachim O. Rädler* (2023). *Photolithographic microfabrication of hydrogel clefts for cell invasion studies. Lab on a Chip*, 23, 1886-1895. DOI: 10.1039/D2LC01105K.
2. Johannes Flommersfeld, **Stefan Stöberl**, Omar Shah, Joachim O. Rädler, Chase P. Broedersz* (2024). *Geometry-Sensitive Protrusion Growth Directs Confined Cell Migration. Physical Review Letters* 132.9, 098401. DOI: 10.1103/PhysRevLett.132.098401.
3. **Stefan Stöberl**[†], Johannes Flommersfeld[†], Maximilian M. Kreft, Martin Benoit, Chase P. Broedersz*, Joachim O. Rädler* (2024). *Nuclear deformation and dynamics of migrating cells in 3D confinement reveal adaptation of pulling and pushing forces*. Manuscript under revision (**Science Advances**). Preprint uploaded to bioRxiv, DOI: 10.1101/2023.10.30.564765

[†] These authors contributed equally to this work.

1. Introduction

Cell migration is a fundamental process in various physiological settings within the human body. For instance, fibroblasts migrate towards wound sites, where they perceive and respond to environmental signals, thereby facilitating the secretion of extracellular matrix (ECM) proteins and subsequent cellular proliferation [1]. Furthermore, immune cell migration serves as a pivotal process in the immune response against infection. To effectively tackle pathogens, immune cells must migrate from the bloodstream to the specific sites of infection [2]. Nonetheless, the migratory behavior of cells can lead to significant risks to organisms, particularly when cancer cells undergo transitions to a migratory phenotype [3]. This transition often leads to the formation of cancer metastasis, which are responsible for the majority of cancer-related deaths [4]. Thus, comprehending and predicting cellular migration behavior may prove pivotal in the advancement of more effective treatments. In this context, it becomes particularly crucial to acknowledge the complex environment traversed by cells within the organism, encompassing both chemical and mechanical gradients.

The investigation of the fundamental mechanisms underlying cell migration has prompted increased attention towards appropriate experimental systems. Over the last decades, considerable efforts have been directed towards the development of 2D experimental setups. Utilizing micro-structuring techniques have yielded extensive datasets characterizing cell behavior, thereby facilitating the modeling and assessment of spatio-temporal regulatory mechanisms at the cellular and molecular levels. Substantial progress has been achieved in comprehending the processes, that guide cell migration on 2D substrates [5–7]. Despite these notable advancements, there is an increasing acknowledgment, that 2D substrates inadequately capture the multifaceted nature of the *in vivo* environment [8, 9]. The chemical microenvironment traversed by cells *in vivo* constitutes a complex interplay of extracellular matrix (ECM) proteins, proteoglycans, growth factors, and signaling molecules [10]. The physical properties of the ECM environment are governed by the interaction among these diverse components. Furthermore, it can manifest as fibrillar, porous, soft, rigid, or viscoelastic structures, each of which significantly influences cell migration in a manner not accurately replicated in 2D experimental setups. Hence, such discrepancies elucidate the distinctions between findings from 2D and 3D assays [11]. Arising from the imperative to closely replicate *in vivo* conditions, there has been growing emphasis on the development of 3D experimental setups in recent years [12]. Consequently, naturally derived hydrogels, such as collagen or Matrigel, have emerged as widely adopted biomimetic substrates in 3D cell culture and microenvi-

ronment engineering, owing to their inherent advantageous characteristics, including bio-compatibility and facilitation of cell adhesion [13–15]. Nonetheless, limitations of these naturally derived hydrogels encompass their heterogeneous network structure characterized by variable mesh sizes, formed fibers, and batch-to-batch variability [16]. In response to these challenges, synthetic hydrogels have garnered increased attention in recent decades [17]. These hydrogels are fabricated through synthetic chemistry, involving the cross-linking of bioinert chemical monomers, such as poly(ethylene glycol) (PEG) and poly(acrylamide) (PA) [18]. Despite potentially mimicking less physiological conditions, synthetic hydrogels offer precise control over their biophysical properties and exhibit reproducibility, which contrasts favorably with naturally derived hydrogels [12]. These advantages were exploited to investigate cell invasion within well-defined and reproducible 3D environments, reasonably mimicking physiological conditions [19–21].

Over the last two decades, an increasing number of studies have used the versatility of such developed experimental platforms to investigate the impact of confinement on cell migration dynamics. Studies have demonstrated, that the width of confinement, coupled with the stiffness of the surrounding environment, can induce changes in the migration phenotype of cancer cells [22]. Furthermore, it has been observed, that cells possess a tendency to migrate and accelerate into narrow 2D confinements [23]. This phenomenon is particularly relevant in physiological contexts, wherein cells commonly encounter spatial constrictions while invading their natural ECM. However, for cells to navigate through narrow 3D constrictions, the nucleus, as largest and stiffest organelle, assumes a pivotal role [24]. Investigations have revealed, that in scenarios, where nuclear deformation is required, the translocation of the nucleus emerges as the bottleneck in the migration process [25–27]. Initially, the role of the nucleus in confined migration was primarily reduced as that of a passive cargo, wherein its viscoelastic properties play a pivotal role in confined cell migration [28, 29]. Nevertheless, recent studies employing flat silicon microcantilevers to confine cells have provided evidence, suggesting that, beyond undergoing passive deformation, cells can exploit their nucleus to sense confinement cues and actively modulate nuclear morphology [30, 31]. In contrast to the externally imposed confinement observed in these investigations, cells typically self-impose spatial confinement as they spontaneously migrate within and through narrow pores. In this context, the extent, to which such active nuclear mechanisms contribute to self-imposed confined migration, remains to be completely understood.

While the significance of the nucleus in confined migration has been established, there remains an ongoing debate regarding the involvement of the cytoskeleton in deforming and maneuvering the nucleus through constrictions. Numerous studies have indicated a predominant role of contractile actomyosin fibers located in front of the nucleus, generating 'pulling' forces transmitted to the nucleus through the LINC (Linker of Nucleoskeleton and Cytoskeleton) complex, which anchors actin filaments via nesprin-2 to the nuclear membrane [19, 32, 33]. Conversely, other studies have highlighted the significance of posterior cortical contractions during transmigration through narrow constrictions, proposing a mechanism based on an osmotic 'pushing' force. [26, 34, 35]. These cortical contractions are believed to be triggered by

significant nuclear deformations leading to calcium ion Ca^{2+} release, consequently enhancing myosin recruitment to the cortex [30,31]. Taken together, these investigations indicate a multifaceted interplay involving geometrical confinement, cellular migration machinery, and nuclear mechanics. However, the precise manner in which this interplay impacts migration dynamics when cells spontaneously impose physical confinement by navigating through narrow constrictions remains unclear [28,31,36].

This thesis presents the fabrication of versatile experimental platforms utilizing photolithography techniques for the investigation of confined cell migration, employing the synthetic hydrogel PEG-norbornene (PEG-NB). Initially, we employ hydrogel-hydrogel interfaces, termed 'sponge clamp', to study the invasive potential of distinct cancer cell lines. This approach is designed to elucidate variations in cell invasion dynamics contingent upon the biophysical properties of the surrounding environment. Subsequently, we establish dumbbell-shaped hydrogel cavities to explore repeated, self-imposed 3D confined cell migration. This innovative experimental approach facilitates the examination of 3D confined cell migration dynamics, with a particular emphasis on unravelling the role of the nucleus. Furthermore, we utilize these compliant hydrogel channels to investigate the mechanical properties of the nucleus during translocation. Expanding upon this, we analyze nuclear morphology across a broad range of confinement widths, aiming to deepen our understanding of cytoskeletal force generation mechanisms enabling the nucleus to navigate diverse spatial constrictions effectively.

The framework of this thesis is structured to systematically investigate cell invasion and nuclear mechanics within innovative 3D hydrogel assays, aiming to unravel the mechanisms, by which cytoskeletal forces enable cells to navigate confinement.

In **Chapter 2**, the foundation is set by examining fundamental aspects of cell migration alongside the mechanical properties of the nucleus. The chapter introduces theoretical frameworks and modeling methodologies employed in the investigation of cell migration dynamics. Moreover, it details the microfabrication techniques employed in the fabrication of biomimetic materials utilized for migration studies, along with the fundamental principles underlying the elasticity and rheology of extended bodies.

Chapter 3 presents the experimental methodologies employed in the study, starting with the utilized synthetic hydrogel PEG-NB. Furthermore, the chapter discusses the microscopy techniques utilized, alongside an introduction to the fundamental principles of atomic force microscopy.

In **Chapter 4**, the fabrication process of the hydrogel-hydrogel interfaces, referred to as 'sponge clamps', is detailed. Characterization of swelling properties and stiffness is conducted, contingent upon the composition of the utilized hydrogel. Additionally, the chapter provides insights into cell invasion dynamics through narrow constrictions for two distinct cancer cell lines, MDA-MB-231 and HT-1080.

Chapter 5 introduces dumbbell-shaped cavities within a PEG-NB hydrogel layer to study cell mechanics. The chapter begins by elucidating the microfabrication process, emphasizing the creation of a well-defined and adaptable experimental platform. Specifically, this chapter examines the influence of physical confinement on the

migration dynamics of MDA-MB-231 cells. Furthermore, it includes the inference of a stochastic dynamical top-down model for the confined migration process, enabling the separation of deterministic and stochastic components of the dynamics.

In **Chapter 6**, the investigation delves into the nucleus's role as a rate-limiting factor by examining its mechanical characteristics within the dumbbell-shaped cavities. This includes an exploration of the viscoelastic properties of the nucleus and a quantitative assessment of its volume during confinement translocation. Moreover, the chapter entails the determination of contact forces exerted by the nucleus as it traverses through compliant hydrogel channels, achieved through the utilization of tracer beads embedded within the hydrogel.

In **Chapter 7**, an analysis is presented regarding the morphological changes of the nucleus across a wide spectrum of confinement widths. The chapter investigates how force-generation mechanisms adapt in response to varying degrees of confinement. These findings are further challenged by experimentally perturbing the pulling force mechanisms and analyzing cytosolic calcium levels relative to the level of confinement.

Chapter 8 provides an outlook and comprehensive discussion of the topics discovered in this thesis. Additional experimental methodologies are detailed in **Appendix A**, while a detailed description of the data analysis techniques is provided in **Appendix B**.

2. Fundamental Concepts

2.1 Cell Migration

Cell migration plays a key role in physiological processes such as wound healing and immune response [37–40]. However, the migratory behavior of cells can also pose significant risks to organisms, particularly when cancer cells undergo transitions towards a migratory phenotype [3]. This transition frequently leads to the formation of cancer metastasis, which account for the majority of cancer-associated fatalities [4]. Consequently, understanding and predicting cellular migration behavior could emerge as pivotal facets in the development of more effective therapeutic strategies.

After decades of research on cell migration, much is known about the key players involved in the cell migration machinery. At the molecular level, cell migration is a highly complex process that involves the coordination of hundreds of different proteins. Subsequently, the main components implicated in the process of cell migration and the cell environment are presented, followed by a closer look at different modes of cell migration as well as guidance mechanisms and cellular force generation.

2.1.1 Role of the Cytoskeleton and Cellular Adhesion Machinery

The cellular cytoskeleton constitutes a highly dynamic network consisting of various polymers and fibers, present in all cell types. The cytoskeleton fulfills three primary functions: spatial organization of cellular contents, establishment of physical and biochemical connections between the cell and its external environment, and generation of coordinated forces essential for cellular motility and morphogenesis [41]. Achieving these functions necessitates the activity of various cytoplasmic proteins and organelles.

Contrary to its static implications, the cytoskeleton is a dynamic and adaptable framework characterized by continuous flux in its component polymers and regulatory proteins. It consists of three distinct types of cytoskeletal filaments: actin filaments, intermediate filaments and microtubules (see Figure 2.1) [42]. All three cytoskeletal polymers function as mechanical components, distinguished by their stiffness, the dynamics of their assembly, their polarity, and the type of molecular motors with which they interact. [41].

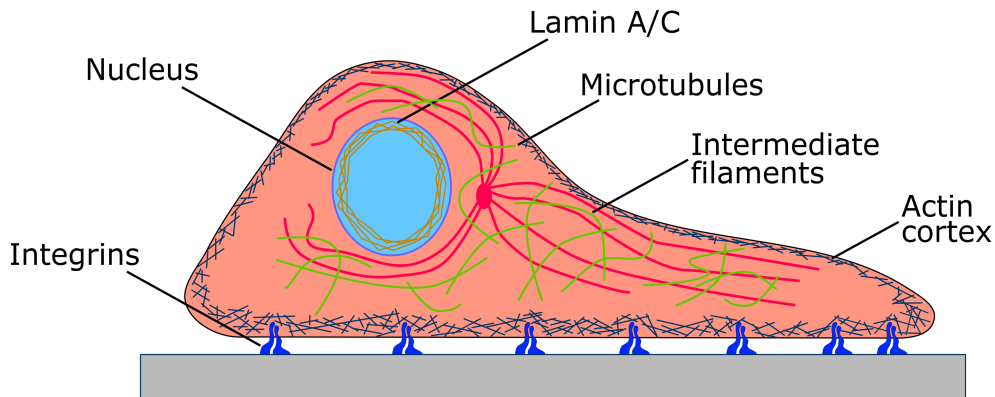


Figure 2.1: **Illustration of the pivotal cytoskeletal components.** The cytoskeleton is mainly composed of microtubules (green), intermediate filaments (red), and actin (purple fibers). The cytoskeleton is linked to the substrate through adhesions mediated by e.g. integrins (blue).

Microtubules are the stiffest and largest component of the three polymers. They form elongated and rigid constructs that extend from the centrosome towards the cell periphery, contributing to an extensive network within the cell. They have the most complex assembly and disassembly dynamics, notably contributing to cell division by forming the mitotic spindle and in cell migration, helping to maintain the cell polarization and actin assembly.

Actin filaments are much less rigid than microtubules but the presence of high concentrations of crosslinkers that bind to actin filaments promotes the assembly of highly organized, stiff structures, including bundled and branched networks. Bundles of aligned filaments support filopodial protrusions, which are involved in chemotaxis and cell-cell communication. In contrast, networks of highly branched filaments support the leading edge of most motile cells and generate the forces involved crucial for alterations in cellular morphology. Furthermore, the actin cytoskeleton is continually assembled and disassembled in response to the local activity of signalling systems, such as the local triggering of contractile actin-filament bundles known as stress fibers when cells interact with their environment via integrins [43, 44].

Both actin filaments and microtubules possess a polarized structure, characterized by two distinct ends where a dynamic polymerization and depolymerization of the structures take place. As a result, both act as tracks for molecular motors such as dynein, kinesin and myosin proteins [45, 46]. These motors have essential roles in organizing the microtubule and actin cytoskeleton, such as the interaction of myosin motors with bundles of aligned actin filaments. This interaction enables cells to contract and sense their environment [47, 48].

In contrast, intermediate filaments, the third cytoskeletal filament, are not polarized and cannot support movement of molecular motors. These filaments are the least stiff of the three and can be crosslinked to each other, as well as to actin filaments and microtubules. Intermediate filaments offer mechanical support for the internal cytoplasmic environment and cell surface, while also participating in cellular shap-

ing and regulating signal transduction pathways [49–51], including keratins and vimentins. Nuclear lamins also constitute intermediate filaments and play a pivotal role in maintaining the structural integrity and stiffness of the nucleus [29, 52].

Moreover, for effective interaction with the cell environment, the cytoskeleton must be coupled to the ECM via an adhesion machinery [53]. Central to this process are integrins, a pivotal group of molecules that bridge the gap between the cell environment and the cytoskeleton [54]. Integrins, transmembrane proteins composed of α and β subunits, facilitate binding to ECM proteins and facilitate cell-cell interactions. Notably, integrins can bind various ECM proteins, including fibronectin, collagen, and laminin. Upon stable binding of multiple integrins to the ECM, focal adhesions, larger adhesion clusters, are formed, establishing stable connections between the cellular environment and the cytoskeleton. This not only enables cell adhesion but also provides a platform for signaling events. Integrins are recognized as key players in mechanotransduction, the process by which mechanical cues from the cellular environment are translated into intracellular signals. Alongside other signaling receptors, such as those detecting soluble growth factor gradients, integrins play a critical role in directed cell migration.

2.1.2 Cellular Migration Modes

Cells exhibit diverse modes of migration depending on their phenotype and functional role as well as the surrounding ECM and their biophysical properties. For instance, leukocytes predominantly migrate individually throughout various tissues in the body during their lifespan, while numerous other cell types undergo migration collectively, participating in tissue organization, shaping, or repair processes. This phenomenon is called collective migration, characterized by the coordinated movement of cell clusters, which is observed among many cell populations, either as loosely or tightly associated groups [55].

The fundamental process of cell migration starts with the establishment of cellular polarity, with a leading edge and a trailing end. Subsequent to this, actomyosin-mediated protrusions form at the leading edge, which subsequently attach to the substrate through integrin-based focal adhesions. Contraction of the actomyosin complex induces tension along the cellular longitudinal axis, thereby facilitating forward translocation of the cell body and retraction of the trailing end [43, 56]. This basic migratory mechanism is conserved across a spectrum of cell types and modes of migration. Nevertheless, each migration mode harbors distinct variants, which depend on the cellular environment [57, 58]. Consequently, differences occur in cellular morphology, migration velocity and cell-cell interactions. Generally, cell migration can be divided into single-cell and collective cell migration. Each mode of migration is further subdivided into various types. The following paragraph focuses on migration modes of single cells and its subcategories.

Single-cell migration can be categorized into amoeboid and mesenchymal migration (see Figure 2.2). Amoeboid migration comprises two distinct forms: blebby amoeboid migration, characterized by rounded or ellipsoid cells lacking mature focal adhesions and filopodia, relying instead on propulsive blebs for movement; and

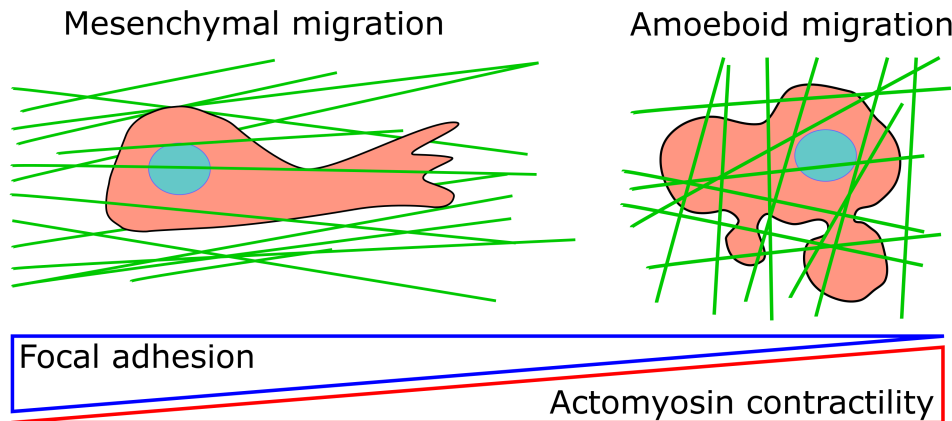


Figure 2.2: **Single cell migration modes.** Exemplary cells demonstrate either the mesenchymal migration mode along ECM fibres, featuring elongated, spindle-shaped cells with pronounced focal adhesions, or the blebby amoeboid migration mode, characterized by rounded morphology pushing against ECM fibres, lacking of focal adhesions and filopodia.

pseudopodal amoeboid migration, characterized by elongated cells with weak cell-substrate interactions and actin-rich filopodia at their leading edge [59, 60]. Examples of cells employing these mechanisms include leukocytes, neutrophils, and dendritic cells.

Conversely, mesenchymal migration involves elongated, spindle-like cells with robust focal adhesions and increased cytoskeletal contractility. This mode of migration closely resembles the general migratory process and is observed in cells such as fibroblasts and sarcoma cells [61, 62]. However, cells exhibit migratory behavior not only within an organism but also in their ECM. The terminologies migration and invasion are commonly employed interchangeably in biological discourse. While the underlying mechanisms are closely related, cell migration is defined as the directed translocation of cells across a 2D surface or through a 3D matrix. Conversely, cell invasion occurs when a cell is embedded within a dense 3D network, such as certain ECMs. Therefore, additional processes are required to facilitate cellular locomotion. Principally, cells can remodel the surrounding ECM in instances where the pores of the ECM are too constricted for cellular traversal. This remodeling entails the enzymatic degradation of the ECM by matrix metalloproteinases (MMPs) or other proteases, thereby generating migration conduits through the cleavage of structural fiber proteins such as collagen or fibronectin within the ECM [63].

2.1.3 Impact of 3D Confinement on Cell Migration

Cell migration is influenced by both intrinsic characteristics of the migrating cells and external environmental factors. The environmental conditions, including properties such as stiffness, size, and density, along with the spatial arrangement of adhesion sites, can be well controlled in the context of migration on two-dimensional, continuous substrates [64, 65]. However, the regulatory factors become notably more

complex within 3D networks. A pivotal component of the 3D *in vivo* extracellular environment is the ECM. The ECM represents a dynamic composition primarily comprising two major classes of macromolecules: proteoglycans and fibrous proteins [10, 66, 67].

Cells synthesize ECM components internally, subsequently releasing them through

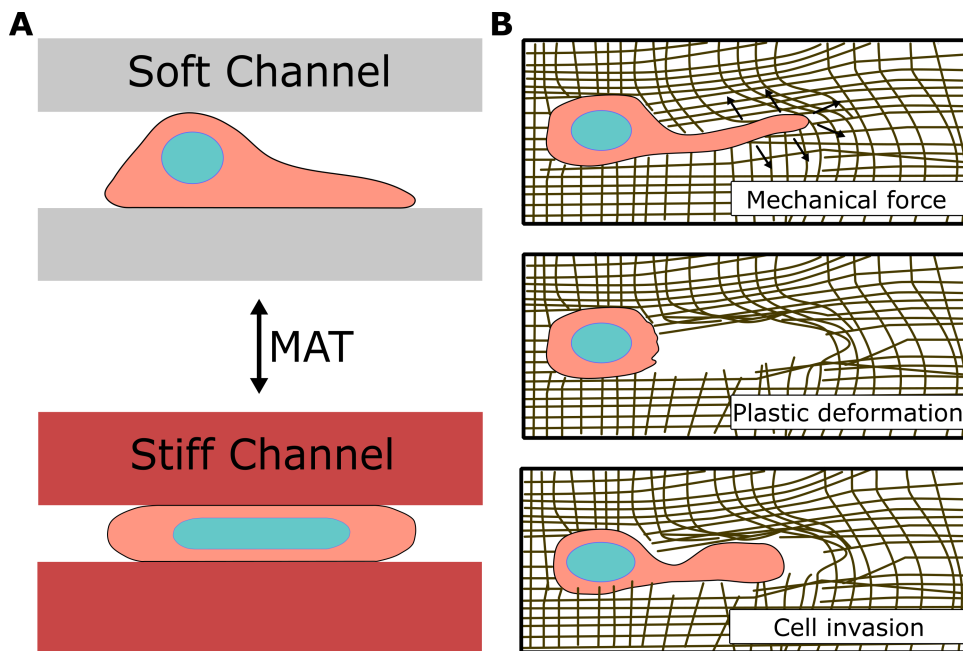


Figure 2.3: **Illustration of the ECM impact on cell migration behavior.** (A) Change of cellular phenotype induced by the environmental properties such as confinement height and matrix stiffness. (B) Schematic sequence of plasticity-mediated cell migration, where cell-generated forces plastically deform the matrix to open paths and facilitate cell invasion.

exocytosis into the extracellular milieu, where they undergo remodeling, modification, or degradation by other cells. This continual process results in the dynamic alteration of the ECM's composition and organization by cells themselves. Despite the ECM's fundamental components being largely consistent across diverse organs and tissues, its composition and, consequently, its properties exhibit considerable divergence, ranging from the rigidity of bone tissue to soft brain matter [68].

The ECM goes beyond a structural scaffold for cellular housing, as it is a multifaceted assembly of macromolecules, growth factors and higher-order structures that interplay and change over time. Consequently, interplay between ECM and cells significantly modulates cellular function and behavior. In addition to its role in biochemical signaling, the ECM provides three-dimensional mechanical and structural cues, both of which have emerged as significant determinants influencing three-dimensional (3D) cell migration, as evidenced by computational and experimental studies [69, 70]. Key environmental parameters influencing 3D migration include confinement, adhesions sites, and the viscoelastic properties of the surrounding matrix [71–73]. Notably, significant confinement below a certain threshold can impede

migration by impeding nuclear movement. The impact of adhesion sites varies with cell phenotype, with certain migration types relying on force transmission through focal adhesions, while others remain adhesion-independent. Moreover, cells possess the ability to switch migratory phenotypes in response to environmental cues, in addition to biochemical stimuli. For instance, the stiffness of the surrounding matrix has been implicated in driving tumor metastasis through the induction of epithelial-mesenchymal transition (EMT) [74].

Additionally, physical confinement has been observed to potentially enhance cell migration velocity and induce mesenchymal-amoeboid transition (MAT), thereby increasing invasive capability significantly (see Figure 2.3A). This phenotype strongly influences migratory characteristics, including speed and persistence [22]. Geiger et al. conducted experimental investigations demonstrating that reduced fiber stiffness not only hinders cellular motility but also prevents the mesenchymal-amoeboid transition, suggesting that high matrix stiffness is crucial for initiating MAT [72]. Furthermore, recent research has uncovered that tumor tissues exhibit not only increased stiffness compared to normal tissue but also heightened viscosity [75, 76]. This elevated mechanical plasticity enables cell-generated forces to induce microstructural alterations in the surrounding environment. This mode of migration, termed plasticity-mediated migration, operates independently of protease activity, as it does not involve degradation of the surrounding ECM. Consequently, the physically expanded pores facilitates cancer cell invasion and metastasis (see Figure 2.3B) [71].

2.1.4 Guidance Mechanisms of Cell Migration

The characteristics of the ECM play a significant role not only in determining the mode of cell migration but also in directing migration along specific trajectories. This phenomenon is observed in various physiological processes such as embryogenesis and cancer metastasis, particularly in cancer cell migration towards vascular structures, where distinct guidance cues are distributed asymmetrically within the cellular environment [77, 78].

One mechanism of guidance involves contact guidance along geometric features such as collagen fibers, nerve bundles, or engineered surfaces. Consequently, *in vivo* studies often incorporate structures such as pillars and cavities [79–81]. In the context of cancer metastasis, cells frequently exploit existing anatomical features to facilitate their escape from primary sites. However, this guidance is not solely dependent on physical contact, as ECM density along these structures is often reduced or absent, thereby promoting 3D cell migration. *in vitro* experiments have demonstrated that perpendicular grooves enhance wound closure independent of cell adhesion to the substrate, while tilted pillars effectively polarize and guide the movement of normal human dermal fibroblasts [82, 83].

Furthermore, the mechanical properties of the ECM can also serve as guidance cues for cell migration, a phenomenon known as durotaxis. This process entails individual cells adhering to and migrating along a substrate with heterogeneous stiffness distributions (see Figure 2.4). Under such conditions, cells tend to

migrate from regions of lower stiffness toward those of higher stiffness, regardless of their adhesive properties [84]. The effectiveness of this guidance mechanism is strongly influenced by both the gradient of stiffness and the absolute stiffness of the substrate [85, 86]. It is hypothesized that cells exert traction forces on their surroundings and thereby determine the substrate rigidity. Subsequently, this mechanical information may be transduced into chemical signals within the cell, orchestrating the process of cell migration. A recent study, has revealed that durotactic behavior can emerge within cell collectives [87]. In this work, the response of isolated human mammary epithelial cells (MCF-10A) was compared to that of cell clusters plated on substrates featuring stiffness gradients. Notably, the researchers observed durotaxis in the clustered cells while the isolated cells did not exhibit such behavior, implying long-range force transmission across the cluster via cadherin-based contacts [87].

In addition to its involvement in physiological processes, evidence from *in vitro*

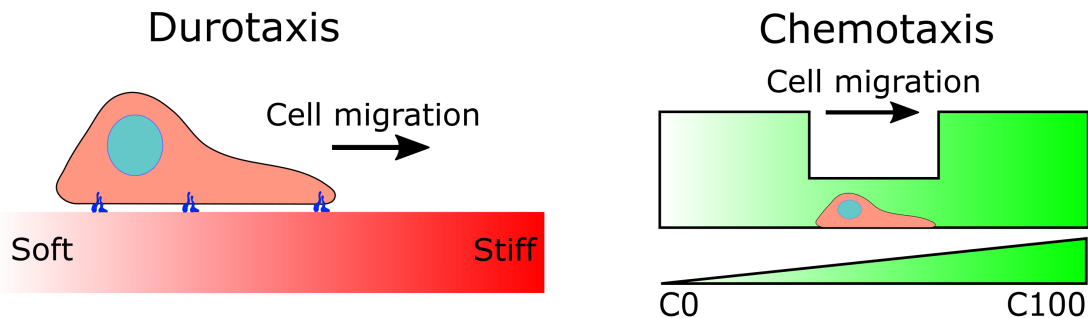


Figure 2.4: **Depiction of guidance cues.** Durotaxis is elucidated as the mechanism of guidance, wherein cells tend to migrate in accordance with stiffness gradients. In contrast, chemotaxis is contingent upon the spatial distribution of signaling molecules.

studies indicates that durotaxis plays a role in fibrosis and cancer progression [88]. It is well documented that cancer cells cultured on stiff substrates exhibit more aggressive phenotypes compared to those on softer substrates [89, 90].

Another mechanism of guidance relies on the spatial distribution of signaling molecules, which can be either matrix-bound, termed haptotaxis, or soluble, termed chemotaxis (see Figure 2.4). These guidance mechanisms not only involve growth factors or signaling molecules but also consider the concentration of adhesion linkers such as collagen, fibronectin, or receptors presented by adjacent cells [91–93]. Various fundamental processes in organisms, including embryogenesis, immune response, and cancer metastasis, have been extensively studied regarding the role of chemotactic guidance. For instance, dysregulated chemotaxis of leukocytes and lymphocytes contributes to inflammatory diseases such as asthma and arthritis [94, 95].

Numerous signaling pathways have been identified that translate gradients in the concentration of signaling molecules, initially perceived by cell-surface receptors, into cellular polarization towards regions of higher chemoattractant concentration [96–98]. Moreover, it is unlikely that cell migration is solely governed by a

single mechanism; rather, various guidance cues collectively influence cell behavior. In the context of cancer metastasis, soluble chemotactic gradients likely direct migration, while preexisting structures such as nerve bundles or fibers contribute to contact guidance [99,100].

2.2 Theoretical Description of Cell Migration

In recent decades, extensive investigations into the dynamics of cellular motility and migration have revealed the complex intracellular signaling networks regulating the movement of eukaryotic cells. The mechanisms underlying cell motility involve a broad variety of physical phenomena, including the polymer physics governing cytoskeletal dynamics [101,102], the dynamics of signaling molecules through reaction-diffusion processes [103], and the active mechanical forces generated by acto-myosin contraction [104,105]. These physical processes collectively contribute to the propulsion of the cell membrane, resulting in overall cellular motion. Much of this motility machinery is evolutionary conserved across various organisms and tissues, suggesting the potential for a universal understanding of cell motility through the elucidation of its underlying physics [44]. However, while significant progress has been made in elucidating the biophysical aspects of cell motility, the integration of these processes to generate collective cellular behaviors remains a current focus of research [105].

A promising perspective lies in exploring whether principles from physics can exceed the elucidation of individual physical components of cellular systems and offer conceptual and predictive frameworks for understanding emergent cellular behaviors. To address this challenge, there has been growing integration of mathematical and computational modeling with experimental research. These modeling approaches serve as tools for achieving a quantitative system-level comprehension of migratory behaviors. Consequently, two primary modeling approaches have been extensively developed. Firstly, bottom-up models start with postulated rules describing various cellular components and aim to predict emergent behaviors. These models are typically compared to experimental data by fitting model parameters to match predicted and experimentally observed statistics. Examples include cellular Potts models [7,106] and models coupling actin flow, polarity cues, and focal adhesion dynamics [107]. However, a drawback of these bottom-up approaches is their difficulty in directly applying to experimental observations due to the large number of parameters that may be challenging to constrain based on experimental data [105]. As a result, models are frequently tailored to capture specific aspects of data but may encounter challenges in depicting the complete temporal dynamics exhibited by cells or their responses to external stimuli.

Secondly, an alternative approach to mechanistic modeling is presented through data-driven top-down models, which systematically constrain model selections by utilizing experimental data. These approaches commonly yield a more phenomenological representation of the system, drawing upon experimental data at the cellular or tissue level rather than the molecular scale.

2.2.1 Persistent Random Walk

The first systematic analysis into the motion of small organisms were conducted in the 1920s, during which Fürth observed that the movement exhibits not purely stochastic behavior but instead demonstrates a degree of persistence [108]. This phenomenon can be mathematically described through the Ornstein-Uhlenbeck process:

$$P \frac{\delta \vec{v}}{\delta t} = -\vec{v} + \sqrt{2D} \vec{\eta}. \quad (2.1)$$

Given the velocity vector \vec{v} and the diffusion coefficient D that typifies Brownian motion, P denotes the persistence time, denoting the timescale at which the stochastic self-propulsion velocity randomize, while $\vec{\eta}$ represents a normalized Gaussian white noise. The mean square displacement (MSD), often referred to as Fürth's formula, can be delineated as follows:

$$MSD(t) = \langle |x(t) - x_0|^2 \rangle = 2nD(t - P(1 - e^{-\frac{t}{P}})), \quad (2.2)$$

where n is the number of dimensions. Also, it was observed that the behavior of cells crawling on a two-dimensional surface matched the Ornstein-Uhlenbeck process, leading to the establishment of Fürth's Formula as the standard formalism for analyzing cell migration [109, 110]. Furthermore, one investigation focused on the motion of mouse fibroblasts in tissue culture [111]. The results revealed that the direction of motion for intervals of 5 hours, appeared stochastic. Both, the theoretical analysis and experimental validation demonstrated that the motility of persisting cells could be characterized by an augmented diffusion constant D^* .

2.2.2 Data-Driven Top-Down Approaches

Adopting a reductionist approach, cell migration has been extensively investigated on precisely defined structures, yielding insights into key aspects of the migratory behavior of cells. These observations have been formalized into simple, top-down models, which need to be constrained by experimental data to provide a phenomenological depiction of cellular systems without reference to specific molecular processes [105]. Top-down models utilizing the full spectrum of spatial and temporal information that characterizes a process will be superior compared to techniques reliant on processed statistics derived from data. Another central idea in top-down approaches is that they prioritize agnosticism towards the underlying molecular or mechanistic determinants of behavior. Consequently, inference approaches within this framework start with a sufficiently broad class of diverse models, with inference procedures selecting the most appropriate model based on available data. Moreover, a successfully constrained model, despite being based on experimental data, should possess the capability to predict novel observations beyond the data used to constrain.

One example of such top-down modeling is presented by Brückner et al. [23], who introduced a theoretical framework describing the stochastic migration of cells on

two-state micropatterns. In this case, cell persistence depends upon the local geometries of the pattern, which can be captured through a generalization of the underdamped Langevin equation:

$$\dot{v}(x, v) = F(x, v) + \sigma(x, v)\xi(t). \quad (2.3)$$

Here $F(x, v)$ represents the deterministic component of nuclear dynamics dependent on position and velocity, while σ and ξ denote the amplitude of noise and Gaussian white noise, respectively. In the case of cell migration on patterns comprising two square-shaped islands connected by a narrow bridge, Brückner et al. successfully inferred the values of $F(x, v)$ and $\sigma(x, v)$ from experimental data. Their analysis demonstrated that Eq. 2.4 effectively characterizes the observed migration dynamics. Particularly, the inferred values of $F(x, v)$ on such two-state patterns revealed an interesting acceleration behavior of cells upon entering the channel, resulting in deterministic cycling between the islands.

2.2.3 Bottom-Up Mechanistic Cell Migration Models

In addition to the benefits of such data-driven models, it is important to acknowledge their shortcomings. These models typically lack generalization and often fail to provide mechanistic insights into the underlying processes governing cell migration. To address this challenge, simplified physical models are frequently employed, aiming to elucidate the fundamental mechanisms driving cell motility and incorporate them into quantitative, predictive frameworks [105]. Consequently, simplified bottom-up models, often characterized by 1D descriptions of cell polarity and migration dynamics based on physical principles, have been developed. Among others, Sens proposed a bottom-up model focusing on the pivotal role of underlying mechanics in organizing cell motility, such as the active mechanics of the cytoskeleton, cell membrane tension, and substrate stiffness [112]. This model describes cell spreading and crawling through the interplay between actin polymerization and cell-substrate adhesion mediated by mechanosensitive stochastic linker. Despite its simplicity, this model predicts several well-known cellular behaviors documented in the literature, including the stick-slip behavior of the cell front and phenomena like spontaneous symmetry breaking or bistability observed in cells and cell fragments [113–115]. Overall, these 1D bottom-up migration models have provided valuable insights into key cellular behaviors observed experimentally [105]. However, challenges remain in precisely predicting the stochastic dynamics of cells, particularly in structured environments.

To address this limitation, intermediate models that bridge the gap between inferred descriptions from top-down approaches and mechanistic bottom-up migration models are essential [105]. Following this approach, Brückner et al. extended their investigations to acquire more mechanistic insights through data-driven models [116]. Consequently, they progressed beyond describing the cell solely in terms of its overall position to develop a more detailed model incorporating the nuclear position x_n , the position of an experimentally derived protrusion coordinate x_p , and the cell polarity P . This way of describing the cell enabled them to systematically constrain on the

structure of such a mechanistic model using experimental data. The velocities of the nucleus are then described as follows:

$$\zeta_n \gamma(x_n) \dot{x}_n = k(x_p - x_n), \quad (2.4)$$

where ξ_n represents the friction coefficient of the nucleus, k characterizes the linear elastic coupling between nucleus and protrusion and $\gamma(x_n)$ ensures reduced friction within the constriction. Furthermore, the variations in the protrusion velocities \dot{x}_p are significantly larger and are described as follows:

$$\zeta_p \dot{x}_p = -k(x_p - x_n) - \delta_{x_p} V(x_p) + P(t). \quad (2.5)$$

Here, ζ_p denotes the friction coefficient of the protrusion, while the confining potential $V(x_p)$ accounts for the boundaries of the pattern. The dynamics of polarity, exhibiting time-correlated behavior, are expressed within the geometry adaptation (GA) model. Within this model, the magnitude and direction of polarity feedback depend on the specific local geometry of the confinement, as expressed in the following equation:

$$\dot{P}_{GA} = \alpha(x_p) P_{GA} - \beta P_{GA}^3 + \sigma \xi(t). \quad (2.6)$$

The parameters α and β determine the stochastic dynamics of the protrusion. Overall, this model describes the confinement-induced acceleration observed in [23] through the interplay between cellular confinement and polarization. More recently, Flommersfeld et al. have build up to this intermediate model by introducing a generalized model of confined cell migration, revealing how membrane tension, actin alignment, and polarity cue diffusion interplay to generate the geometry adaptation effect [117].

2.3 Mechanics of the Cell Nucleus

In recent years, there has been increasing consideration of the cell nucleus regarding its role in cell invasion and cancer metastasis. On the one hand, the cytoplasm is very flexible and can undergo large deformations as well as actively remodel to occupy the available space, allowing it to penetrate openings as small as 1 μm [118, 119]. The nucleus, on the other hand, is the largest cellular organelle and approximately 5-10 times stiffer than the surrounding cytoskeleton as it is mechanically stabilized by a constitutive network of structural proteins; therefore it commonly resists large changes in shape. Additionally, the nucleus occupies a large fraction of the cellular volume [120]; with a typical diameter of 5-10 μm , the nucleus is larger than many of the pores encountered in the ECM.

As previously discussed, cells navigate through their surrounding ECM by traversing tight meshwork structures, forming constrictions ranging from less than 1 μm to several tens of microns. When encountering constrictions smaller than the diameter of the nucleus, the nucleus must undergo deformation to the size of the constriction [27, 28, 121]. Consequently, for migration through small pores or 3D scaffolds,

the nucleus can become the rate-limiting organelle. For instance, Wolf et al. showed that nuclear deformability constitutes a rate-limiting factor during non-proteolytic migration of cells through 3D collagen matrices [118]. The need for physical deformation emphasizes the significance of nuclear flexibility in facilitating cellular invasion through the ECM network. Additionally, migration within confining environments raises the general question, whether and how cells can regulate their nuclear characteristics and force generation mechanisms to overcome such spatial constrictions.

2.3.1 Physical and Biological Properties

The positioning and movement of the nucleus relies on coordinated interactions among various cellular components. These include the extensions of the leading edge, attachment of integrins to the extracellular matrix, the contractility of actin cytoskeleton fibers, the organization of microtubules, and the linker of cytoskeleton and nucleuskeleton (LINC) complex, which physically connects chromatin to the cytoskeleton. The interplay of these cellular components can be perturbed by external forces. These disturbances may lead to structural alterations within the nucleus facilitated by the cytoskeletal framework. This framework acts as a conduit for the transmission of mechanical forces from the cellular membrane to the nuclear envelope. Consequently, this can lead to unregulated exchange of materials between the nucleus and cytoplasm, DNA damage, and cell death. [122]. Consequently, preserving the nucleus's ability to resist extreme deformation and strain energy release is crucial for maintaining its mechanical stability [28, 36]. For that reason, significant attention is directed towards understanding the viscoelastic properties of the nucleus.

The overall stiffness, or elasticity, of the nucleus within a cell depends on various structural factors, including the presence of A-type lamins within the nuclear lamin network that supports the double nuclear membranes, as well as the chromatin organization. Deficiency in lamin A/C leads to notable displacement of the microtubule organizing center from the nuclear envelope and has profound effects on the mechanical characteristics of the nucleus, as demonstrated by investigations utilizing intracellular nanorheology. Both the elasticity and viscosity of the nucleus are impacted by lamin A/C deficiency [29, 52].

Furthermore, the chromatin also contributes to the viscoelastic properties of the nucleus. The chromatin's packing state exhibits variability and adjusts in response to various cellular changes such as transcriptional requirements, DNA repair activities, and the phase of the cell cycle. Throughout the cell cycle, there are transient and reversible alterations in DNA organization, characterized by the conversion of dense heterochromatin to more open euchromatin via histone acetylation or demethylation processes [123, 124]. These modifications induce chromatin decondensation, resulting in nuclear softening and size increase [125, 126]. Conversely, chromatin condensation enhances nuclear compaction and stiffness while reducing nuclear size, facilitating cellular migration in processes like wound healing and cancer metastasis [127]. These dynamic changes highlight the complex relationship between chromatin structure

and cellular functionality.

Previous investigations into cell nuclear mechanics did not separate the individual roles of chromatin and lamins in the overall nuclear response to physiological strains and strain rates. However, Stephens et al. achieved this distinction by successfully characterizing the viscoelastic properties of the nucleus, specifically elucidating the contributions of lamin A/C and chromatin [128]. They employed an innovative micromanipulation technique to isolate and gradually stretch individual cell nuclei at physiological speeds and strains, ensuring reproducible nuclear force-extension measurements. This methodology revealed that chromatin compaction primarily governs the short-extension force response during small deformations, while depletion of lamin A/C insignificantly influences this regime. Conversely, lamin A/C levels dictate the nuclear capability for strain stiffening under extensive deformations. These intricate physical modifications within the nuclear interior significantly impact cellular morphology and migration in 3D confined environments. Notably, low lamin A levels have been associated with colon cancer recurrence [129] and malignant carcinomas [130], highlighting the crucial *in vivo* role of lamin A in cellular survival and behavior.

2.3.2 Mechanisms of Cellular Force Generation

Due to the considerable size and stiffness of the nucleus, cells are required to exert significant intracellular forces in order to induce deformation of the nucleus as it traverses constrictions. This process of nuclear deformation and locomotion through narrow spaces imposes constraints on the migratory capacity of cells within confined 3D environments [20, 26, 29, 131]. However, the precise mechanism by which cells mobilize the nucleus through confined spaces, including whether cells predominantly exert pulling or pushing forces on the nucleus, remains incompletely understood. It is probable that cells employ a variable combination of both mechanisms, depending upon specific environmental conditions.

In the majority of migrating cells, the nucleus assumes a posterior position, located in the rear of the cell [132]. Recent investigations suggest that actomyosin contractility, potentially in conjunction with intermediate filaments, physically pull the nucleus forward during both 2D and 3D migration (see Figure 2.5) [19, 32, 33]. Therefore, recent studies have elucidated the molecular components responsible for physically linking the nucleus to the cytoskeleton, with the LINC complex identified as the pivotal structure facilitating the transmission of mechanical forces across the nuclear envelope [133]. In the context of 3D lamellipodial-based migration, the coordinated action of actomyosin contractility and integrin-mediated traction at the leading edge is required for the translocation of the nucleus through narrow constrictions. Specifically, myosin IIA-containing actomyosin bundles collaborate with vimentin filaments to pull the nucleus by engaging with nesprin-3 α of the LINC complex via plectin [134].

Conversely, other work highlighted the significance of rear cortical contractions during transmigration through narrow constrictions, presenting a mechanism based on an osmotic "pushing" force [26, 34, 35]. This mechanism entails the accumula-

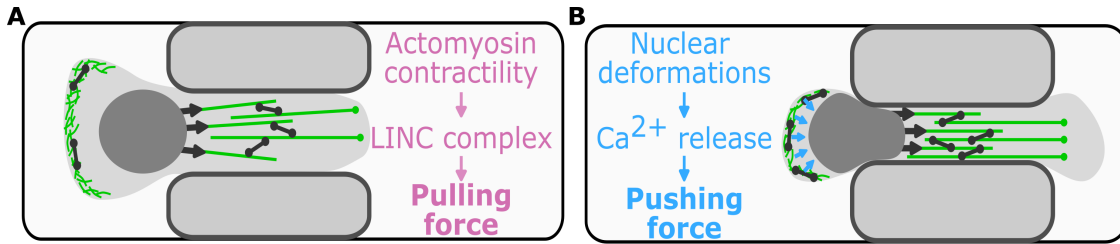


Figure 2.5: **Sketch of the cellular force generation mechanisms.** (A) During 3D migration, actomyosin contractility pulls the nucleus forward. Confinement of the protrusion induces growth, thereby enhancing the pulling force. (B) Strong deformations of the nucleus trigger the release of Ca^{2+} , resulting in increased cortical contractility. As a consequence, pressure in the rear of the cell increases, leading to an enhanced pushing force exerted upon the nucleus. Figure adapted from [135].

tion of actin and active myosin in the rear cell cortex, based on increased RhoA-ROCK signaling induced by substantial nuclear deformations triggering Ca^{2+} release [30,31,135]. RhoA-ROCK-mediated contraction of the rear results in enhanced intracellular pressure in the posterior cell compartment, exerting a propulsive force on the nucleus to facilitate migration through confined spaces [34]. Although the cytosolic back pressure requires locally concentrated actomyosin contractility, the precise regulatory mechanisms governing this force-generating mechanism within intricate geometries remain unclear.

Recent findings by Ju et al. propose that the localized reinforcement of microtubules by cytoplasmic linker-associated proteins (CLASP) serves as a mechanostat enabling cells to appropriately position the nucleus and temporally coordinate actomyosin contractility, thereby generating the cytosolic hydrostatic pressure requisite for overcoming nuclear barrier [35]. Upon achieving a threshold cytosolic hydrostatic pressure in the rear cellular compartment, the microtubules undergo disassembly, releasing GEF-H1, which organizes localized coordination of microtubule and actin dynamics. This activates a final burst of RhoA-mediated contractility at the rear membrane, consequently enhancing nuclear velocity and facilitating transmigration through the constriction. In a broader context, recent work suggests that certain cell lines possess the capability to employ both mechanisms for nuclear transit, contingent upon environmental conditions, albeit with potential variations in preference among individual cell lines [34]. The degree of independent or synergistic mechanisms of these pushing and pulling forces in facilitating nuclear transit requires further investigations.

2.3.3 Nucleus as an Internal Ruler

Similar to modern engineered devices, cells within the human body possess the capability to measure their surroundings. Despite the growing recognition of the significance of boundary conditions (BCs) in cellular physiology, only a limited number of mechanisms through which cells can distinguish specific BCs have been precisely elucidated. Notably, factors such as substrate stiffness or adhesive envi-

ronment geometry are among the identified mechanisms, predominantly associated with strain or stress, collectively termed mechanotransduction pathways [136–138]. Recent studies have demonstrated that mechanical cell deformation and cellular packing density within populated tissue regions exert influence over major morphodynamic processes, including cortical actomyosin contractility, cell division, and cell extrusion and invasion.

For instance, epithelial cells in the intestine monitor local cell densities and exit the

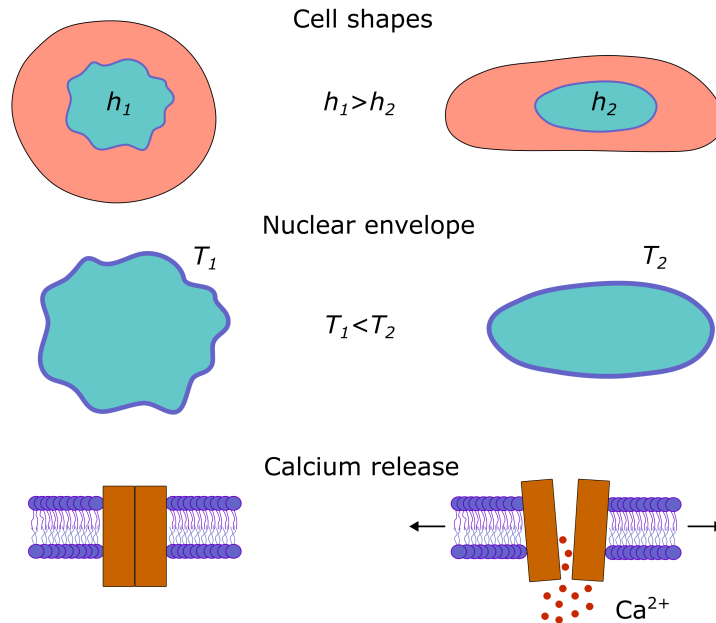


Figure 2.6: **Sketch of the nuclear ruler model.** Cells utilize the nucleus as an intrinsic ruler of cellular height regulation. Upon deformation of the cell below its resting nuclear height (h_1), there is an increase in nuclear surface area. Upon reaching a critical height (h_2), the NE undergoes full expansion and elongation, thereby increasing its tensile strength (T). This heightened tension within the NE subsequently triggers the activation of stretch-sensitive proteins, modulating and promoting cortical actomyosin contractility.

tissue once a threshold density is surpassed, thereby preventing hyperplasia [139]. Immune cells possess the ability to assess the pore size of neighboring tissues, facilitating migration towards regions of minimal mechanical resistance [140]. Epidermal stem cells utilize the availability of ECM for cell attachment and spreading as a guiding cue in their determination of cell fate [141]. Cumulatively, these findings suggest the existence of a conserved, albeit unidentified, mechanosensitive cellular signaling module governing myosin II-based cortical contractility and the transformation of motile cells, contingent upon cellular shape deformations within constrained tissue microenvironments [60, 142, 143]. Among others, mechanosensitive molecules localized both around and within the nucleus have been recognized as pivotal players. Their physical connections to cytoskeletal components transmit external forces via membrane receptors [144]. Therefore, the nucleus has gathered increased attention to possibly act as an internal ruler within the cell.

Recent research has identified the nucleus as a pivotal component for quantifying cellular shape deformation through two primary physical parameters: nuclear shape deformation resulting in inner nuclear membrane (INM) unfolding and the intracellular spatial arrangement of the nucleus [30, 31]. Each individual cell in its non-stressed state possesses a specific nuclear volume and an excess of nuclear envelope (NE) surface area contained within NE folds. When the dimension of the cell is reduced below the resting nuclear diameter, the nucleus undergoes deformation, leading to unfolding of its envelope. Upon complete unfolding of the NE, it undergoes stretching, prompting the release of calcium (see Figure 2.6). Calcium ions, classical messenger molecules, exert a well-known stimulatory effect on actomyosin contractility, thereby mechanistically linking cell height to cell contractility [145]. The parameter space defined by these two variables (INM unfolding and calcium levels) serves as a dual-input identifier for cells to decode distinct shape deformation, as demonstrated in instances such as anisotropic cell deformation in confinement versus isotropic hypotonic cell stretching. This enables cells to adopt specific adaptive responses contingent upon the type of physical shape deformation encountered.

These findings highlight the notion that nucleus deformation and its intracellular positioning establish a cellular sensing mechanism enabling cells to promptly and reversibly adjust their dynamic response to fluctuations in shape. In the context of cell migration, such tailored cellular behaviors may help cells in avoiding environmental entrapment, a phenomenon which is relevant in processes such as cancer cell invasion [26, 122, 146].

2.4 Microfabrication of Biomimetic Materials

Cell cultures are widely utilized in biological and medical research as simplified model systems to investigate complex aspects of human biology. The primary objective of employing these *in vitro* models is to enhance the time efficiency of research and make them more economically viable, thereby facilitating early-stage screening assays. Nevertheless, a notable limitation arises from the gradual loss of cellular phenotype attributed to the simplified composition of prevailing culture platforms utilized for model establishment. Unlike in *in vivo* conditions, where cell function is influenced by biochemical and biophysical cues from the microenvironment, conventional culture systems lack such complexity [96, 98, 147]. To address this issue, biomaterials, particularly hydrogels, have gained widespread acceptance as substitutes for the *in vivo* ECM in numerous *in vitro* models [148]. Hydrogels have emerged as optimal substrates for *in vitro* cell cultures, exhibiting favorable characteristics as both 2D and 3D scaffolds due to their high porosity, facilitating nutrient and gas transport, and their adjustable chemical and mechanical properties [149, 150].

2.4.1 2D and 3D Experimental Platforms

To enable the study of mammalian cells, it is imperative to culture them in an environment that closely mimics the *in vivo* conditions of the body. Traditionally, this involves culturing cells on a flat substrate, thereby restricting them to two dimensions. Typically, substrates composed of glass or plastic are coated with ECM proteins to facilitate cell adhesion, onto which cells are seeded (see Figure 2.7). Moreover, the surface coating can be engineered with microstructures to facilitate migration analysis, or alternatively applied onto a thin layer of hydrogel, often comprised of cross-linked polyacrylamide (PA), for investigations on softer substrates [5,7,89,90]. 2D experimental assays offer several advantages, including rapid cell proliferation, simple and straightforward procedures and low reagent costs. Furthermore, these experimental setups are suitable to high-throughput analysis while maintaining robust reproducibility. However, 2D cell culture entails inherent limitations. Cells are constrained to planar configurations, failing to mimic the native structures. Moreover, the absence of a three-dimensional cellular microenvironment prevent the establishment of complex cell-cell and cell-environment interactions. Consequently, these factors may induce variances in cellular morphology and molecular pathways compared to *in vivo* situations. Hence, differences have been observed between experiments conducted in 2D versus those conducted in 3D, as well as *in vivo* experiments [11,151].

For that reason, 3D cell culture has attracted increased attention to address these

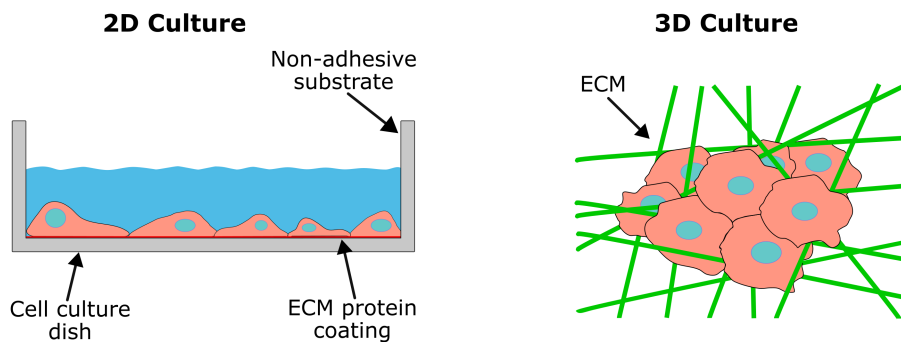


Figure 2.7: **Illustration of 2D and 3D cell culture.** In 2D cell cultures, cells adhere to and migrate along a planar substrate. In 3D cell cultures, cells proliferate within a 3D environment, typically embedded within a gel-like matrix or grown on a solid scaffold.

limitations. Particularly when the aim is to accurately model physiological phenomena in *in vitro*, 3D assays are often considered superior to their 2D counterparts. The principal advantages of 3D cell culture include enhanced *in vivo*-like cell-cell interactions, proliferation dynamics, and morphological features, attributable to the more accurate representation of the natural environment of cells. Furthermore, 3D culture systems afford cells variable access to nutrients, metabolites, and signaling molecules, which allows cells the creation of distinct environmental niches and microenvironments, in contrast to the homogeneity of 2D culture environments [152].

Additionally, 3D experimental platforms offer biochemical and biophysical cues, such as concentration gradients and tissue stiffness, as well as potential heterogeneities in mechanical properties [91]. Despite the increased complexity of 3D assays, robust reproducibility can still be achieved. However, these approaches are not without drawbacks, including prolonged culture formation times due to matrix physical constraints and increased reagent costs. Moreover, the multifaceted influence of cues provided by the 3D environment on cellular behavior often complicates result interpretation and the disentanglement of concurrent cellular influences. In summary, it is crucial to clarify the experimental objectives beforehand and subsequently select the most appropriate assay format suited to target the underlying scientific question.

2.4.2 Synthetic and Naturally Derived Hydrogels

The term hydrogel describes 3D network structures derived from a variety of synthetic and/or natural polymers capable of absorbing and retaining significant amounts of water. Hydrogels manifest as swollen 3D viscoelastic polymeric networks possessing physical properties replicating the cellular microenvironment. Hydrogels utilized for replicating cellular microenvironments must adhere to various biological and physical design criteria dictated by specific applications. For instance, hydrogels intended for 3D cell culture necessitate crosslinking in the presence of cells to ensure cell viability [153]. Moreover, these hydrogels must mimic essential elements of the natural ECM, such as providing mechanical support and undergoing controlled degradation. This imitation is crucial for facilitating appropriate and desired cellular functions, including proliferation and protein secretion [154, 155]. These 3D environments can be derived from either natural or synthetic hydrogels, each approach having its own advantages and drawbacks, which will be explored within this section.

Natural polymers are derived from organic materials and can be constructed from

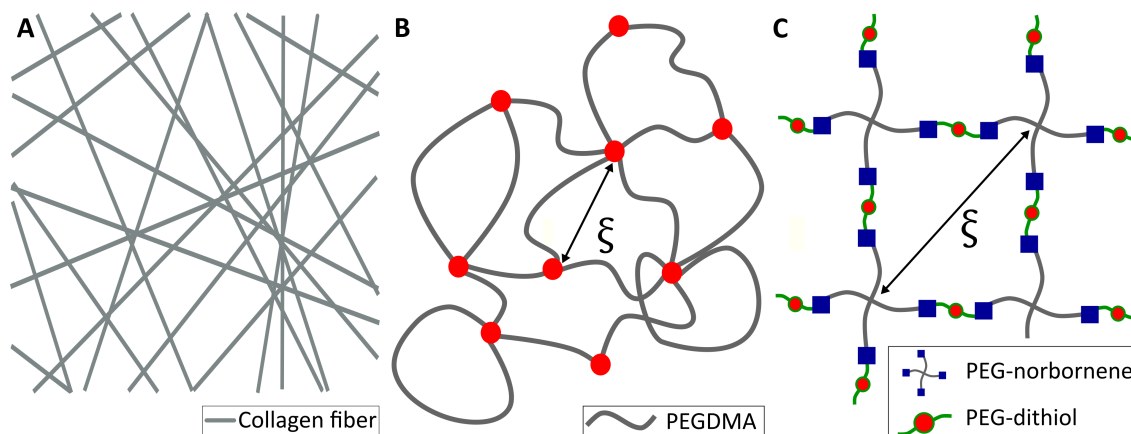


Figure 2.8: **Hydrogel classes.** (A) Naturally derived hydrogels, here collagen as an example. (B) (C) Reaction mechanism comparison of synthetic hydrogels: PEG-diacrylate formed via a chain-growth mechanism (B) and PEG-norbornene formed via a step-growth mechanism (C).

individual protein constituents, such as collagen, gelatin, elastin, and fibrin, or from protein blends like cell-derived Matrigel (see Figure 2.8). These polymers serve as extensively utilized biomimetic substrates in 3D cell culture and microenvironment engineering, owing to their inherent beneficial attributes, which include biocompatibility, facilitation of cell adhesion, and responsiveness to enzymatic activity and restructuring mediated by cells [13,14,155–159]. Collagen, an important constituent of the ECM, is a naturally occurring biological material prevalent in skin, bone, and blood vessels [14,160,161]. Gelatin, derived from animal collagen through thermal denaturation, shares similar characteristics. Due to their biodegradability and the production of non-toxic degradation byproducts, collagen and gelating hydrogels are beneficial for cellular embedding within their stable fibrillar network. The structural attributes, stiffness, and pore sizes of collagen gels exhibit considerable variability depending on the collagen extraction method and gelation conditions employed. These gels can be supplemented with other ECM components, such as fibronectin, to more closely mimic the natural ECM. However, the resultant matrix, characterized by fiber formation, displays high heterogeneity, resembling *in vivo* conditions and replicating ECM complexity. This heterogeneity, while beneficial for mimicking natural conditions, poses challenges in discerning fundamental guidance mechanisms due to the simultaneous presentation of multiple cues. Additionally, the density of adhesion and cell signaling sites in collagen depends on protein concentration, which concurrently influences gel stiffness [162]. Thus, altering the concentration of adhesion sites unavoidably modifies the substrate stiffness.

Matrigel, another widely employed natural hydrogel for 3D cell culture, is a commercially available, thermo-responsive ECM-based substrate. Derived from Engelbreth-Holm-Swarm (EHS) mouse sarcoma cells, Matrigel has been extensively utilized for over three decades across a broad spectrum of applications, including transmigration assays, cancer spheroid culture, and stem cell culture [15,163,164]. Below 10°C, Matrigel exhibits liquid-like properties and can be manipulated using conventional liquid-handling instruments. However, above 10°C, it undergoes self-assembly, forming an optically transparent hydrogel capable of supporting cell proliferation and viability. Nevertheless, attempts to generate thin-layer 3D cell cultures suitable for imaging and other analytical techniques using low volumes of Matrigel may yield inconsistent results due to air-liquid interfacial tension and evaporation. While larger volumes can reduce these issues by producing thicker hydrogels, challenges such as extensive diffusion distances, increased costs, and incompatibility with standard imaging tools constrain their utility. A notable limitation of Matrigel stems from its complex and incompletely characterized composition, comprising numerous growth factors, signaling molecules, and matrix proteins with batch-to-batch variability [16]. This variability impedes the widespread adoption of Matrigel across various applications due to concerns regarding reproducibility.

Synthetic hydrogels are produced using methodologies within synthetic chemistry, often involving the cross-linking of bioinert chemical monomers. While synthetic hydrogels may be considered less biomimetic compared to their naturally derived

counterpart, they offer distinct advantages. Notably, the chemistry and composition of synthetic hydrogels can be tailored and precisely controlled, enhancing their reproducibility and allowing for precise adjustment of their biophysical properties. Commonly employed synthetic hydrogels include poly(acrylamide) (PA), poly(ethylene glycol) (PEG) and poly(vinyl alcohol) (PVA) [165–169]. For instance, PVA, a longstanding polymer hydrogel material, has experienced renewed interest in recent years. Numerous studies have highlighted its potential for further investigation. PVA is a water-soluble, long-chain polymer that mimics the fiber structure of the ECM, with mesh sizes ranging from a few nm to several μm , depending on the PVA and intended application. These hydrogels have gathered significant attention due to their low toxicity, high water absorption capacity, favorable mechanical properties, and excellent biocompatibility [170, 171]. Moreover, they are widely recognized for their diverse application in bio-medicine, including tissue engineering scaffolds, wound dressings, and soft robotics [172].

Another commonly utilized synthetic hydrogel is PA due to its advantageous physical and chemical characteristics, which encompass chemical inertness, high porosity and permeability, optical transparency, and adjustable elasticity [173]. Consequently, PA hydrogel substrates coated with ECM proteins find widespread application in 2D cell microenvironments, notably in 2D traction force microscopy [174–177]. Recent advancements have extended the versatility of PA hydrogels through approaches involving 3D printing, enabling the creation of complex structures with resolutions of 100–150 μm [178].

PEG-based hydrogels stand out as perhaps the most prevalent synthetic hydrogel, owing to the non-toxic nature of their precursor even before polymerization, which facilitates cell encapsulation within 3D environments [153, 179, 180]. Linear and multi-arm PEG monomers undergo cross-linking via various reaction methods, yielding a relatively uniform mesh. Gelation of PEG hydrogels can occur spontaneously, triggered by temperature changes, or induced by illumination through radical polymerization methods, including chain growth-polymerization and step-growth polymerization [181, 182]. Although PEG alone lacks the ability to support cellular activity, copolymers of PEG incorporating biologically active moieties, such as peptides, have been successfully employed in diverse *in vivo* and *in vitro* studies. For instance, fibronectin-derived RGD peptide sequences are frequently utilized as ligands, enabling cell adhesion and migration [153, 183]. Furthermore, manipulation of the mechanical properties of PEG-based hydrogels can be achieved by adjusting monomer concentration or cross-linker quantity independently of ligand concentration. However, a limitation of PEG-based hydrogels is the relatively small mesh size, typically a few tens of nm, considerably smaller than pores found in the natural ECM [184, 185].

2.4.3 Different Microfabrication Techniques

Synthetic hydrogels can be manufactured and polymerized using various microfabrication techniques, each with distinct advantages and drawbacks. These

methodologies encompass micromolding and UV lithography, which can be further classified into photomask-based photolithography and maskless photolithography. Numerous micromolding strategies have been documented for constructing 3D tissue constructs [21, 179, 186, 187]. Micromolding is a versatile technique applicable across a wide range of hydrogels. Initially, a silicon wafer is coated with photoresist, undergoes soft-baking, and is then exposed to laser direct imaging to define specific structures. Elastomers like polydimethylsiloxane (PDMS) and poly(methylmethacrylate)(PMMA) have been utilized as templates for tissue construct fabrication (see Figure 2.9A). Recently, Afthinos et al. demonstrated the utility of micromolding in casting an experimental assay for 3D traction force measurements within compliant microchannels [21]. Microchannels were fabricated on a silicon wafer serving as a mold for polymerization of PA. Briefly, the microchannel design was imprinted on the lower surface of the gel, which was then combined with a flat PA gel to achieve 3D confinement (see Figure 2.9A). Furthermore, the entire device underwent coating with ECM proteins via chemical activation of the hydrogel followed by ECM addition and overnight incubation. Generally, micromolding offers advantages such as rapid processing and user-friendly procedures, yet it is associated with prolonged waiting times for testing new designs due to the necessity of fabricating silicon wafers.

Conventional photolithography methods utilized in tissue engineering primarily

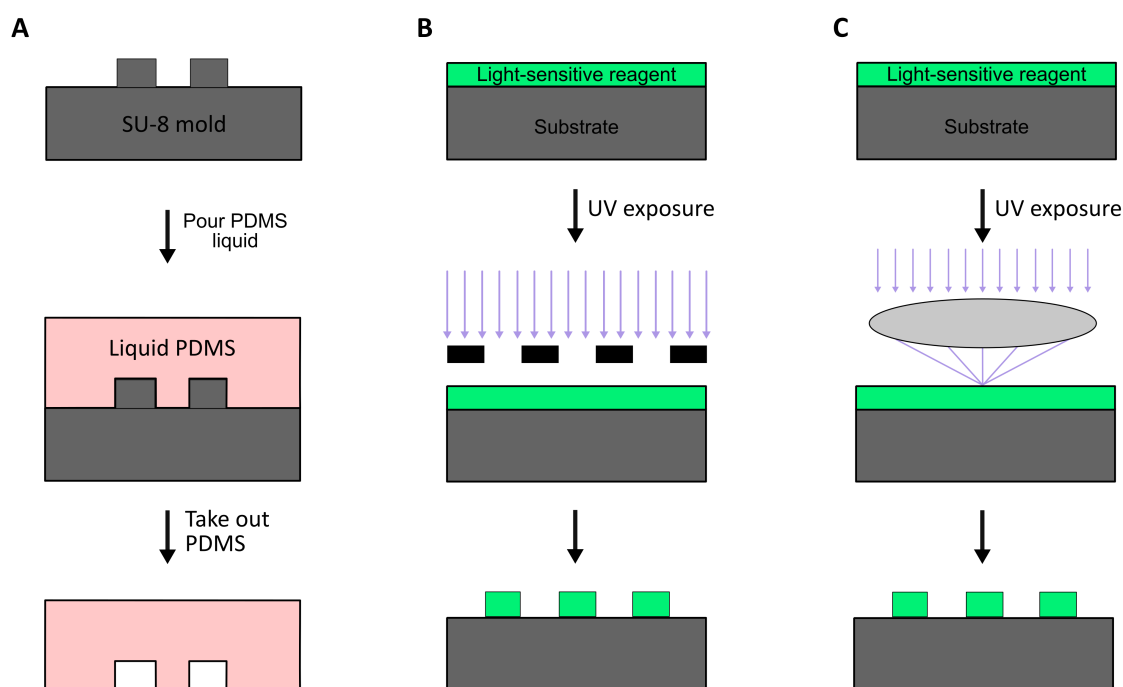


Figure 2.9: **Microfabrication processes.** (A) Micromolding commonly employs SU-8 photoresist molds, from which PDMS is subsequently replicated. (B) The photosensitive reagent is exposed to UV light through a chromium-mask containing the desired structures. (C) Mask-free technique involves direct laser writing, where features are directly inscribed in the photosensitive reagent.

include mask-based photolithography and stereolithography, each possessing distinct attributes such as cost considerations, levels of cell damage, resolution, and fabrication speed.

Photomask-based lithography relies on a UV light source that selectively polymerizes photosensitive hydrogel precursors based on the design of the employed photomask (see Figure 2.9B) and finds application across various experimental platforms [153, 165, 183, 188]. Subsequent to exposure, the remaining hydrogel precursors can be washed away, leaving behind the polymerized hydrogel as depicted in Figure 2.9B. For instance, Dietrich et al. introduced a novel technique to induce uniaxial strain in matrices by microstructuring photo-polymerizable PEG-norbornene (PEG-NB) hydrogel strips with embedded cells in a channel slide to investigate the effects of macroscopic deformation on single cell migration [153]. In brief, fibrosarcoma cells are encapsulated in thick slabs of PEG-NB hydrogel, which are polymerized through the addition of a radical photo-initiator and selective UV illumination via specific photomasks. This microfabrication technique presents the benefits of a simple setup, facilitating the generation of numerous replicas of the experimental assay in a high-throughput fashion. Nevertheless, the rapid prototyping process is hindered by the necessity of creating new photomasks for each novel design, and the attainable resolution is constrained by diffraction limitations.

Maskless photolithography has been used for the production of many well-defined experimental platforms [189–191]. This method employs a UV laser for the selective polymerization of hydrogels, without the need for a photomask (see Figure 2.9 C). Among others, Zorlutuna et al. produced multifunctional polymer hydrogels that recapitulate cell-cell interactions between skeletal muscle myoblast cells and primary hippocampus neuron cells [189]. The ability of perfusable structure in these hydrogels is required for long-term culturing of 3D structured tissue. In short, alginate hydrogel was polymerized via the usage of a radical photo-initiator, a UV laser (325nm) and a computer controlled elevator that allows automated fabrication of complex 3D shapes in a layer-by-layer fashion. An alternative laser-based stereolithography uses two-photon laser systems, in order to fabricate 3D hydrogels using photosensitive materials [192, 193]. The advantage of these approaches is that they are able to produce 3D tissue constructs with micro- or nanometer-scale precisions. However, drawbacks of this approach are possible toxicity of the photo-initiator and the fabrication speed especially for large tissue constructs.

2.5 Elasticity and Rheology of Extended Bodies

In physics and materials science, elasticity theory plays a pivotal role in the domain of mechanics, providing deep insights into the fundamental responses of materials to external forces. Robert Hooke's proposed work in 1678 established a fundamental relationship between the force applied to a spring and its resulting deformation, encapsulated in his proposition that the extension of a spring is directly proportional to the force exerted upon it [194]. This foundational principle is the basis of classical

(infinitesimal-strain) elasticity theory. In general, elasticity denotes the ability of a body to resist a deformation and return to its original configuration upon removal of the applied force. Through systematic analysis, elasticity theory reveals parameters such as the Young's modulus, shear modulus, and Poisson's ratio, which characterize a material's resistance to tensile forces, shear stress, and volumetric changes, respectively. These parameters serve as fundamental elements for comprehending the mechanical properties of materials and predicting their responses under diverse loading conditions. Particularly, in bio-mechanics, elasticity theory plays a crucial role in elucidating the mechanical properties of biological tissues.

At the opposite end of the materials spectrum, Isaac Newton directed his focus toward liquids, as evidenced in his work 'Principia' published in 1687, wherein he introduced a hypothesis pertaining to steady shearing flow [195]. This hypothesis posits that the resistance arising from the lack of slipperiness of the parts of the liquid, assuming all other factors remain constant, is directly proportional to the velocity gradient between adjacent layers of the liquid. This phenomenon, now termed 'viscosity', denotes the intrinsic resistance of a fluid to deformation under a specified rate and quantifies the internal frictional forces acting between fluid layers in relative motion. Fluids that exhibit a constant viscosity coefficient at a given temperature, irrespective of the applied strain rate, are classified as 'Newtonian fluids'. However, only a limited fraction of fluids demonstrate such constant viscosity behavior. Conversely, a large fraction of fluids exhibits viscosity changes with strain rate, which are classified as 'non-Newtonian fluids'.

To characterize the flow behavior of materials that exhibit a combination of elastic and viscous properties, rheology emerged by integrating principles from both elasticity and (Newtonian) fluid mechanics. This interdisciplinary approach addresses materials situated between the classical extremes of pure elasticity and fluid behavior. Notably, the foundational laws formulated by Hooke and Newton are linear in nature, presuming a direct proportionality between stress and strain. Consequently, the viscoelastic behavior discussed thus far operates within a linear framework, capable of accommodating a broad spectrum of rheological phenomena. However, it is essential to acknowledge that the linear regime is inherently constrained, with materials exhibiting linear behavior only within a finite range of stress. This range may be relatively modest, indicating that material properties such as rigidity and viscosity can undergo alterations in response to applied stress. Such alterations may manifest either instantaneously or over a long period of time and can entail either an increase or decrease of the material parameter. For instance, the phenomenon of 'shear-thinning' arises when an applied shear rate induces molecular structural breakdown within the material, resulting in an under-proportional increase in shear stress relative to the shear rate and consequently causing a reduction in viscosity.

2.5.1 General Concepts

In the following, the foundational laws formulated by Hooke and Newton as well as rheology principals are explained.

Hooke's Law

In physics, Hooke's law is an empirical law that asserts the linear relationship between the force F required to stretch or compress a spring by a certain distance ΔL , expressed as:

$$F_s = k\Delta L, \quad (2.7)$$

here k represents a constant factor, called spring constant, denoting its stiffness. The simplest form of solid deformation occurs when a material undergoes strain along a particular axis under the influence of an applied force (see Figure 2.10). The resulting relative strain is quantified as a function of the applied force, exerted perpendicular to the material's surface areas A , and is termed as stress σ :

$$\sigma = \frac{F}{A}. \quad (2.8)$$

Robert Hooke noted the presence of a linear correlation between stress and extension

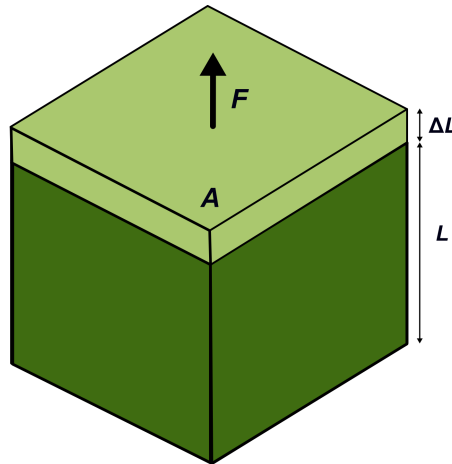


Figure 2.10: **Hookean solid.** A material is deformed along an axis by applying the force F perpendicular to the surface A . This results in the relative strain, $\epsilon = \Delta L/L$.

in many materials [194], thus:

$$\sigma = E\epsilon, \quad (2.9)$$

where E denotes the elastic modulus, also known as Young's modulus, a mechanical property characterizing the tensile or compressive stiffness of solid materials under longitudinal force application. Young's modulus quantifies the relationship between the stress σ exerted on the object and the consequent axial strain ϵ , defined as the ratio of stress to strain. Materials exhibiting a linear stress-strain correlation are termed 'Hookean' and behave like an elastic spring, as described by Eq. (2.7), where the spring constant is denoted as:

$$k = A\frac{E}{L} \quad (2.10)$$

Newtonian Fluid

Isaac Newton was the first to describe the phenomenon of resistance to motion in deforming liquids, which he termed as the lack of slipperiness among liquid particles [195]. The force F necessary to induce uniform motion between two plates separated by a distance h and in relative motion is directly proportional to the relative velocity v between the surfaces:

$$F = A\eta\frac{v}{h}, \quad (2.11)$$

where the sample beneath the surface A undergoes shear deformation as the upper plates moves parallel to the force F . This scenario establishes the dynamic viscosity η . Given that the ratio of velocity to plate spacing equals the deformation rate $\dot{\gamma} = \frac{d\gamma}{dt} = \frac{v}{h}$, the equation for viscosity is commonly known as Newton's law and given by:

$$\sigma = \eta\dot{\gamma}. \quad (2.12)$$

According to this formulation, liquids can be categorized into two groups: 'Newtonian fluids' and 'non-Newtonian fluids'. A Newtonian fluid is a liquid or gas wherein the shear stress σ during laminar flow is directly proportional to the deformation rate $\dot{\gamma}$. For isotropic, incompressible Newtonian fluids, the simple Eq. (2.12) is applicable. However, numerous materials do not conform to ideal viscous behavior and thus cannot be accurately characterized by Newton's law. This is notably observed in viscoelastic materials. Such materials are classified as non-Newtonian fluids, wherein viscosity notably varies with the shear rate and/or the duration of the applied stress.

Non-Newtonian Fluids

A non-Newtonian fluid is characterized by its ability to exhibit varying viscosity in response to applied force. Typically, this variation in viscosity is contingent upon either the shear rate or the shear rate history. While viscosity is a commonly employed concept in fluid mechanics to characterize the shear properties of fluids, it may prove insufficient in incorporating the behavior of non-Newtonian fluids. Certain non-Newtonian fluids may exhibit shear-independent viscosity, yet still display normal stress-differences or other non-Newtonian behavior.

Newtonian fluids exhibit a direct proportionality between shear rate and shear stress (see Figure 2.11A). Consequently, viscosity remains constant across a broad spectrum of shear rates. In contrast, non-Newtonian fluids can exhibit shear thinning, a phenomenon occurring from the disruption of the molecular structure of the sample due to hydrodynamic forces generated by shear. Consequently, an increase in shear rate results in a under-proportional increase in shear stress, leading to a reduction in viscosity with increasing shear rate (see Figure 2.11A). Another non-Newtonian behavior is shear thickening, characterized by an increase in the number of structural subunits under shearing. As a result, increasing shear rates induce a

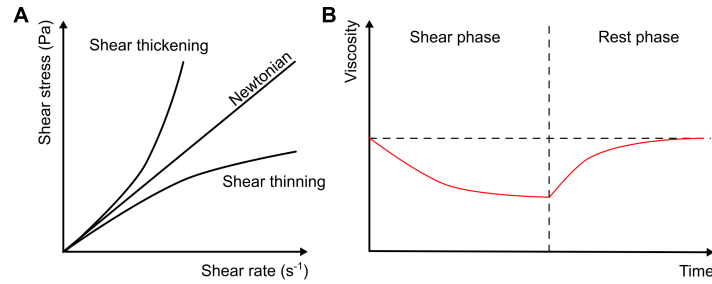


Figure 2.11: **Non-Newtonian behavior.** (A) The viscosity of non-Newtonian fluids is dependent on shear rate. (B) The fluid can exhibit time-dependent viscosity. Therefore, a constant coefficient of viscosity cannot be defined.

over-proportional increase in shear stress, yielding an increase in viscosity with increasing shear rate (see Figure 2.11A). An example of time-dependent alteration in the flow properties of non-Newtonian fluids is termed thixotropy, wherein viscosity reduces during applied shear and reverts to its initial state only after stress removal (see Figure 2.11B).

2.5.2 Poisson Ratio

Another important measure in materials science and solid mechanics is the Poisson's ratio, which serves as a quantification of the Poisson effect, a phenomenon wherein a material demonstrates a tendency to expand in directions perpendicular to the applied compression [196]. Conversely, under tensile loading, the material typically contracts in directions transverse to the applied stretching. An illustrative example of this behavior is the observable thinning of a stretched rubber band. Once again, Poisson's ratio denotes the ratio of relative contraction to relative expansion, maintaining consistent values as aforementioned. The Poisson's ratio of a stable, isotropic linear elastic material is constrained to the range of -1.0 and +0.5 due to the necessity for Young's modulus, shear modulus, and bulk modulus to maintain positive values [197]. The majority of materials exhibit Poisson ratios spanning from 0.0 to 0.5 [196]. An ideally incompressible isotropic material undergoing elastic deformation at negligible strains would possess a Poisson's ratio equal to 0.5. For many steels and rigid polymers operating within their design limits, Poisson's ratios typically exhibit values around 0.3 [198]. Rubber demonstrates a Poisson ratio approaching 0.5, while cork's Poisson ratio is around 0, indicating minimal lateral expansion during compression. In exceptional instances, certain materials exhibit transverse shrinkage under compression (or expansion under tension), resulting in a negative Poisson's ratio value [199]. These materials, such as some polymer foams, are categorized as auxetic materials [199, 200], resulting in an elongation in the perpendicular direction when stretched in one direction.

The Poisson's ratio can be described as follows under the assumption that the ma-

terial undergoes stretching or compression in a single direction (see Figure 2.12):

$$\nu = -\frac{d\epsilon_{trans}}{d\epsilon_{axial}} = -\frac{d\epsilon_y}{d\epsilon_x} = -\frac{d\epsilon_z}{d\epsilon_x} \quad (2.13)$$

where ν is the resulting Poisson's ratio, ϵ_{trans} the transverse strain and ϵ_{axial} the axial strain, respectively.

For instance, considering the elongation of a cube along the x-direction (see Figure 2.12), where there is a lengthening of ΔL in the x direction, and a shortening of $\Delta L'$ in the y and z directions, the infinitesimal diagonal strains can be expressed as:

$$d\epsilon_x = \frac{dx}{x} \quad d\epsilon_y = \frac{dy}{y} \quad d\epsilon_z = \frac{dz}{z}. \quad (2.14)$$

Assuming that the Poisson's ratio is constant through deformation, integrating these expressions and using the definition of Poisson's ratio gives

$$-\int_L^{L+\Delta L} \frac{dx}{x} = \int_L^{L+\Delta L'} \frac{dy}{y} = \int_L^{L+\Delta L'} \frac{dz}{z}. \quad (2.15)$$

Solving the relationship between ΔL and $\Delta L'$ results in:

$$\left(1 + \frac{\Delta L}{L}\right)^{-\nu} = 1 + \frac{\Delta L'}{L}. \quad (2.16)$$

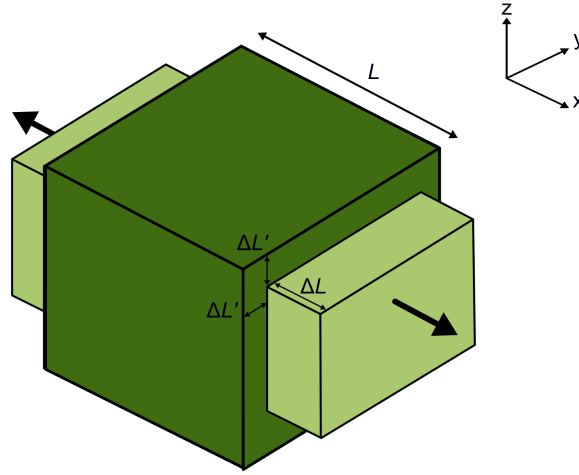


Figure 2.12: **The Poisson's ratio experiences alteration due to geometric changes.** A cubic specimen with edge dimensions of L , comprising an isotropic linearly elastic substance under uniaxial tension applied along the x -axis, featuring a Poisson's ratio of 0.5.

For very small values of ΔL and $\Delta L'$, the first-order approximation yields:

$$\nu \approx -\frac{\Delta L'}{\Delta L}. \quad (2.17)$$

Based on the length change and the following expressions

$$V = L^3 \quad (2.18)$$

and

$$V + \Delta V = (L + \Delta L)(L + \Delta L')^2 \quad (2.19)$$

the relative change of volume $\Delta V/V$ can now be calculated:

$$\frac{\Delta V}{V} = \left(1 + \frac{\Delta L}{L}\right) \left(1 + \frac{\Delta L'}{L}\right)^2 - 1. \quad (2.20)$$

Using equation 2.7 yields:

$$\frac{\Delta V}{V} = \left(1 + \frac{\Delta L}{L}\right)^{1-2\nu} - 1 \quad (2.21)$$

and for small values of ΔL and $\Delta L'$, the first-order approximation results in:

$$\frac{\Delta V}{V} \approx (1 - 2\nu) \frac{\Delta L}{L} \quad (2.22)$$

2.5.3 Contact Mechanics and Hertz Model

Contact mechanics involve the examination of the structural deformation of solids when they come into contact at one or more points [201, 202]. A pivotal aspect within contact mechanics pertains to the differentiation between stresses exerted perpendicular to the surface of the contacting bodies, termed normal stress, and those acting tangentially, termed shear stress. Normal contact mechanics, or frictionless contact mechanics, specifically delves into the analysis of normal stresses induced by externally applied normal forces and the inherent adhesion at closely interfacing surfaces. Conversely, frictional contact mechanics highlight the influence of frictional forces. Embedded within mechanical engineering, contact mechanics draws upon principles from mechanics of materials and continuum mechanics, employing physical and mathematical frameworks to address computations relevant to elastic, viscoelastic, and plastic bodies engaged in static or dynamic contact scenarios. Contact mechanics play a pivotal role in providing essential insights for the safe and energy-efficient design of technical systems, as well as facilitating investigations into contact stiffness and indentation hardness.

The foundation of contact mechanics is commonly attributed to Heinrich Hertz's publication "*On the contact of elastic solids*" (original title in German: *Über die Berührung fester elastischer Körper*). In this publication, he established the calculations concerning the contact between two non-adhesive bodies, accounting for the forces acting on both the volumes and surfaces of these bodies [203]. The theory of contact between elastic bodies serves to determine contact areas and indentation depths. For instance, to evaluate the contact between a sphere and a half-space,

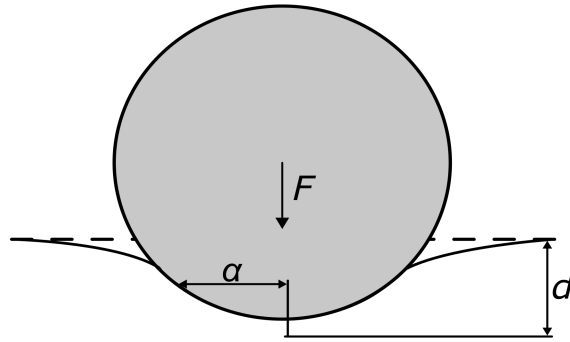


Figure 2.13: **Illustration of contact mechanics.** An elastic-half space indented by an elastic sphere.

an elastic sphere of radius R penetrates an elastic half-space, resulting in a total deformation of d and yielding a contact area of radius (see Figure 2.13):

$$\alpha = \sqrt{Rd} \quad (2.23)$$

The relationship between the applied force F and the deformation d is expressed as:

$$F = \frac{4}{3}E^*\sqrt{R}d^{3/2} \quad (2.24)$$

with

$$\frac{1}{E^*} = \frac{1 - \nu_1^2}{E_1} + \frac{1 - \nu_2^2}{E_2}. \quad (2.25)$$

E_1 , E_2 denote the elastic moduli, while ν_1 , ν_2 represent the Poisson's ratios of the elastic sphere and the indented half-space, respectively.

3. Experimental Methods

3.1 Polymerization of PEG-NB Hydrogels

In this work, the experimental assays employ synthetic PEG-NB as substrate. Previous investigations have demonstrated its suitability for studying cell migration and cellular behavior [153,180,204]. The hydrogel is synthesized by polymerizing 20 kDa polyethylene glycol (PEG) with norbornene groups at each end, with linear cross-linkers featuring thiol functionalities at both ends (see Figure 3.1). The employed cross-linker, a 1 kDa PEG-Dithiol, remains resistant to cellular degradation. Consequently, cells are unable to enzymatically degrade the surrounding ECM, which is necessary to migrate through the gels with a relative small mesh size of only a few tens of nm [184,205].

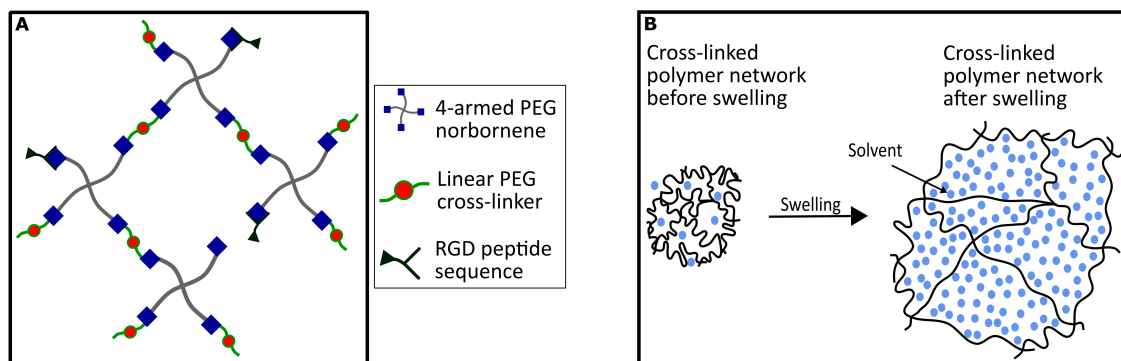


Figure 3.1: **Schematic overview of the PEG-NB hydrogel network components and characteristic swelling.** (A) PEG-NB undergoes cross-linking facilitated by a linear PEG cross-linker featuring two thiols. (B) Swelling occurs upon addition of a solvent, e.g. water. The coiled cross-linked polymer network expands, leading to elongation of the polymer chains.

In addition, a cystein-containing short Arg-Gly-Asp (RGD)-peptide sequence may be introduced to facilitate cell adhesion onto the hydrogel substrate via integrin interactions. In order to initiate radical polymerization using UV-light, the hydrogel precursor is supplemented with a photo-initiator LAP. Upon exposure to light with a wavelength of approximately 365nm, the photo-initiator absorbs the photons, leading to its dissociation in two radicals. These generated radicals are highly reactive and exhibit a tendency to abstract hydrogen atoms from nearby molecules,

particularly hydrogens from the thiol groups of the cross-linker present in the solution. This process results in the formation of thiyl groups, which subsequently engage with PEG-NB monomers to generate carbon-centered radicals. Sequential abstraction of hydrogel chains from additional thiol groups culminates in the formation of stable thioether linkages and new thiyl radicals [18, 206]. This mechanism, termed step-growth polymerization, facilitates the formation of uniform polymer networks [182, 207].

The extent of cross-linking within the hydrogel matrix plays a pivotal role and has a significant influence on its mechanical properties. Notably, the stiffness of the polymerized PEG-NB hydrogel is highly affected, spanning a range from 200 Pa to 20 kPa, thereby mimicking a wide spectrum of natural ECMs using PEG-NB hydrogels [184]. Additionally, swelling, a critical hydrogel property, is significantly influenced by the composition of the hydrogel, with water or other solvent molecules constituting up to 90% of the gel volume (see Figure 3.1 B). Factors influencing the degree of water uptake include the chemical composition and concentration of polymers within the gel, the extent of cross-linking, ionic strength, solvent pH, and temperature. The phenomenon of hydrogel swelling is theoretically well-understood, with many common approaches based on the fundamental work of Flory and Rehner [208, 209].

Hence, the amount of cross-linker utilized during hydrogel polymerization holds crucial importance, denoted as the cross-linker ratio r_c :

$$r_c = \frac{2c_{crosslinker}}{4c_{PEG-NB}} \quad (3.1)$$

The cross-linker ratio r_c in the hydrogel precursor represents the ratio of functional groups of the cross-linker (each containing two thiol groups per molecule) to the number of functional groups of the PEG-NB monomers (each containing four norbornene groups per monomer), denoted by $c_{Crosslinker}$ and c_{PEG-NB} , respectively. A cross-linker ratio of one indicates that each norbornene group present in the solution can undergo reaction with one thiol group of the cross-linker, resulting in the formation of a fully cross-linked gel.

Overall, the utilized hydrogel possesses biophysical properties closely resembling those observed in *in vivo* settings, while the photo-induced polymerization technique enables spatially and temporally controlled polymerization. Moreover, this method facilitates high-throughput fabrication with minimal batch-to-batch variability.

3.2 Light Microscopy

Light microscopy serves as a crucial tool in biological research, facilitating the observation of important biological structures at cellular and sub-cellular resolutions. By utilizing the properties of optics, light microscopy methodologies have profoundly impacted the comprehension of microscopic phenomena. Brightfield (BF) microscopy represents the most common and elementary approach within light microscopy [210]. This method incorporates a bright light source positioned beneath the sample, thereby illuminating it, while the image results through the difference

in contrast between the specimen and its surroundings. BF microscopy involves essential components, including a light source, condenser lens, objective, ocular, detector, and a sample stage for stabilization. The objective, positioned next to the sample, collects light interacting with the sample, thereby magnifying and generating an enlarged, real image. Subsequently, the ocular further magnifies this image for observation by the user. The combined magnification of the objective and ocular determines the overall magnification of the image, typically ranging from $40\times$ to $1000\times$. Nevertheless, BF microscopy encounters limitations such as low contrast in weakly absorbing samples.

Phase contrast microscopy is another technique, which functions by converting differences in the refractive indices of specimens into contrast, thereby augmenting the visibility of transparent samples. This methodology employs specialized condenser and objective lenses to induce phase shifts in light as it traverses distinct regions of the specimen [211]. Light passing through the sample remains unaltered, whereas light diffracted and phase-shifted by structures within the sample undergoes changes in phase. To increase image contrast, constructive interference is caused between the diffracted and unaltered light. This is accomplished by directing background light through a phase ring, which shifts the light by one-quarter wavelength. Upon focusing the light on the detector, the phase shift induces constructive interference between background and scattered light rays emerging from regions of the field of view containing the sample. This leads to increased brightness in these areas compared to regions devoid of the sample.

Fluorescence microscopy, another technique utilized in cellular biology, involves the use of fluorescent dyes or labeled molecules to visualize specific structures or molecules within samples [212]. This microscopy technique involves the utilization of fluorescent dyes or fluorescently labeled molecules to visualize specific structures or molecules within a sample. To this end, excitation light emitted from a white light source transmits through an excitation filter, permitting only light of a specific wavelength, capable of exciting the fluorophore, to pass through (see Figure 3.2). Upon reflection from a dichroic mirror, the excitation light is focused through the objective lens onto the sample. After excitation, the fluorescent molecules within the specimen undergo temporary excitation to a higher energetic state. Subsequently, during relaxation to the ground state a photon of a longer wavelength is emitted. A fraction of the emitted light is captured by the objective, transmitted through the dichroic mirror and the emission filter. This selectively blocks excitation light while transmitting the emitted light to the eyepiece or camera for visualization or imaging, respectively. This methodology, wherein both excitation and emitted light traverse the same objective lens, is termed epifluorescence.

The advancement of microscopy techniques has led to the establishment of confocal microscopy, which fundamentally involves an excitation source, usually a laser system, emitting coherent light. This light passes through a pinhole aperture positioned in a plane conjugate to the scanning point on the sample [213]. This leads to the emission of fluorescent light at exactly this point. A pinhole located within the optical pathway selectively blocks signals that are not in focus, thereby per-

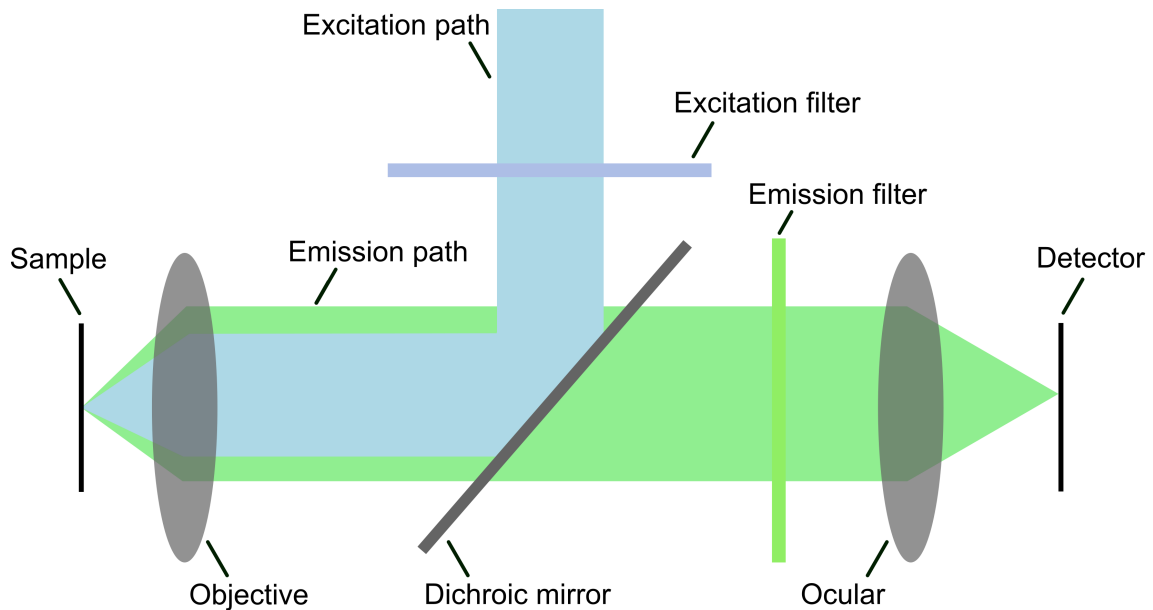


Figure 3.2: **Schematic visualization of the epifluorescence microscope technique.** Fluorescent molecules within the sample undergo transient excitation upon exposure to the excitation light. During relaxation, photons with a longer wavelength are emitted, subsequently captured by the objective lens, transmitted through the dichroic mirror and emission filter, and ultimately visualized by the detector.

mitting only the fluorescence signals originating from the illuminated spot to reach the light detector. Detectors commonly employed in this context include highly sensitive avalanche photodiodes and photomultiplier tubes, which convert light into electrical signals. Consequently, confocal microscopy offers the capability to generate sharp, detailed images of thin sections within thicker specimens, thereby finding widespread application in examining cellular structures.

3.3 Atomic Force Microscopy

Atomic force microscopy (AFM) emerged in 1986 as a scanning technique built in order to investigate phenomena at the nanoscale and has found successful application across diverse scientific and technological fields [214]. Fundamentally, AFM involves the use of a sharp tip scanning across a sample surface while registering the interactions between the tip and the sample. The tip, bound to a flexible cantilever or the sample itself, is mounted to a piezoelectric scanner capable of precise movement along three axes. Throughout the measurement process, a laser diode directs a laser beam onto the rear of the cantilever positioned above the tip. As the cantilever undergoes deflection due to forces between the sample and the tip, the angular displacement of the reflected laser beam is detected using a position-sensitive photodiode (see Figure 3.3A). Variations in beam deflection magnitude can be used to calculate the interaction force between the tip and the specimen. The AFM captures these positional alterations, enabling surface topography mapping or

real-time monitoring tip-sample interaction forces.

AFM presents several advantages over conventional microscopy techniques. While optical microscopy is a convenient tool for observing biological specimens, its resolution is constrained by the wavelength of the light source. In contrast, AFM has superior spatial resolution, reaching sub-nanometer scales, thereby facilitating the mapping of individual molecule distributions [215]. Moreover, AFM enables the investigation of both the mechanical properties of cells and their surrounding environment.

Furthermore, AFM is capable of conducting force spectroscopy, involving the di-

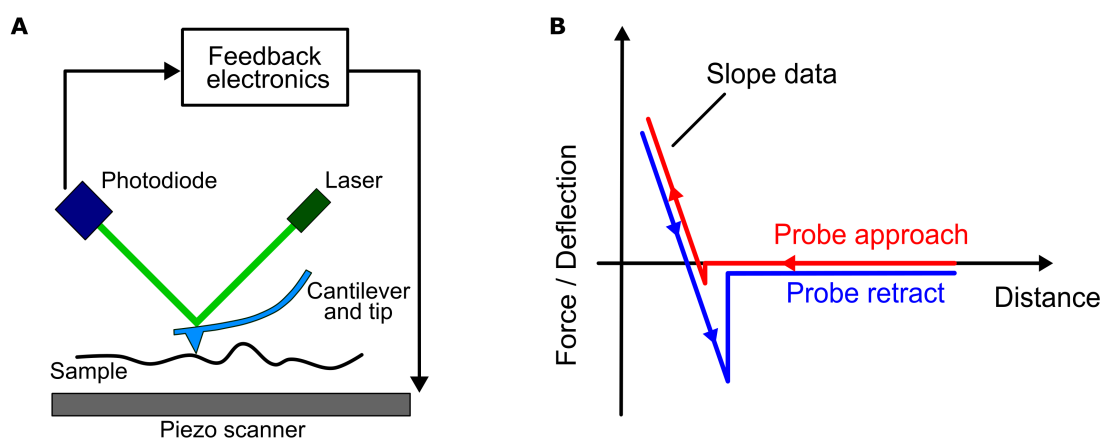


Figure 3.3: **Working principle of AFM.** (A) An AFM produces images through the scanning of a small cantilever across the surface of a sample. The sharp tip positioned at the cantilever's end makes contact with the surface, causing deflection of the cantilever and altering the amount of laser light reflected onto the photodiode. (B) Representative approach (red) and retraction curves (blue) for force-distance spectroscopy.

rect assessment of tip-sample interaction forces relative to the gap between the tip and the sample surface. In this procedure, the AFM tip is advanced towards and retracted from the surface while monitoring the cantilever's deflection in response to piezoelectric displacement. To derive the quantitative tip-sample force from the cantilever deflection, the spring constant of the cantilever must be calibrated, typically accomplished using the thermal tune method [216]. This technique treats the cantilever as a harmonic oscillator influenced by thermal noise fluctuations.

The outcome of AFM measurements are represented as a force-distance curve (see Figure 3.3 B). These force-distance curves yield a range of mechanical properties of the sample surface. For instance, the stiffness of the sample can be determined from the slope curve in the contact region. To convert stiffness into Young's modulus, the geometry of the tip-sample contact must be considered, often employing a contact mechanics model such as Hertz's model. Overall, this AFM-based force spectroscopy approach finds widespread application in biophysics for assessing the mechanical characteristics of living tissues or cells [217, 218].

4. Cell Invasion Studies in Synthetic Hydrogel Clefts

The invasion of migratory cells into surrounding tissues is a critical phenomenon central to both cancer metastasis and immune response. Cancer metastasis typically proceeds through pre-existing gaps within ECM structures or along vascular channels. Key factors such as rigidity, adhesive properties, and the width of constrictions profoundly influence the 3D migration of cells. Comprehensive migration assays are essential for probing the interplay between cellular dynamics and migration modes with respect to these parameters.

This chapter investigates the migratory velocity of cancerous cell lines traversing non-degradable synthetic hydrogel clefts. To this end, an experimental assay is developed, involving the fabrication of deformable PEG-NB hydrogels through micro-fabrication employing photolithography. The experimental setup consists of several polymerized hydrogel blocks aligned in parallel. Upon swelling, these blocks reduce the initial gap dimensions, leading to narrow interfaces between the hydrogels. These hydrogel clefts are subsequently characterized for their biophysical properties including stiffness and swelling behavior. The invasiveness of HT-1080 fibrosarcoma cells within these hydrogel configurations is then evaluated, alongside variations in experimental parameters such as initial constriction width and hydrogel composition. To promote cell invasion through these narrow clefts, a chemotactic gradient is employed. Additionally, the cellular responses of HT-1080 cells are compared with those of MDA-MB-231, a human breast adenocarcinoma cell line, to generalize the applicability of the developed experimental assay, termed 'sponge clamp'. This chapter is largely based upon the publication by Stöberl et al. [183].

4.1 Fabrication of Pressurized Migratable Hydrogel Clefts

To explore the invasive potential of human cancer cell lines, within predefined matrix gaps, we developed a novel experimental protocol termed 'sponge clamp'. This assay employs a hydrogel network comprising 4-armed PEG-NB, cross-linked by an off-stoichiometric quantity of linear PEG-dithiol, as described in section 3.1. Modulating the concentration of PEG-NB and adjusting the crosslinker amount facilitates stiffness tuning of the resulting hydrogels, yielding Young's moduli rang-

ing from 60Pa to 300Pa, effectively mimicking a spectrum of soft tissue properties. Moreover, the incorporation of the Cys-Arg-Gly-Asp-Ser (CRGDS) peptide sequence into the otherwise bio-inert and non-cleavable hydrogel matrix promotes cell adhesion via integrin interactions. Utilization of the photo-initiator LAP facilitates UV-induced polymerization. The combination of this hydrogel composition and the photolithography technique employing chromium-coated glass masks (see subsection 2.4.3 enables the fabrication of complex structured matrices with high precision in a high-throughput manner (see Figure 4.1A).

In this study, several hydrogel blocks with initial dimensions of 100 μm width and

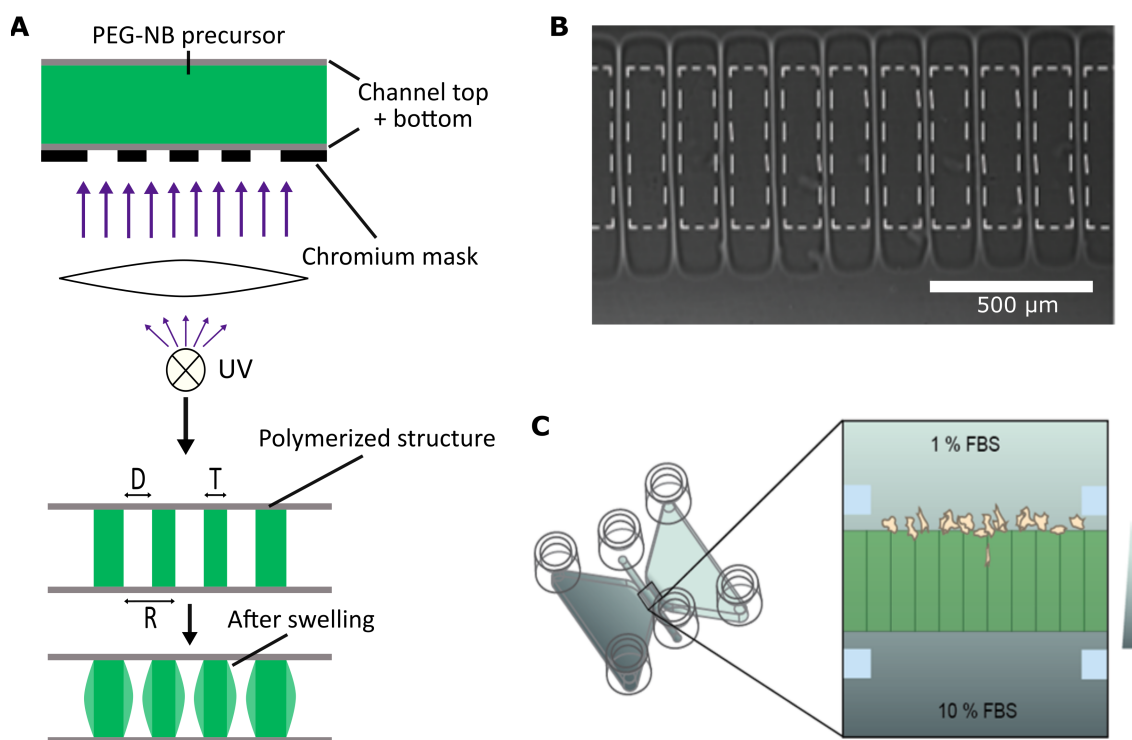


Figure 4.1: **Visualization of the fabrication process and work principle of migratable hydrogel clefts.** (A) Application of photomask-based lithography to microfabricate hydrogel blocks arranged at regular intervals within a microchannel. (B) Top-view bright field microscopy image illustrating polymerized hydrogel strips forming narrow gaps subsequent to swelling. Dashed outline corresponds to pre-swelling pattern. (C) Schematic depiction of hydrogel blocks integrated into a microfluidic chip. Reproduced from [183] with permission from the Royal Society of Chemistry.

700 μm length are casted. Through the polymerization of the hydrogel within a channel, expansion in the vertical direction is restricted, resulting in an anisotropic swelling of the polymer network, predominantly oriented transversely to the channel axis (see Figure 4.1B). The degree of expansion is dependent on the utilized precursor. As the PEG-NB hydrogel swells, the spacing between the blocks diminishes, resulting in the formation of multiple parallel hydrogel clefts (see figure 4.1B). Depending on the initial spacing of the blocks and the composition of the polymer,

swelling may extend into neighboring blocks, leading to the formation of interfaces between hydrogel blocks. To facilitate cellular invasion at these hydrogel-hydrogel interfaces, a chemotactic gradient is applied along the direction of the clefts (see Figure 4.1C). For this purpose, a commercially available channel slide featuring side reservoirs, specifically engineered for providing a stable gradient, is utilized (μ -slide chemotaxis, ibidi). The stability of the gradient has been comprehensively characterized, ensuring a well-defined and temporally stable gradient for a duration of at least 48 hours [219, 220]. Specifically, cells suspended in medium containing a low serum concentration are seeded on one side of the casted hydrogel blocks, while the adjacent chamber is filled with serum of high concentration. Overall, through the utilization of soft hydrogels with precisely defined compositions, we are able to construct highly standardized and thoroughly characterized migration pathways, enabling the study of cellular traversal through pre-existing gaps. These structures can be imaged using brightfield microscopy techniques to investigate cell invasion dynamics.

4.2 Characterization of Hydrogel Swelling and Contact Profiles

To assess the experimental observations derived from employing the 'sponge clamp', we examined the mechanical characteristics of the PEG-NB hydrogels. The shear modulus of the macroscopic bulk hydrogel was quantified utilizing a shear rheometer, serving as an estimate for the stiffness anticipated within microstructured hydrogel blocks. As illustrated in Figure 4.2A, the hydrogel compositions employed exhibit low stiffness, evidenced by storage moduli of less than 100Pa. The rigidity of the

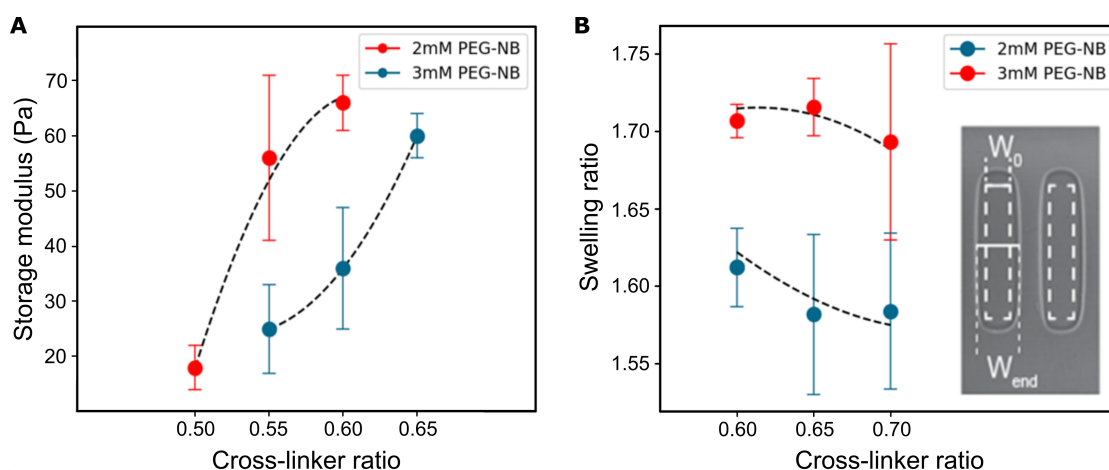


Figure 4.2: **Characterization of hydrogel properties.** Assessment of the storage modulus (A) and swelling ratio (B) of PEG-NB hydrogel across varying PEG-NB concentrations and cross-linker ratios. Presented results show the mean \pm SD derived three independent measurements. Reproduced from [183] with permission from the Royal Society of Chemistry.

gels demonstrates an increase with the cross-linker ratio across both utilized concentrations of PEG-NB. The observed storage moduli align with stiffness values previously documented for synthetic hydrogels employed in *in vitro* cell migration studies [205, 221]. Beyond rigidity, the swelling behavior is pivotal within the scope of this investigation, contingent upon the polymer and cross-linker concentrations of PEG-NB, as well as temperature variations [208, 209, 222]. Swelling ratios were determined through the expansion of free-standing hydrogel blocks, as evidenced by phase-contrast images (see Figure 4.2B inset). It was found that swelling ratios increase with increasing concentrations of PEG-NB, reaching approximately 1.72, with a lower influence observed from the cross-linker ratio.

In instances where hydrogel blocks are positioned closer than the distance given by the swelling ratio, the blocks undergo swelling and establish close proximity. Confocal microscopy utilizing fluorescently labeled dextran (MW: 10kDa), which cannot diffuse into the hydrogel due to the small mesh size, enables the visualization of closed structures. Reconstitution of the water-filled volume reveals the complete 3D contour of the clefts (see inset in Figure 4.3A). The degree of swelling in the hydrogel block near the substrate appears diminished compared to that in the channel center, likely attributed to the covalent binding of the hydrogel block to the substrate. In the channel center, the hydrogel fronts establish flat physical contact between adjacent blocks. The triangular spandrel area at the base is characterized by the gap size, denoted as G , representing the distance between hydrogel-hydrogel interfaces at the channel bottom after swelling.

To assess the extent of hydrogel swelling and consequently determine the final dis-

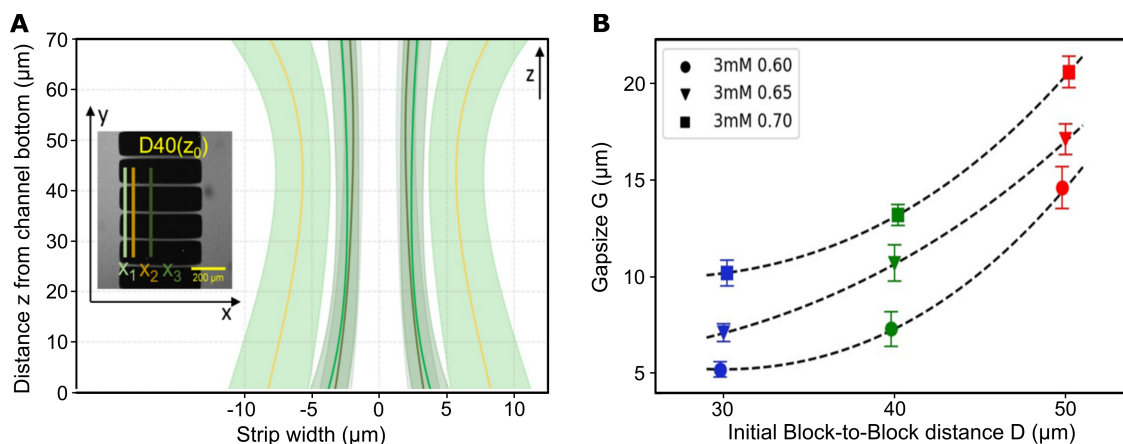


Figure 4.3: **Illustration of the final hydrogel-hydrogel interface.** (A) Hydrogel profiles as a function of distance from the substrate bottom at various x-positions, as specified in the inset. These profiles demonstrate a broader inlet compared to the constriction width within the 'sponge clamp' (presented as mean \pm SD for $n > 8$ hydrogel clefts per x-position). (B) Evaluation of the gap size, G , defined as the width of the cleft at its base, in relation to the initial distance between adjacent blocks D for different cross-linker ratios ($n > 8$ hydrogel clefts per 'sponge clamp' condition, depicted as means \pm SD). Reproduced from [183] with permission from the Royal Society of Chemistry.

tance between two hydrogel blocks, we conducted an analysis of the 3D morphology and gap size G across three initial block-to-block distance D . Notably, the hydrogel profiles consistently demonstrate the expected anisotropic swelling behavior, as indicated by an increase in swelling magnitude with greater distance from the substrate (see Figure 4.3A). Additionally, to validate the hydrogel profiles, we investigated the variation in x-position relative to the distance z from the substrate. Remarkably, the gap of the 'sponge clamp' inlet is notably broader compared to the hydrogel profiles at greater x-positions (see Figure 4.3A). Consequently, the initial block-to-block distance D delineates distinct hydrogel-cleft geometries, characterized by the gap size G at the surface of the channel bottom, through which cellular migration is facilitated (see Figure 4.3B). To evaluate the reproducibility and temporal stability

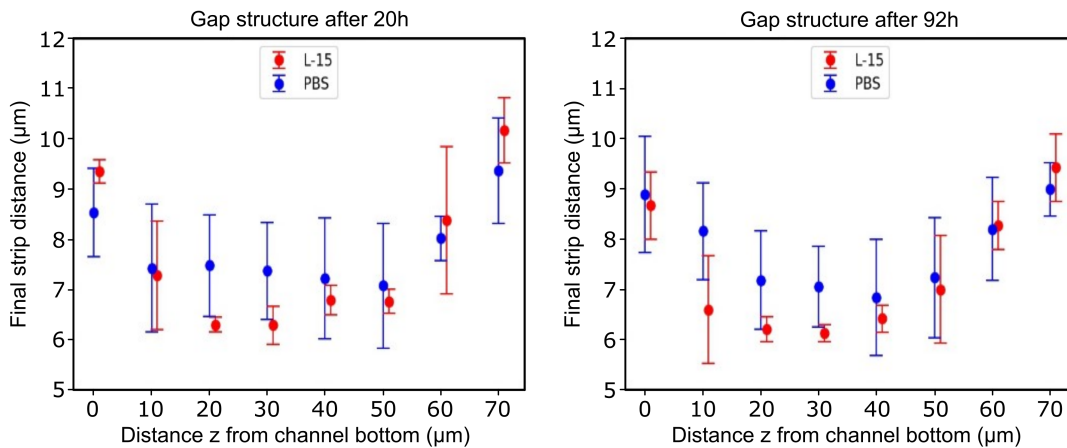


Figure 4.4: **Reproducibility and long-term stability of the hydrogel clefts.** 'Sponge clamps' were fabricated under identical conditions and imaged after 20 hours and 92 hours post-fabrication using GFP-labeled Dextran. No significant alterations in the gap morphology were observed over time, with consistency maintained both in terms of batch-to-batch variability and the nature of the employed medium. Reproduced from [183] with permission from the Royal Society of Chemistry.

of hydrogel profiles, 'sponge clamps' with a cross-link ratio of 0.6 and above were examined. Findings indicate a high degree of reproducibility and negligible alterations in the hydrogel clefts for a minimum duration of 92h (see Figure 4.4). Furthermore, the impact of medium constituents on the swelling behavior of hydrogels was investigated. No significant effects of the utilized medium, whether PBS or L-15 cell culture medium, were observed. Subsequently, hydrogels with cross-link ratios lower than 0.6 were excluded from further analysis due to their poor long-term stability.

4.3 Invasion Capacity in Hydrogel Clefts

To validate the suitability of the experimental assay for investigating cell migration dynamics, HT-1080 fibrosarcoma cells were introduced to one side of the clamp, and a chemotactic gradient ranging from 1% to 10% FBS was applied across the gel to induce directed migration into the hydrogel clefts. Cells traversed into the clefts as

single cells, guided by the chemotactic gradient, displacing the gel to pass through (see Figure 4.5). The center of mass of the first cell (leading cell) was tracked over time as a measure for invasion capacity. Evaluation of invasion depth was standardized for each cell trajectory. This involved individually considering the entrance point of each hydrogel cleft, as illustrated by green and cyan bars in Figure 4.5. These bars represent the starting point of the 'sponge clamp' and the leading cells, respectively.

For each cleft within the array, the leading cell trajectory was recorded and col-

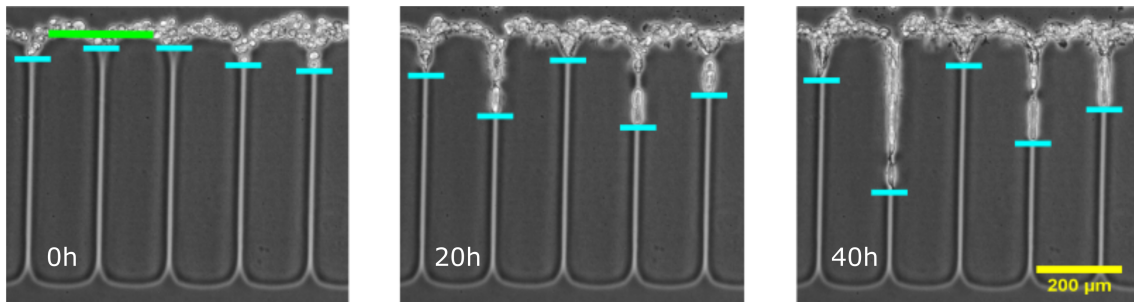


Figure 4.5: **Illustration of the invasion in hydrogel-hydrogel interfaces.** Exemplary time-lapse microscopy images of HT-1080 cells invading the 'spongeclamp'. Reproduced from [183] with permission from the Royal Society of Chemistry.

lectively analyzed. To investigate the influence of environmental factors, various pressurized hydrogel-hydrogel interfaces were created by modifying the cross-linker ratios and initial strip distances. The mean invasion trajectories for different conditions are shown in Figure 4.6A across three distinct gap sizes. It was observed that the average velocity over a 40-hour period systematically increased with the gap size G (see Figure 4.6B). To explore whether cell velocities are also dependent on hydrogel stiffness, the mean velocity was analyzed as a function of cross-linker ratio for a fixed block separation D (see Figure 4.6C). The data reveals a slight decrease in mean velocity with increasing cross-linking ratio. This marginal dependence is likely attributable to the fact that higher cross-linker ratios not only enhance hydrogel stiffness but also diminish swelling, consequently leading to larger gap sizes.

However, when considering larger gap sizes, encompassing both parameters of cross-linker ratio and initial block-to-block distance, the mean velocity is notably more influenced compared to variations in the cross-linker ratio alone. This phenomenon can be attributed to the significantly less hydrogel deformation required for cells to squeeze through the hydrogel-hydrogel interfaces. Moreover, there are examples indicating instances where slight compression of cells enhance their invasiveness compared to an uncompressed state [223]. Thus, it is plausible that at very low levels of compression, cell invasion is limited, but it increases rapidly with slightly higher compression. Conversely, under considerably increased pressure within the clefts, cell invasion may be impeded. This observation could also explain the observed invasion behavior of HT-1080 cells in this work.

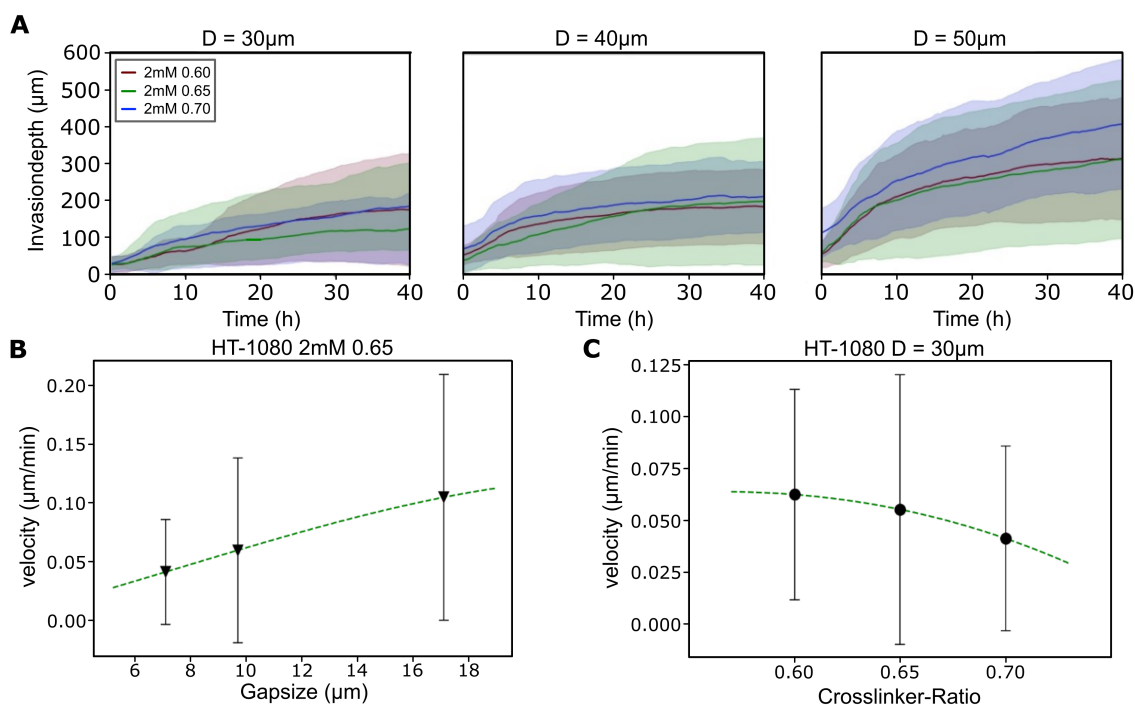


Figure 4.6: **Characterization of the invasion capacity of cancerous cell lines within hydrogel clefts exhibiting different mechanical properties.** (A) Representation of the average cell trajectories of HT-1080 cells migrating into hydrogel-hydrogel interfaces, producing through modifications in hydrogel compositions and employing three distinct initial strip distances (with $n > 40$ clefts per 'sponge clamp' condition, mean \pm SD). (B) The rate of invasion by HT-1080 cells demonstrates a positive correlation with the gap size of the 'sponge clamp' (with $n > 40$ clefts per initial strip distance, mean \pm SD). (C) Invasion velocity of HT-1080 cells as a function of cross-linker ratio (with $n > 40$ clefts per hydrogel composition, mean \pm SD). Reproduced from [183] with permission from the Royal Society of Chemistry.

To further validate the versatility of the 'sponge clamp', we compared the invasion dynamics of MDA-MB-231, a human breast adenocarcinoma cell line, to that of HT-1080 fibrosarcoma cells. Both cell types are known for their high invasiveness, both with and without proteolytic digestion of their surround matrix [73,224]. Once again, three cross-linker ratios were employed for a fixed initial block-to-block distance ($D = 50 \mu\text{m}$) to generate pressurized hydrogel-hydrogel interfaces. Across all tested conditions, HT-1080 migration exhibited significantly higher velocities during the initial hours of the experiment compared to MDA-MB-231 cells (see Figure 4.7). Consequently, the final invasion depth of HT-1080 cells after 60 hours surpassed that of MDA-MB-231 cells due to the slower invasion speed during the initial hours. Several factors may account for this discrepancy. Differences in cell migration mechanisms between the entry and narrowing channel phases could contribute, with adaptation to channel constraints being more critical during the entry phase. Additionally, slower initial cell migration rates may result from cellular stress induced by the detachment procedure using trypsin solution, which disrupts crucial

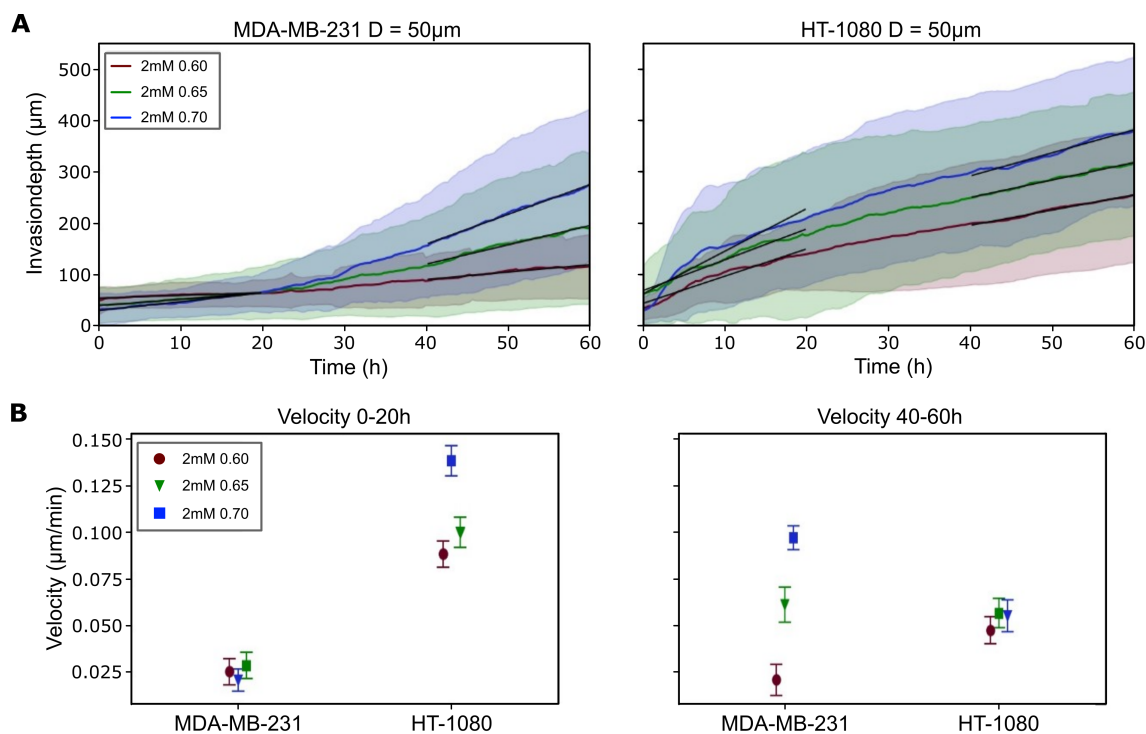


Figure 4.7: **Comparison of migration dynamics between two distinct cancer cell lines invading hydrogel-hydrogel interfaces.** (A) Evaluation of invasion depth exhibited by MDA-MB-231 and HT-1080 cells invading hydrogel clefts with diverse mechanical properties (with $n > 40$ clefts per hydrogel composition, means \pm SD). (B) Separation of cell velocity across distinct time intervals (entering phase: 0-20h, migration phase: 40-60h). The dependency of velocity on cross-linker ratio varies between MDA-MB-231 and HT-1080 cells during the entry phase compared to the migration phase (with $n > 20$ clefts per hydrogel composition, means \pm SD). Reproduced from [183] with permission from the Royal Society of Chemistry.

cell-surface interactions, including integrins, necessary for effective migration [225]. Furthermore, Lautscham et al. demonstrated that a smaller fraction of MDA-MB-231 cells compared to HT-1080 cells entered narrow constrictions formed in PDMS, although invasion depth and speed were comparable [73].

To further quantify cell velocity, we divided the invasion process into entering (0-20 hours) and migration phases (40-60 hours). Interestingly, MDA-MB-231 cells exhibited consistent invasion speeds across all tested conditions during the entering phase, while HT-1080 cells displayed a dependency on hydrogel conditions, migrating significantly faster overall compared to MDA-MB-231 cells (see Figure 4.7B). Thus, the initially low mean invasion rate of MDA-MB-231 cells may be attributed to non-invading cells blocking cleft entrances until a highly invasive cell successfully enters and migrates effectively. However, during the migration phase, MDA-MB-231 cells were more sensitive to experimental conditions compared to HT-1080 cells, suggesting that MDA-MB-231 migration behavior is influenced by changes in ECM properties. Another potential explanation for these distinct behaviors could be the

fact, that MDA-MB-231 cells form multicellular streams while HT-1080 cells squeeze through as single cells (see [183] for further details). These morphological differences correlate with the observed migration velocities of both cell lines.

4.4 Discussion

This work presented here, describes the fabrication of microstructured clefts composed of synthetic PEG-NB-based hydrogels and demonstrates their applicability in investigating the invasiveness of cancer cells. The migratable hydrogels were fabricated by employing photolithographic patterning of hydrogel blocks within microchannel slides. Subsequently, the interstitial space was closed through swelling, resulting in 'sponge clamp' structures, where the hydrogel blocks are compressed against each other. We modulate the mechanical properties of the clefts through variations in the off-stoichiometric amount of cross-linker PEG-dithiol and the absolute PEG-NB concentration. Additionally, the hydrogel facilitates cell adhesion through the incorporation of CRGDS peptide sequences. The versatility of this experimental assay for cell migration investigation was demonstrated by seeding invasive HT-1080 and MDA-MB-231 cells in the channel, coupled with the application of a chemotactic gradient. Our findings indicate that MDA-MB-231 cells are influenced by the hydrogel composition compared to HT-1080 cells, highlighting the increased sensitivity of MDA-MB-231 cells to the stiffness of the surrounding ECM when traversing through tight constrictions. These observations align with previous studies demonstrating a correlation between the migration behavior of MDA-MB-231 cells and ECM stiffness [22, 72, 73].

In general, various cell invasion assays are available and established to quantitatively assess cell migration. Among these, the Boyden chamber is the most prominent, utilizing a porous membrane with pore diameters typically ranging from 3 to 12 μm . Cells transmigrate from an upper reservoir to a lower reservoir in these chambers, where they are subsequently counted. Boyden chambers find wide application in studies of invasive cell migration, with specific mechanical properties such as membrane thickness and well-defined stiffness [226, 227]. In contrast, the 'sponge clamp' assay introduced in this work offers a tunable cleft length. Moreover, the mechanical stiffness of the clefts can be adjusted within the soft tissue range, and the adhesiveness of the environment can be modulated by varying the amount of CRGDS peptide sequences employed. Notably, the interplay between the cross-linker ratio and the initial block-to-block distance permits precise tuning of ECM properties over a broad spectrum. Regarding readout, while the Boyden chamber relies on the total number of transmigrated cells following a designated timeframe, the 'sponge clamp' enables visualization of the invasion process, providing trajectories and velocities of invading cells via image analysis. This readout method is commonly utilized in the cell migration research community, facilitating comparability with other experimental designs. Furthermore, this introduced experimental assay holds potential for extension and integration with the Traction-Force-Microscopy (TFM) technique in three dimensions by incorporating small, fluorescent nanobeads into the hydrogel as a TFM readout. Given that the hydrogel stiffness of the

assay is within the range of soft tissue, such data is suitable for inferring forces typically exerted by cells *in vivo*. This approach has the potential to shed light into the ongoing debate concerning the role of the nucleus during transmigration through 3D constrictions. Previous studies have highlighted the significance of the nucleus, as the stiffest and largest organelle, in 3D confined cell migration [19,26,30,120]. This topic will be investigated in detail in the following chapter.

5. Migration of Cells in Dumbbell-shaped Hydrogel Cavities

In the previous chapter, we established an experimental methodology utilizing PEG-NB hydrogels to investigate cellular invasion through confined hydrogel interfaces, under the influence of chemotactic gradients. However, this assay presents challenges for quantitatively assessing self-directed confined cell motility and its association with nuclear dynamics, due to its complex experimental setup and the lack of scalability for high-throughput analysis. To address these limitations, we build on a valuable experimental approach introduced by Brückner et al. [23], which examines the stochastic migration of cells within structured surroundings. This involves the fabrication of a micropattern comprising two square adhesive islands connected by a narrow bridge, thereby establishing a minimal two-state framework for investigating confined cell migration in two dimensions.

In this chapter, we extend this experimental methodology to facilitate the investigation of 3D confined cell migration. This expansion offers the benefits of simplicity and minimalism inherent to the 'dumbbell-shape' experimental configuration, facilitating high-throughput data acquisition. Essentially, these dumbbell-shaped structures comprise cavities surrounded by a layer of PEG-NB hydrogel, replicating physiological scenarios where cells encounter 3D constriction. Consequently, this assay represents a three-dimensional and deformable extension of the flat microcontact printed dumbbell pattern employed in prior investigations [23, 117, 228]. The fabrication process relies on PEG-NB hydrogels polymerized via maskless photolithography to achieve a resolution suitable for narrow constrictions measuring a few microns in width. Subsequently, time-lapse phase-contrast microscopy is utilized to observe the iterative migration of cells between cavities via deformable channels of predefined dimensions. This innovative approach enables the investigation of 3D confined cell migration dynamics, particularly shedding light on the role of the nucleus, the largest and stiffest organelle within the cell. Prior investigations have identified nucleus translocation as the bottleneck during migration through narrow 3D constrictions, necessitating nuclear deformation [25, 26]. However, the impact of physical confinement on cellular dynamics remains incompletely understood, particularly concerning dynamic alterations across a broad spectrum of constriction widths. This chapter is largely based on the publication by Stöberl et al. [183].

5.1 Microfabrication of Hydrogel-Based 3D Assays

For the quantitative analysis of self-imposed confined cell migration, artificial microfluidic assays are commonly employed. Notably, microfabricated hydrogel-based migration assays [118, 229–231] and transwell migration assays [29, 232, 233] have emerged as valuable tools for elucidating the impact of nuclear mechanical properties on cell migration and viability at the single-cell level. Long, linear PDMS channels are frequently utilized to explore the migration dynamics of cells physically confined within a precisely controlled experimental environment. However, for

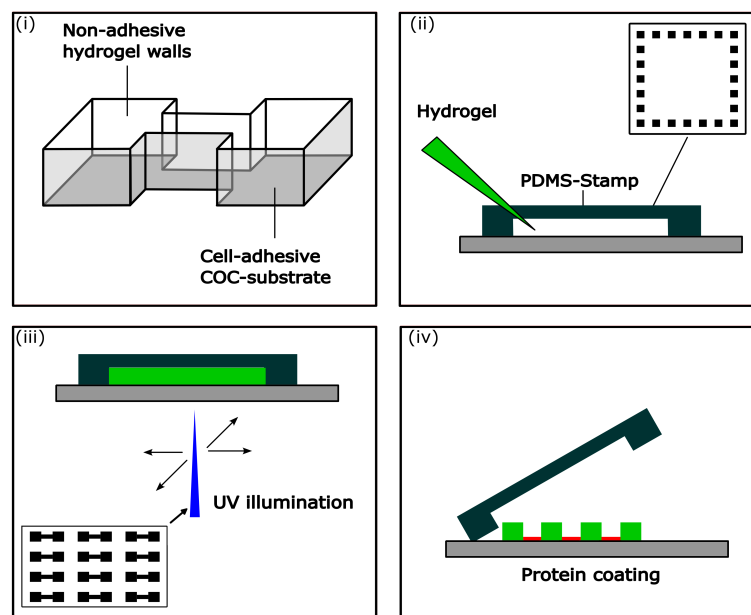


Figure 5.1: **Schematic depiction of the fabrication process of 3D dumbbell-shaped micro-cavities.** Visualization of the final assay containing non-adhesive walls and a cell-adhesive substrate (i). A PDMS stamp provides a precise thickness of the hydrogel layer (ii), which undergoes polymerization through UV-lithography (iii). Stamp is removed, and the substrate is subjected to incubation with an ECM protein (iv). Figure adapted from [135].

the investigation of cell entry into constrictions, the use of short circular pillar-lined PDMS channels has proven pivotal [20]. Such channels enable the study of confinement effects on migration dynamics without inducing significant alterations in the overall migration mode, as elongated channels might trigger mesenchymal-amoeboid transition [22].

In this study, our objective is to integrate the advantages offered by the 'dumbbell-shape' experimental assay introduced by Brückner et al. [23], with the more physiologically relevant conditions afforded by 3D confinement, to quantitatively explore the influence of physical confinement and nuclear deformation on cell migration dynamics. To this end, we developed a hydrogel-based migration assay to conduct

high-throughput experiments on cell migration within a precisely controlled geometric environment.

Our experimental setup involves the utilization of 3D dumbbell-shaped micro-

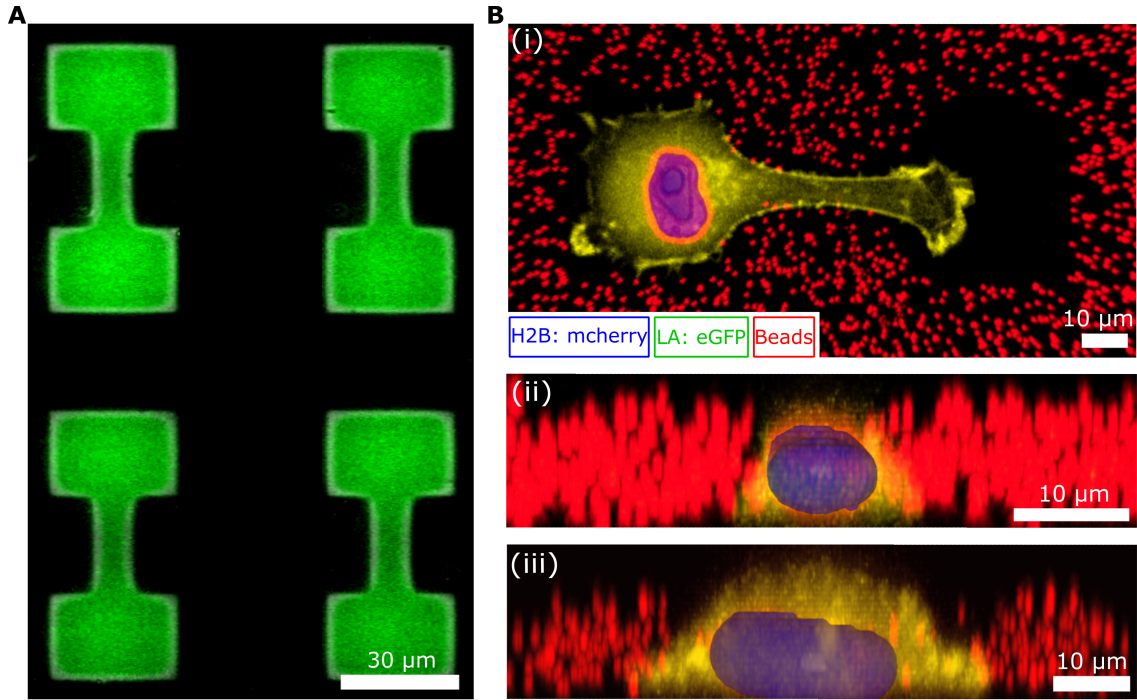


Figure 5.2: **Microscopic characterization of the 3D dumbbells.** (A) Representative confocal microscopy images show a MDA-MB-231 cell co-expressing fluorescently labeled histones (mcherry-H2B, blue) and F-actin (LifeAct-TagGFP2, green) while confined within the cavity, as shown in (i)-(iii). Given the non-adhesive property of the hydrogel, cell adhesion is solely restricted to the substrate. (i) Top view of the dumbbell-shaped cavity; (ii) cross-section through the channel; (iii) cross-section through an island. (B) Representation of the ECM protein coating by utilizing labeled fibronectin. Figure adapted from [135].

cavities incorporated within a 20 μm thick layer of PEG-NB hydrogel (see Figure 5.1A). The experimental protocol employs commercially available imaging dishes (μ-Dish 35mm, ibidi). To achieve a defined height for the hydrogel layer containing the desired structures, PDMS stamps are employed. The stamp architecture comprises small pillars that create a gap between the substrate and the stamp, which is subsequently filled with the hydrogel precursor (see Figure 5.1(ii)). The hydrogel precursor utilized here comprises 8-arm PEG-NB cross-linked by PEG-dithiol. Modulating the concentration of PEG-NB and adjusting the amount of cross-linker enables the tuning of the stiffness of the resultant hydrogels, as discussed in section 4.1. Additionally, the hydrogel precursor includes the photo-initiator LAP to facilitate UV-induced polymerization. Following to the infiltration of the hydrogel precursor into the free space of the PDMS stamp, selective photo-patterning of the hydrogel precursor was achieved using the PRIMO module (Alvéole) with the pattern provided in the inset of Figure 5.1(iii) (further information of the dumb-

bell dimensions are provided in **Appendix A**). Thus, the whole hydrogel except for the dumbbell-shaped regions undergoes illumination, resulting in the formation of dumbbell-shaped cavities within the hydrogel layer. Subsequent to exposure, the stamps were removed, and the imaging dish was incubated with an ECM protein (see Figure 5.1(iv)). Following, the bottom of the cavities was coated with fibronectin to enhance cell adhesion, while the PEG-NB hydrogel remains non-adhesive to cells. The selective coating of ECM protein is shown in Figure 5.2A using fluorescently labeled fibronectin. Additionally, fluorescent nano-beads were incorporated into the hydrogel precursor. Their diameter, being 200 nm, contrasts with the relatively smaller mesh size of the hydrogel network, typically in the tens of nanometers, resulting in the embedding of these nano-beads within the hydrogel post-polymerization (see Figure 5.2B). These nano-beads serve as markers for assessing forces exerted by cells on their surroundings based on the elastic deformation field of the walls, a concept that will be elaborated in chapter 6. Overall, this experimental configuration facilitates the investigation of 3D confined cell migration in a high-throughput manner, with cells consistently maintained within the cavity walls throughout the experiments (see Figure 5.2B (i)-(iii)). Notably, despite complete deformation within the narrow channel, the nucleus remains contained within the hydrogel layer and does not spill over.

5.2 Cell Dynamics in 3D Confinement

Time-lapse microscopy is employed to investigate the repeated migration of cells traversing from one cavity side to another through the deformable channel of a defined width. Within the 3D dumbbells, metastatic human breast cancer cells (MDA-MB-231) migrate spontaneously in a mesenchymal mode within the micro-cavities (see Figure 5.3). At the entrance of the narrowing channel, lamellipodia-like protrusions are repeatedly initiated, occasionally progressing into sustained larger protrusions. While some protrusions swiftly retract, others extend into the adjacent unoccupied cavity. Within the new cavity, the protrusion expands with an almost half-circular shape, which ultimately results in the transition of the cellular body. Following complete cellular transition, the cytoskeleton's shape and actin distribution become randomized, reverting to a state identical to that preceding the transition. Subsequently, another transition soon follows in the opposite direction, highlighting the repeatable nature of this confined migration process.

Herein, we explore cell migration dynamics in relation to confinement widths by fabricating arrays of 3D dumbbells with channel widths spanning a broad range from 4 to 35 μm . The average nuclear width outside the channel measures $11.62 \pm 0.01 \mu\text{m}$, derived from averaging across various geometries and cells at different stages of the cell cycle. For channel widths exceeding this threshold (see Figure 5.3 lowest row), cells typically enter the channel without necessitating nuclear deformations.

In this scenario, migration within the channel exhibits limited persistence, with some cells even altering their direction of motion mid-channel without traversing to the opposite side of the pattern. In channels of intermediate widths smaller than

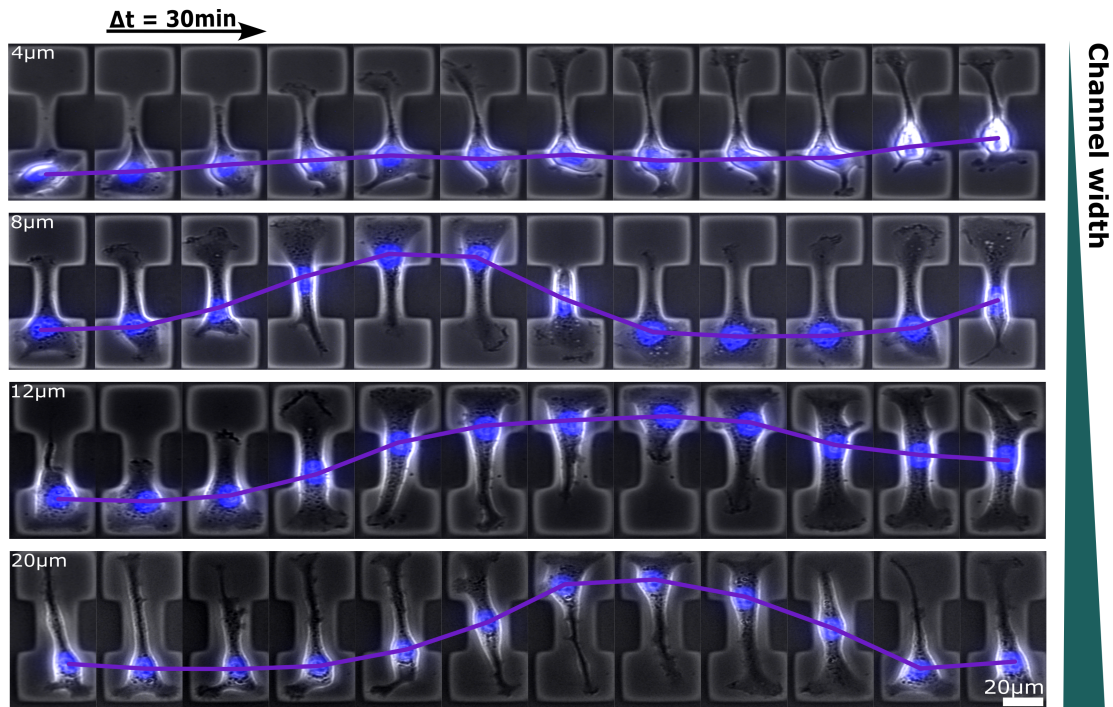


Figure 5.3: **Exemplary time-series of MDA-MB-231 cells.** Cells migrating through dumbbell-shaped cavities with varying constriction width (width = 3-35 μm). Figure adapted from [135].

the nuclear width, cells undergo significant nuclear deformation. Following nuclear reshaping, nearly all cells consistently migrate to the adjacent chamber. Conversely, in the narrowest channel (see Figure 5.3, upper row), unsuccessful attempts at nuclear translocation are frequently observed. In channels where the nucleus becomes constrained ($<12 \mu\text{m}$), we note an increased proportion of 'trapped' cells, characterized by the presence of protrusions extending to the opposite side of the pattern but an inability to relocate their nucleus into the channel. Our findings do not indicate a specific threshold width below which migration is entirely inhibited, but rather a gradual decrease in the proportion of migratory cells with diminishing channel width. Furthermore, when transitions necessitate extensive nuclear deformations, migration behavior markedly differs from that observed on flat micropatterned 2D dumbbells, where frequent transitions were previously noted, even for the narrowest bridge widths [116]. This observation highlights the qualitative alteration in cell translocation dynamics induced by 3D confinement.

To further investigate this, we assess the probability distribution of nuclear positions within our micro-cavities, the mean velocity at the center of the channel, and the transition rates across varying channel widths (see Figure 5.4B). In the absence of confinement, the nuclear position distribution along the longitudinal axis of the pattern is predominantly uniform across significant portions of the micro-cavity. As channel widths diminishes, the distribution undergoes a transition to a double peaked distribution, with maxima within the chambers and a distinct local mini-

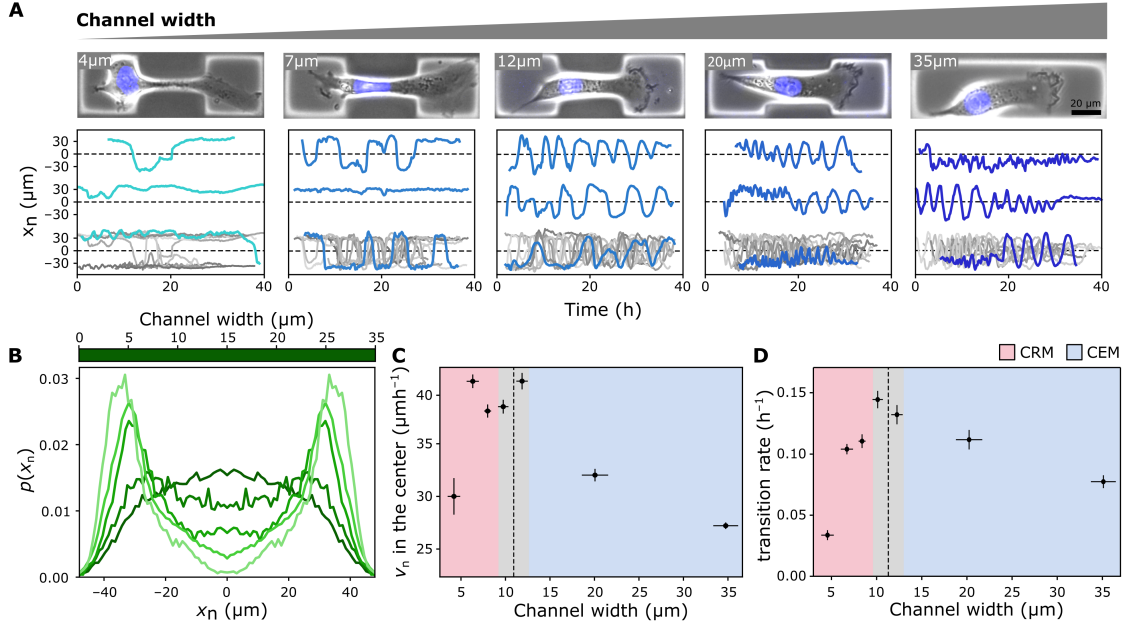


Figure 5.4: **Cell migration statistics for varying channel widths.** (A) Representative examples of cell trajectories for different channel widths (from left to right: 4 μm , 7 μm , 12 μm , 20 μm , 35 μm). (B) The distributions of nuclear position x_n across varying channel widths. (C) Average velocity within the central region of the pattern ($|x_n| \leq 6 \mu\text{m}$). Maximal velocities are observed at an intermediate channel width comparable to the nuclear width. (D) Transition rates across different channel widths. Analogous to nuclear velocities, the highest transition rates occur at intermediate channel widths. (C) and (D): The red region indicates the regime of confinement-reduced migration (CRM), while the blue region indicates confinement-enhanced migration (CEM). The dashed line indicates the average nuclear width and the grey region denotes one standard deviation. Error bars associated with the x-axis represent the standard deviation, while those associated with the y-axis represent the standard error. Figure adapted from [135].

num located at the centre of the constraining channel. However, even for channel widths as narrow as 4 μm , considerably smaller than the average nuclear diameter, instances of cells successfully traversing their nucleus through these notably constricted passages are observed.

Interestingly, we observe a non-monotonic relationship between the average velocity and channel width, exhibiting a peak at a confinement width comparable to the undeformed nuclear diameter (see Figure 5.4C and D). The overall transition kinetics governing cell entry into and migration through the narrowing channel, quantified through the transition rate, displays a similar biphasic dependence on channel width. When starting from the unconfined scenario and progressively reducing channel width, an initial increase in transition rate is observed, succeeded by a sharp decline at channel widths smaller than the nuclear dimensions. We term these phenomena as the 'confinement-enhanced migration' (CEM) and 'confinement-reduced migration' (CRM) regimes, respectively. These findings illustrate the impact of con-

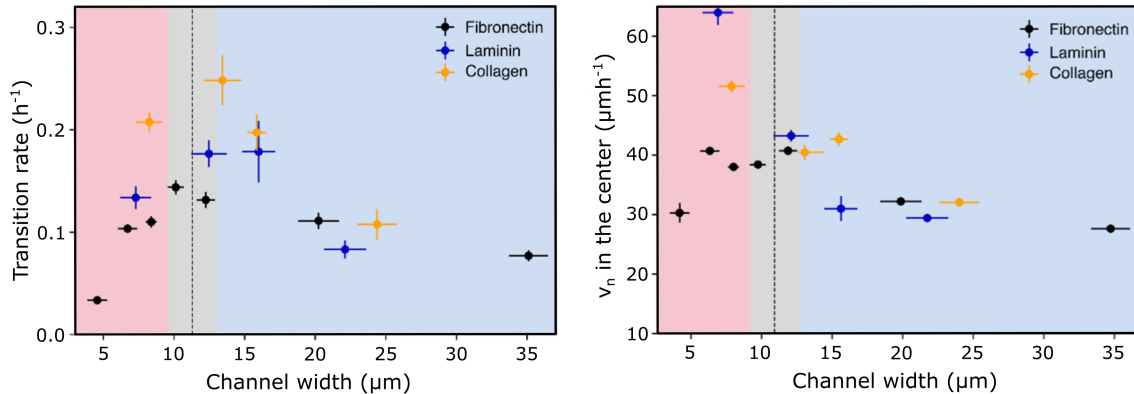


Figure 5.5: **Cell migration statistics with different surface coatings.** Transition rates on laminin, collagen and fibronectin coated patterns show a similar biphasic channel width dependence. The nuclear velocities in the centre of the channel are largely independent of the surface coating at wider channel width, but appear to be higher at lower channel width on patterns with laminin and collagen coating. Figure adapted from [135].

finement on cell migration behavior, wherein it either augments transition rates at wider channel widths or significantly impedes transitions when cells encounter the necessity to physically deform their nuclei within tight constrictions, as observed in prior studies [21, 26].

In order to generalize our findings on cell dynamics, especially the non-monotonic dependence of average velocity and the biphasic dependence of transition rates on channel width, we conducted supplementary experiments. These experiments employed additional ECM protein coatings, laminin and collagen, to further investigate these phenomena. Laminin, a prominent constituent of basement membranes in animal tissues, is commonly utilized in cell culture to coat surfaces, facilitating enhanced attachment and motility in certain cell types. Collagen, comprising a substantial portion of mammalian proteins, provides structural integrity and resilience in tissues, and in cell culture, it serves as a medium for studying cell growth, differentiation, and migration [234] (see Figure 5.5). Consistent with our observations with fibronectin, all scenarios exhibit biphasic transition rate behavior. However, quantitatively, transition rates vary among the ECM proteins utilized, potentially due to differing concentrations of the ECM and the diverse effects of different proteins on cell motility. Notably, we observe a divergence in the behavior of average velocity concerning channel width compared to cells on fibronectin coating. This discrepancy could arise from the limited data available for these additional ECM coatings relative to the extensive trajectory dataset obtained for fibronectin, particularly concerning narrow constrictions.

5.3 Inferred Non-Linear Dynamics of the Nucleus

To gain better insights into the influence of the nucleus on the overall migration behavior under confinement, we adopt the methodology introduced in section 2.2, employing data-driven, top-down models to inform the development of more mechanistic, bottom-up models. While for the case of 2D migration, detailed, data-driven models for the emergent migration behavior have been established previously, this is not the case for migration in 3D confinement. Here, we leverage the statistical properties of nuclear velocities and transition rates obtained from our high-throughput experimental assay. Utilizing the recorded nuclear trajectories, we infer a stochastic dynamical model for the confined migration process, facilitating the separation of deterministic and stochastic components of the dynamics. As discussed in section 2.2, the dynamics of the nucleus of a migrating cell along the longitudinal axis of 2D dumbbell-shaped patterns can be represented in terms of the underdamped Langevin equation.

$$\frac{dv_n}{dt} = F_w(x_n, v_n) + \sigma_w \xi(t), \quad (5.1)$$

where $F_w(x_n, v_n)$ characterizes the deterministic acceleration of the nucleus contingent upon its position x_n and velocity v_n within a confinement of width w , while the Gaussian white noise $\xi(t)$ of strength σ_w accounts for the stochastic nature of cell migration. Here, we extend this methodology to three-dimensional two-state patterns, yielding a systematically constrained top-down model of confined cell migration that comprehensively captures the migration dynamics across varying confinement widths. Given the continuous range of channel widths resulting from the experiments, we bin the data based on the measured width of the pattern in the centre of the channel.

In this manner, we ensure sufficient data availability for each investigated channel width to constrain the terms outlined in Eq. (5.1) (additional information regarding the total number of analyzed cells and bin size is provided in **Appendix B**). Subsequently, we employ the Underdamped Langevin Inference (ULI) algorithm [228] to derive an estimator for $F_w(x_n, v_n)$ from experimental trajectories. Further discussion on the free parameters and model selection is available in the Supplementary Materials of [183].

In order to elucidate the impact of 3D confinement, particularly nuclear deformations, on the non-linear migration behavior of cells, we focus on channel widths equal to or less than 12 μm (see Figure 5.6). Within this range, we observe a transition from transmigration devoid of nuclear deformation ($w = 12 \mu\text{m}$) to pronounced nuclear deformations induced by the confinement ($w < 12 \mu\text{m}$). For channel widths $w \geq 7 \mu\text{m}$, we discern qualitatively similar patterns: The nucleus experiences significant deceleration when positioned near the center of the chambers. Conversely, as the nucleus approaches the constraining channel, it accelerates towards the channel and traverses to the opposite side of the pattern. These obtained non-linear dynamics are qualitatively similar to those observed on 2D micropatterns [23]. Intriguingly, at the narrowest width (4 μm) this acceleration region dissipates, aligning with the

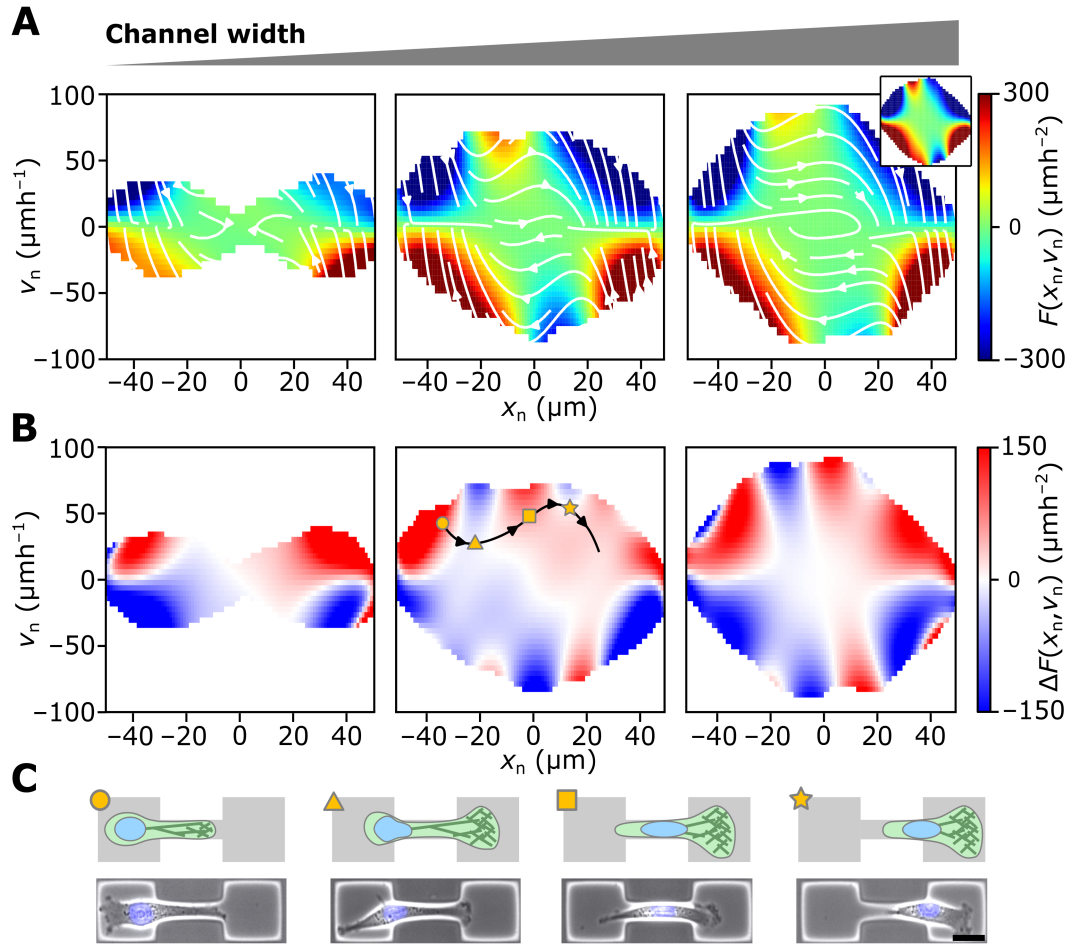


Figure 5.6: **Inferred non-linear dynamics of the nucleus for varying channel widths (from left to right: 4 μm, 7 μm, 9 μm).** (A) The inferred deterministic term $F_w(x_n, v_n)$ within the experimentally sampled region (see Supplementary of [135] for further details). The outer white region is not sampled in the experiments. Right inset: $F_w(x_n, v_n)$ for a channel width of 12 μm. (B) The difference between the deterministic term $F_w(x_n, v_n)$ and the reference term at 12 μm (‘Nuclear Confinement Maps’). The black indicates an exemplary trajectory of a transitioning cell. (C) Snapshots of the typical cellular morphology at different points during the transition as indicated in (B). Figure adapted from [135].

more stationary behavior observed in the experimental trajectories at this channel width. Although we observe both quantitative and qualitative differences among the inferred deterministic terms $F_w(x_n, v_n)$ of the underdamped Langevin dynamics (see Figure 5.6A), discerning a clear signature of increasing confinement through simple visual comparison proves challenging. To facilitate a clearer visualization of the influence of nuclear deformations on the non-linear dynamics, we compute the difference $\Delta F_w = F_{12\mu\text{m}} - F_w$ for comparison with the channel width $w = 12 \mu\text{m}$, below which notable nuclear deformations emerge. This comparison, termed ‘Nuclear Confinement Maps’ (NCM), offers enhanced clarity for interpreting the effects

of nuclear deformations on migratory behavior.

Across all three examined channel widths, the NCMs exhibit several shared qualitative attributes: A cell traversing along a typical trajectory from the left to the right chamber (depicted by the black line in Figure 5.6B, center) starts in a region characterized by $\Delta F_w > 0$ (circle in Figure 5.6B and C). In prior investigations, it was established that on 2D micropatterns, increased confinement of the protrusion stimulates enhanced protrusion growth, consequently resulting in stronger accelerations of the nucleus towards the channel [116]. This distinct region of $\Delta F_w > 0$ may potentially signify the presence of this 'geometry adaptation' mechanism within 3D confinement as well. Upon narrowing the channel, the nucleus transitions into a region of $\Delta F_w < 0$ in the NCM (indicated by the triangle in Figure 5.6B and C). Given that the region of $\Delta F_w < 0$ corresponds to the point where further migration necessitates substantial nuclear deformations, it is plausible that this characteristic of the NCM arises from an effective deformation energy barrier hindering entry into the channel. Subsequently, as the nucleus is guided into the channel, a subsequent region of acceleration is observed (square in Figure 5.6B and C), consistent with the elastic release of tension accumulated during the previous deformation step. Upon achieving sufficiently high velocities, cells traverse through another region characterized by $\Delta F_w < 0$ (star in Figure 5.6B and C) as they exit the channel. Overall, the NCMs reveal a distinct qualitative signature of 3D nucleus confinement, suggesting that elastic nucleus deformations influence transmigration dynamics.

5.4 Discussion

In this chapter, we introduced a novel experimental approach utilizing hydrogel-based systems to investigate high-throughput 3D confined cell migration. This methodology builds upon the two-state system by Brückner et al. [23] for exploring confined cell migration in two dimensions. The fabrication process relies on maskless photolithography of PEG-NB hydrogels, offering a high versatility of the final experimental setup. Variation in the hydrogel composition, particularly the total concentration of PEG-NB and the off-stoichiometric ratio of the crosslinker, enables manipulation of the elasticity and swelling characteristics of the polymerized hydrogel. This allows us to mimic diverse physiological extracellular matrices. Moreover, the utilization of maskless photolithography enables for the polymerization of basically any desired pattern with a resolution of up to 2 μm . Additionally, incorporating fluorescent nanobeads within the hydrogel can serve as a readout for forces exerted on the hydrogel by cell nuclei traversing narrow constrictions, a topic that will be thoroughly discussed in chapter 6 focusing on the mechanical properties of the cell nucleus.

To investigate the role of the nucleus in confined cell migration, we conducted high-throughput time-lapse experiments under consistent conditions, varying only the width of the constriction. With these experiments, we examined the repeated self-imposed migration of individual cells through compliant 3D channels, a process requiring robust and reversible nuclear deformations, particularly at narrow channel widths. The physical constrictions present in the channel exert a multifaceted

influence on cell dynamics. On one hand, in the CEM regime, the transition rate increases, while on the other hand, in the CRM regime, the transition rates sharply diminish due to the requisite nuclear deformations required by constrictions narrower than the nuclear diameter. In this context, we elucidated the dynamics of the migrating cell nucleus along its longitudinal axis through the underdamped Langevin equation. To gain insights into how 3D confinement, particularly nuclear deformations, impact non-linear migration behavior, we focus on channel widths equal to or less than 12 μm . Within this range, we compute 'Nuclear Confinement Maps' which illustrate a notable deceleration during the nucleus entry phase into the channel, succeeded by an acceleration upon exiting the channel. These maps highlight a clear qualitative signature of 3D nucleus confinement, suggesting that elastic nucleus deformations influence transmigration dynamics. To comprehensively understand these non-linear migration dynamics, it is necessary to investigate nuclear mechanics and deformation during transmigration and subsequently construct a bottom-up mechanistic model capable of explaining the observed effects of 3D confinement.

In summary, this innovative experimental platform presents versatile opportunities for investigating physically constrained cell migration in a high-throughput manner. In this study, statistical data were collected from hundreds of cells. The well-defined structures within the hydrogel layer effectively confine cells within the cavities, facilitating straightforward migration analysis. The feasibility of employing different ECM protein coatings on the substrate is highlighted by additional experiments, which reveal qualitatively consistent bi-phasic behavior in cellular transition rates. For future research, fabricated PDMS stamps with varying dimensions to produce hydrogel layers with increased thickness could be used to study the interactions of multiple cell layers in confinement. However, a future challenge would be to adapt these experimental systems to mimic full 3D confinement. Currently, cell adhesion and migration are restricted to two dimensions along the substrate, and the dumbbell-shaped cavities lack a ceiling. Therefore, further system improvements could include incorporating an additional step in the fabrication process to embed the seeded and adhered cells in another ECM component such as Matrigel, or exploiting the functionality of PEG-NB hydrogels by incorporating RGD ligands to facilitate cell adhesion to the walls of the narrow channels. However, a potential drawback of this approach is the risk of cell escape from the cavities, which could be mitigated by sealing the cavities with a coverslip containing a thin layer of the same PEG-NB hydrogel composition, thus providing consistent conditions for the cells in all three dimensions.

6. Mechanical Properties of Cell Nuclei in Compliant Constrictions

In the previous chapter, we conducted an analysis of cell dynamics within compliant 3D hydrogel cavities across a wide spectrum of confinement widths, revealing a bi-phasic behavior in transition rates that peaks approximately at the nuclear diameter. These findings, consistent with previous investigation, highlight the significance of the nucleus in cellular behavior, particularly concerning its mechanical characteristics [26]. The nucleus exhibits considerable variability in size and shape across different cell types, influencing its response to mechanical stimuli. Larger nuclei generally exhibit more resistance to deformation, while nuclei with elongated or irregular shapes may display distinct mechanical behaviors when subjected to external forces. The stiffness of the nucleus is predominantly determined by factors such as the composition and organization of the nuclear envelope, chromatin structure, and nuclear lamina (see section 2.3) [128, 235]. A stiffer nucleus resists deformation more strongly, impacting cellular responses to mechanical cues and the ability to migrate through confined spaces.

Additionally, the nucleus demonstrates viscoelastic properties, displaying both elastic and viscous responses to applied forces over time. This viscoelastic behavior arises from complex interactions among nuclear components, including the nuclear envelope, chromatin, and nucleoplasm [24, 236]. Viscoelasticity influences the nuclear capacity to deform and regain its original shape during cellular processes such as migration and mechanotransduction [237]. Notably, a significant viscous response may lead to a memory effect, wherein the nucleus retains a degree of deformation, potentially influencing subsequent migration behaviors. Furthermore, the nuclear lamina plays a pivotal role in determining the mechanical properties of the nucleus by providing structural support [29, 238]. Disruptions to the nuclear lamina can alter the viscoelastic behavior of the nucleus, thereby affecting cellular functions such as migration and gene expression.

In this chapter, we analyze the mechanical properties of the nucleus to gain deeper insights into its role as a limiting factor. Initially, we analyze the nuclear shapes during its transmigration within the 3D-dumbbell cavities and its subsequent recovery, aiming to elucidate the viscoelastic characteristics of MDA-MB-231 cell nuclei. Furthermore, we quantify the comprehensive 3D deformation of the nucleus throughout

the transition process by employing confocal microscopy to capture 4D movies, allowing for the determination of the nuclear volume at each time point. This dataset facilitates the computation of the nuclear Poisson ratio, a key metric for assessing nuclear elastic properties. To determine whether the nuclear mechanical properties are influenced under strong confinement, we measure the forces exerted on the channel walls by transitioning cells. To achieve this, we analyze the indentation of the soft hydrogel walls during transitions by tracking the displacement of fluorescent beads embedded within them. The magnitude of these forces is estimated by using the maximum bead displacement in the PEG-NB hydrogel, with the Young's Modulus independently determined via AFM. This chapter is largely based upon the publication by Stöberl et al. [183].

6.1 Nuclear Shape Recovery of a Cancerous Cell Line

To further investigate the role of nuclear mechanical properties as suggested by the NCMs in the previous chapter, we analyze the nuclear deformations induced by confinement within a channel. The goal was to obtain insights into the viscoelastic characteristics of the nucleus, potentially indicative of cellular memory effect influencing repetitive cell transitions. To this end, we quantified the morphological changes of cell nuclei using the obtained 2D time-lapse microscopy data. The nuclear morphologies were characterized by their aspect ratios, defined as the ratio of the x-dimension to the y-dimension of the nucleus, across varying channel widths. Subsequently, to group aspect ratios across all cells within specific channel widths, cellular orientation was standardized to depict migration from left to right, consistent with the observed migration direction in Figure 6.1A. This separation facilitated the distinction between pre- and post-transmigration nuclear shapes.

This allows the analysis of nuclear recovery following transmigration and its correlation with constriction width. The findings indicate that in wide constrictions, the nucleus undergoes minimal deformation during cell confinement, as depicted by the dark blue curve. However, this slight deformation is noteworthy considering the confinement width of 20.0 μm significantly exceeds the mean nuclear diameter of 11.6 μm . This suggests that even in the absence of physical confinement, forces act upon the nucleus, resulting in its slight elongation during cell transmigration through wide constrictions. With continuous narrowing of the channel, the corresponding aspect ratios of cell nuclei steadily increase upon entry into the channel. Ultimately, for a channel width of 4 μm , the resultant aspect ratio of deformed cell nuclei within the channel nearly doubles compared to the unconfined scenario. Furthermore, upon exiting the constriction, nuclear recovery occurs, leading to the observation that nuclear shapes before and after the transition appear identical (see Figure 6.1A). To achieve this, we analyzed nuclear morphology at intervals of 10 minutes, corresponding to the temporal resolution of the conducted time-lapse experiments. Analysis started at the time point when the cell nucleus remained fully confined but about to exit the channel. Interestingly, nuclear morphology

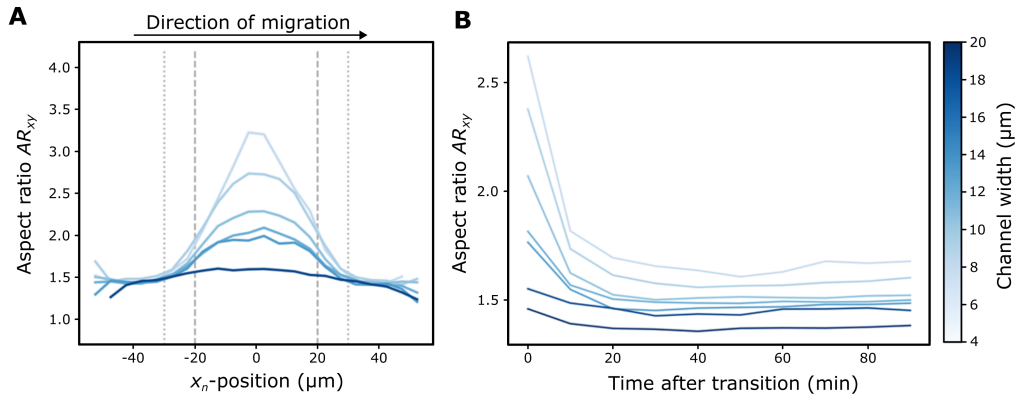


Figure 6.1: **Aspect ratio of the nucleus for different channel widths.** (A) Aspect ratio as a function of nuclear position. Cellular orientation is standardized such that migration occurs from left to right. Grey dashed lines indicate the boundaries of the channel, while grey dotted lines indicate the onset of nucleus entry (left) and complete exit (right). (B) Nuclear shape recovery post-transition. Figure adapted from [135].

rapidly recovers to its original rounded form across the entire range of confinement widths investigated in the experiments. The relaxation time of nuclear shape is approximately 20 minutes post-exit from the channel. Additionally, the width of confinement appears to influence nuclear recovery; wider channels yield a relaxed nucleus with an aspect ratio of approximately 1.4, whereas the narrowest channel results in an aspect ratio of around 1.6 (see Figure 6.1B). These findings suggest that the nucleus of MDA-MB-231 cells exhibits viscous properties. However, this observation implies that within the relevant timescales of our system (hours), nuclear response is predominantly elastic, consistent with the dynamics elucidated in the previous chapter.

6.2 Quantitative Nuclear Volume Analysis

To quantify comprehensive 3D nuclear deformations during transition events, confocal microscopy was employed (see Figure 6.2). Subsequently, cells were examined within dumbbell-shaped cavities via acquisition of 4D movies. At 10-minute intervals, complete z-stacks of the corresponding cells were captured. Utilizing the 'arivis 4D' rendering software (Zeiss), nuclear volume and ellipsoidal main axis were determined. Interestingly, over the experimental duration, a continuous increase of nuclear volume in both relaxed and compressed states was observed on longer time scales. This trend corresponds to a cell growth rate of $1.1 \pm 0.2 \frac{\%}{h}$ (see Figure 6.2A (i)-(iii)). To investigate the overall trend of increasing nuclear volume over time (see Figure 6.2), control experiments involving MDA-MB-231 cells confined within large hydrogel cavities lacking constriction ($50 \times 50 \mu\text{m}^2$) were conducted, yielding a comparable nuclear growth rate of $1.0 \pm 0.5 \frac{\%}{h}$ (see Figure 6.2B (i)-(iii)). Remarkably, examination of the slopes in Figure 6.2A(ii) reveals a notable difference between the

slopes of unconfined states on the island and confined states within the channel. This difference indicates that nuclear volume may not completely restore following cell exit from the channel, potentially explaining the observed flat slope in unconfined states. However, further analysis is required to determine the significance of this phenomenon.

Overall, these evaluations of nuclear volume indicate no significant differences in

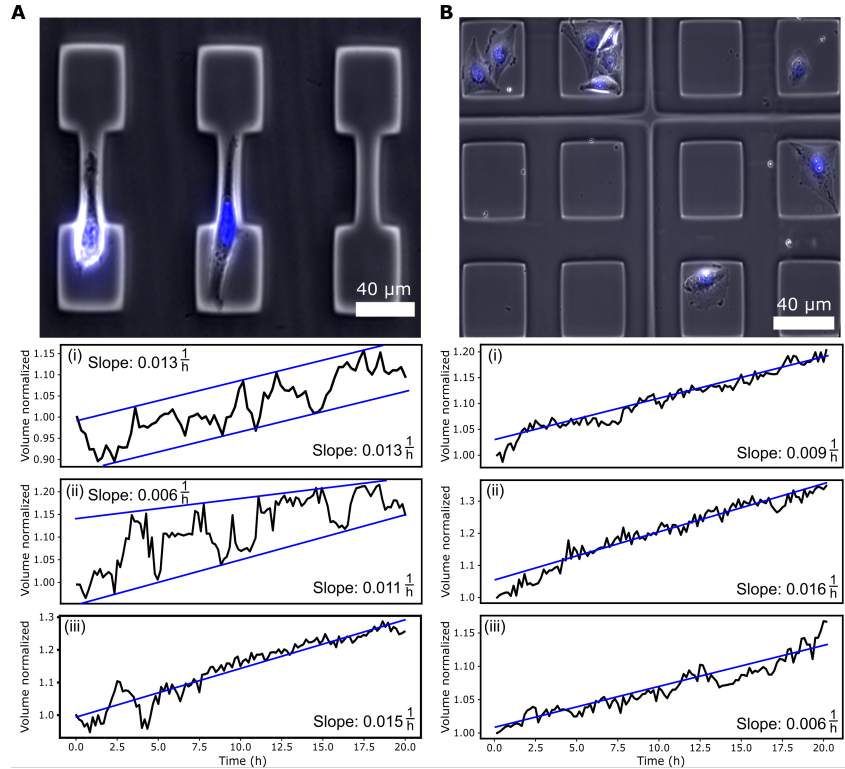


Figure 6.2: **Analysis of nuclear volume alterations over time.** (A) Examination of cells within dumbbell-shaped cavities reveals notable fluctuations in normalized cell volume contingent upon nuclear positioning within the dumbbell structure. Exemplary trajectories depicting nuclear volume variations for cells positioned within dumbbell structures are presented in (i)-(iii). (B) Observation of cell nuclei within hydrogel cavities where cells do not encounter constrictions unveils a consistent increase in normalized cell volume over time. Trajectories illustrating variations in nuclear volume for cells located within hydrogel cavities without constrictions are shown in (i)-(iii). Figure adapted from [135].

the rate of nuclear growth between confined and unconfined conditions. Consequently, the observed increase in nuclear volume over time can be attributed to cellular growth processes.

On shorter timescales, a transient reduction in nuclear volume, up to 11% depending on channel width, is observed upon nuclear entry into the channel. This phenomenon recurs during subsequent transitions. The volume alteration of a material under compression can be quantified by the Poisson ratio ν , where $\nu = 0.5$ denotes an incompressible material, and values below 0.5 indicate volume reduction

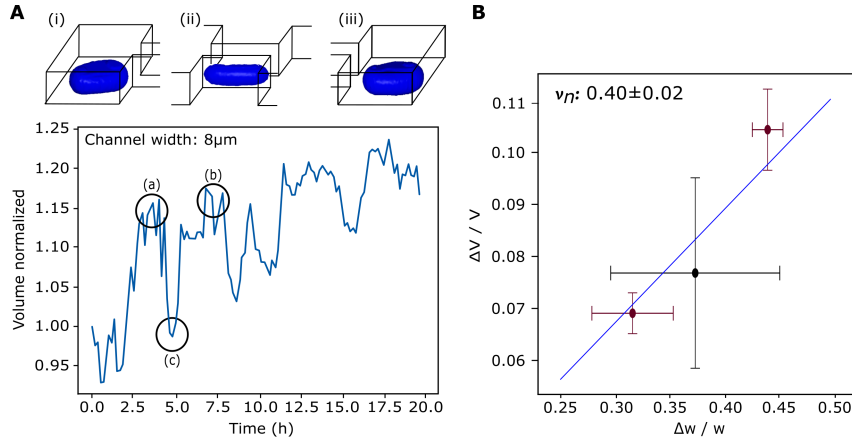


Figure 6.3: **Poisson ratio of MDA-MB-231 cell nuclei.** (A) Quantitative analysis of nuclear volume was conducted utilizing confocal z-stacks captured over a 20-hour period. The nuclear volume demonstrates a decrease under confinement (ii) compared to an unconfined state (i) and (iii). Data acquisition was facilitated by the 'arivis 4D' software. (B) The relative volume change of the nucleus under confinement by channels of varying widths (mean \pm SD, $n_{5\mu\text{m}} = 3$; $n_{8\mu\text{m}} = 4$; $n_{10\mu\text{m}} = 4$ from three biological replicates for each channel width) and fit of an elastic model to derive the Poisson ratio ν of the nucleus (blue line). Figure adapted from [135].

under compression. In the following, we employ the Poisson ratio expression from Eq. (2.22) as the basis for curve fitting to determine the Poisson ratio, utilizing experimental data of relative volume and relative length changes of nuclei for varying channel widths (see Figure 6.3A). For instance, when a cell transmigrates through a 9 μm wide channel, the nuclear volume decreases from 1356 μm^3 in the relaxed state on the island with a nuclear width of 13 μm to 1256 μm^3 and a reduced diameter of 9 μm upon full confinement within the channel. Similarly, for a channel width of 5.6 μm , the nuclear volume decreases from 1792 μm^3 to 1600 μm^3 with an initial nuclear width of 10.2 μm . To determine the standard deviation of the Poisson ratio, error propagation is computed using the variance formula:

$$SD_{\nu_n} = \sqrt{\left(\frac{d\nu}{dV_{rel}}\right)^2 SD_{V_{rel}}^2 + \left(\frac{d\nu}{dW_{rel}}\right)^2 SD_{W_{rel}}^2} \quad (6.1)$$

By converting Eq. 2.13, the Poisson ratio ν_n is given by

$$\nu_n = \left(\frac{1}{2} - \frac{\Delta V}{2V} \frac{W}{\Delta W}\right) \quad (6.2)$$

With the following derivatives of ν with respect to $V_{rel} = \frac{\Delta V}{V}$ and $W_{rel} = \frac{\Delta W}{W}$

$$\frac{d\nu_n}{dV_{rel}} = \left(-\frac{1}{2W_{rel}}\right) \quad (6.3)$$

and

$$\frac{d\nu_n}{dW_{rel}} = \left(\frac{V_{rel}}{2W_{rel}^2}\right) \quad (6.4)$$

we then calculate the standard deviation (SD) of ν_n , which is given by

$$SD_{\nu_n} = \sqrt{\left(\frac{V_{rel}}{2W_{rel}^2}SD_{w_{rel}}\right)^2 + \left(-\frac{1}{2W_{rel}}SD_{V_{rel}}\right)^2} \quad (6.5)$$

This methodology enables the determination of the Poisson ratio of cell nuclei undergoing transmigration through compliant hydrogel channels, closely mimicking physiological scenarios wherein cells migrate spontaneously through narrow constriction. A Poisson ratio ν_n for MDA-MB-231 cell nuclei is derived, yielding $\nu_n = 0.40 \pm 0.02$, independent of channel width (see Figure 6.3B). These findings, together with nuclear shape analysis, suggest that within our experimental framework and relevant timescales, the nucleus exhibits behavior characteristic of a compressible elastic material, as indicated by a Poisson ratio distinct from 0.5.

6.3 Analysis of the Indentation of Hydrogel Walls

To determine the potential impact of strong confinement on nuclear elastic properties, we conducted experiments to measure the force exerted on channel walls by transitioning cells. In this study, we fabricated softer dumbbell-shaped cavities with a total concentration of PEG-NB of 3 mM and an off-stoichiometric crosslinker ratio of 0.4 to enable significant deformation of the hydrogel walls during cell transmigration. The deformation of the soft hydrogel walls during cell transition was analyzed by tracking the displacement of fluorescent nanobeads embedded within the hydrogel matrix (see Figure 6.4A). Quantitative analysis of visible gel deformation was performed using the Python package *TrackPy* [239] to track the positions of the fluorescent marker beads. An exemplary displacement field is depicted in Figure 6.4A, where arrow length and color denote the magnitude and direction of displacement from the neutral position, scaled up twenty-fold for visualization purposes. To investigate the role of friction in this system, observed bead displacements were decomposed into components perpendicular and parallel to the migration direction. The angle ϕ between the perpendicular displacement δ_p and tangential displacement δ_t relative to the migration direction was calculated for further analysis.

$$\phi = \arctan\left(\frac{\delta_p}{\delta_t}\right). \quad (6.6)$$

The obtained median angle of 92.2° indicates that, within our detection limit, we do not observe tangential components, a finding consistent with the non-adhesive characteristics of the PEG-NB based hydrogel (see Figure 6.4B).

In order to assess the normal forces exerted by the nucleus as determined from bead displacement experiments, supplementary AFM experiments were conducted to determine the stiffness of both the hydrogel and the cell nuclei. Two distinct compositions of the hydrogel were investigated: a stiff composition comprising 5mM PEG-NB with a crosslinker ratio of 0.8, and a soft composition comprising 3mM

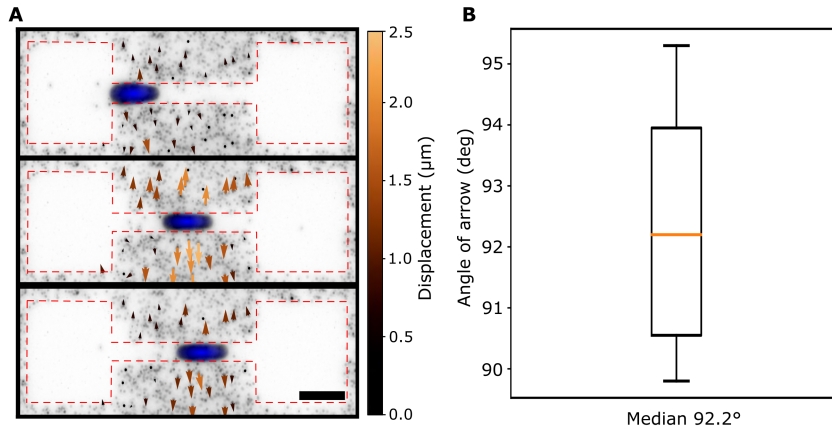


Figure 6.4: **Analysis of the bead displacement.** (A) Representative image of the fluorescently labeled nucleus of an MDA-MB-231 cell traversing the soft PEG-NB hydrogel channel. The displacement field of fluorescent beads incorporated into the hydrogel is visualized with color-coded arrows. (B) Assessment of bead displacement angles: The median displacement values along both the vertical and horizontal axes relative to the hydrogel wall surface (Box plot ($n = 500$) with whiskers extending to $\pm 1.5 \times \text{IQR}$). Figure adapted from [135].

PEG-NB with a crosslinker ratio of 0.4. The stiff composition is employed to generate hundreds of trajectories analyzed in the previous chapter, whereas the soft composition is employed to evaluate the forces exerted by the nucleus on the hydrogel. The Young's moduli for these hydrogel compositions were measured at 23 kPa across 1465 locations and 3 kPa across 1256 locations, respectively. These values are consistent with established ranges for PEG-NB hydrogels [184], emphasizing the physiological relevance of PEG-NB in mimicking various biological tissues. The median Young's modulus for the cell nuclei was determined to be 368 Pa, based on measurements taken at 1920 different positions across 20 cells. These findings are in agreement with published data for the MDA-MB-231 cell line. As illustrated in Figure 6.5, the cells under examination were observed to remain adherent to the bottom of the Petri dish during the measurement process, rather than undergoing constriction-induced deformation, indicating their migration behavior.

To assess the measured normal forces exerted by the nucleus, we adapted a classical Hertz' model to describe gel deformation, relying on the displacement of fluorescent nanobeads tracking the hydrogel deformation. The hydrogel exerts opposing force against an indenting sphere in accordance with Hertz' force, as expressed by the following equation [203, 240]:

$$f_h(\delta) = \frac{4}{3} \frac{E_h}{1 - \nu_h^2} \sqrt{R_i} \delta^{3/2} \quad (6.7)$$

In this context, δ represents the extent of indentation into the hydrogel wall, while R_i denotes the initial radius of the unsqueezed cell nucleus. E_h and ν_n stand for the Young's modulus and Poisson's ratio of the hydrogel, respectively.

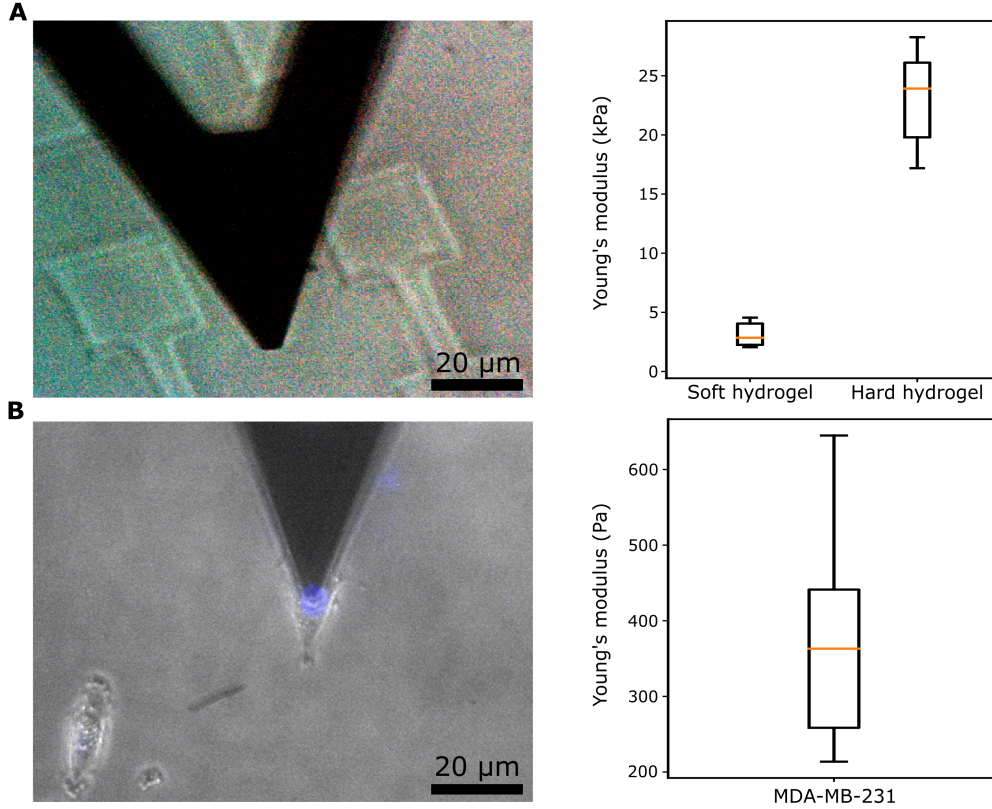


Figure 6.5: **Stiffness measurements of hydrogel and cell nuclei performed with an AFM.** (A) Evaluation of hydrogel stiffness measuring the interaction between two dumbbell structures, considering diverse compositions of the hydrogel (Box plot ($n_{\text{soft}} = 1465$; $n_{\text{hard}} = 1256$) with whiskers extending to $\pm 1.5 \times \text{IQR}$). (B) Stiffness measurement of the nuclei in MDA-MB-231 cells (Box plot ($n = 1920$) with whiskers extending to $\pm 1.5 \times \text{IQR}$). Figure adapted from [135].

Furthermore, we have developed a theoretical framework to compute the expected indentation of the hydrogel induced by a traversing cell. To this end, we employ a basic Hertz model, wherein a compliant sphere experiences compression between two compliant half-spaces (Figure 6.6). Considering the equilibrium established between the sphere and the confining material, it is reasonable to deduce that the hydrogel wall experiences a force similar to that exerted by a rigid sphere (see Figure 6.6A). Simultaneously, the nucleus is conceptualized as a sphere undergoing compression between theoretically infinitely rigid boundaries (see Figure 6.6B). In conclusion, the equation governing the force exerted by the nucleus when compressed to a length of α is as follows [240]:

$$f_n(\alpha) = \frac{4}{3} \frac{E_n}{1 - \nu_n^2} \sqrt{R} \alpha^{3/2} \quad (6.8)$$

The opposing force exerted by the hydrogel against a sphere indenting by δ , denoted as F_h is described by Eq. 6.7. In this context, R_i represents the initial radius of the cell nucleus (prior to compression), while R denotes the radius under compression.

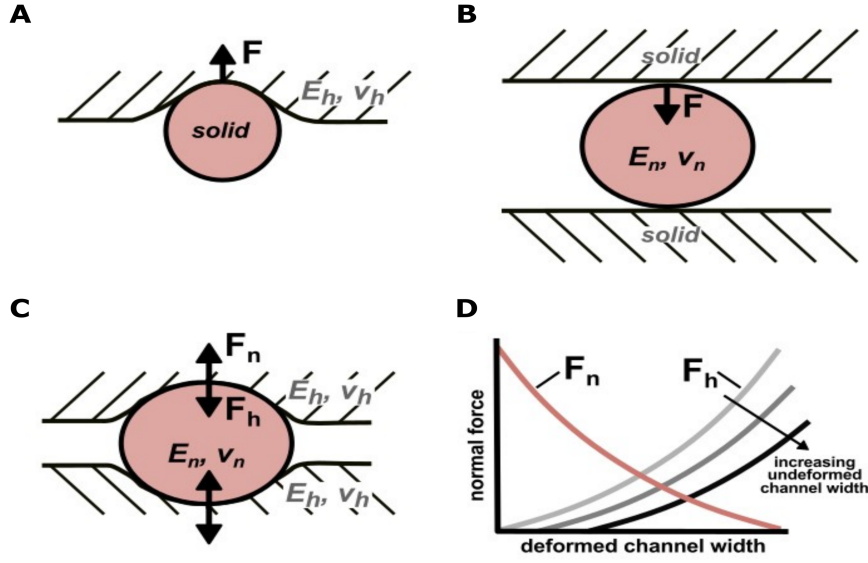


Figure 6.6: **Schematic visualization of the relevant contact mechanics setups.** (A) A rigid sphere is subjected to indentation within an elastic half-space. (B) An elastic sphere undergoes compressive deformation when confined between two rigid boundaries. (C) A deformable sphere experiences squeezing between two compliant half-spaces. (D) An illustrative depiction demonstrating the anticipated state of equilibrium between a soft sphere and a flexible half-space. Figure adapted from [135].

The equilibrium of the system, where these two forces are balanced, determines the expected displacement. To determine this equilibrium, the indentation of the hydrogel is expressed as $\delta = \left(\frac{h}{2} - \frac{h_i}{2}\right)^{3/2}$, and the length of the compressed nucleus as $\alpha = \left(R_i - \frac{h}{2}\right)^{3/2}$. By equating these two forces (Figure 6.6C and D), the following equation is derived:

$$\frac{4}{3} \frac{E_n}{1 - \nu_n^2} \sqrt{R_i} \left(R_i - \frac{h}{2}\right)^{3/2} = \frac{\left(\frac{E_n}{1 - \nu_n^2}\right)^{2/3}}{\left(\frac{E_h}{1 - \nu_h^2}\right)^{2/3} + \left(\frac{E_n}{1 - \nu_n^2}\right)^{2/3}} \left(R_i - \frac{h_i}{2}\right) \quad (6.9)$$

We consider the mechanical characteristics of both the hydrogel and nucleus. The Young's modulus and Poisson's ratio of the hydrogel are denoted as E_h and ν_h , while those of the nucleus are denoted as E_n and ν_n respectively. The initial height of the constriction, labeled as h_i , signifies the separation between the hydrogel walls in the absence of a cell. Correspondingly, the initial radius of the cell nucleus, denoted as R_i , represents its dimension when not subjected to constriction. Upon the presence of a cell within the constriction, the separation between the walls h or the diameter of the nucleus alters. In cases where the hydrogel and the nucleus possess comparable stiffness properties and the constriction width is sufficiently

narrow, a notable difference between the initial height h_i and the final height h may be observed. This difference occurs due to the displacement of the hydrogel induced by a displacement value δ . The displacement can be determined by solving the following equation.

$$\delta = \frac{h}{2} - \frac{h_i}{2} = \frac{\left(\frac{E_n}{1 - \nu_n^2}\right)^{2/3}}{\left(\frac{E_h}{1 - \nu_h^2}\right)^{2/3} + \left(\frac{E_n}{1 - \nu_n^2}\right)^{2/3}} \left(R_i - \frac{h_i}{2}\right) \quad (6.10)$$

This equation describes the anticipated deformation of the hydrogel when a cell nucleus is squeezed inside a hydrogel constriction.

Collectively, the normal forces exerted by the nucleus, as inferred from the bead

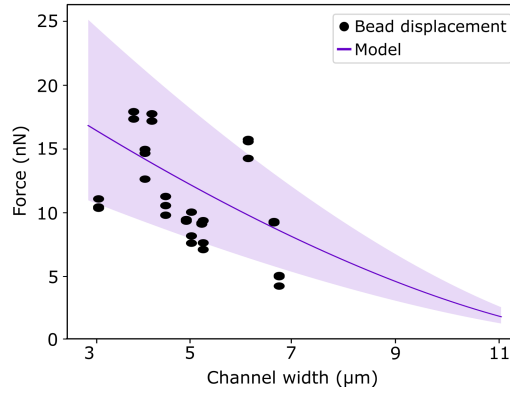


Figure 6.7: **Contact forces exerted from the nucleus to the hydrogel walls as a function of channel width.** The normal forces were evaluated as a function of channel width, derived from the observed bead displacement (shown as black dots). For comparison, the expected forces are shown in purple based on a Hertz model utilizing independently measured Young's moduli of both the hydrogel and cell nucleus (shaded area represents one standard deviation). Figure adapted from [135].

displacement experiments with the experimentally determined Young's modulus, exhibit a non-linear increase with increasing confinement (see black dots in Figure 6.7). To facilitate comparison, we anticipate the contact forces through a theoretical model based on the modified Hertz model derived from Equation 6.10. In this context, a compliant nucleus, symbolized as an elastic sphere possessing the experimentally determined Poisson's ratio ($\nu_n = 0.40$) and a Young's modulus ($E_n = 368$ Pa) (see Figure 6.3), indents a compliant wall characterized by an independently measured Young's modulus ($E_h = 3$ kPa) obtained via AFM in the absence of confinement (see purple curve in Figure 6.7). The alignment between the estimated forces exerted by the nucleus onto the hydrogel walls and the predictions of the adjusted Hertz model suggests that the elastic properties of the nucleus remain relatively unchanged during cellular transmigration through a 3D constriction.

6.4 Discussion

In this chapter, we analyze the mechanical properties of the nucleus to attain a deeper understanding of its role as a constraining factor governing cell migration. Initially, we investigated the viscoelastic characteristics of the nucleus of MDA-MB-231 cells. To accomplish this, we utilized 2D time-lapse microscopy datasets to quantify the morphological changes of nuclei during transmigration through constrictions. Our findings indicate that, within the relevant temporal scales of our investigation, the response of the nucleus is predominantly elastic. This observation aligns with the dynamics elucidated in the previous chapter, wherein no evidence of a memory effect associated with multiple transmigration of cells through constriction was observed. Nonetheless, our results imply that the width of the confinement exerts an influence on nuclear recovery, as the recovered nuclear morphologies exhibit variation contingent upon channel width. This aspect requires further investigation in subsequent studies, which may involve modifications to the experimental framework such as altering the dimensions of the dumbbell-cavities, or studies using alternative cell lines characterized by nuclei with more pronounced viscous properties.

Additionally, we explored the nuclear volume utilizing 4D confocal imaging techniques. Our findings indicate that the nuclear volume exhibits a progressive increase over time, independently of the presence of confinement, attributable to cellular growth. This observation is consistent with previous investigations concerning nuclear size [241, 242]. Across various cell sizes, the nuclear volume and cell volume correlate. Jorgensen et al. suggests a consistent increase in nuclear volume concurrent with cell volume increase, particularly during DNA replication in the S phase [241]. Similar observations of gradual nuclear enlargement during the cell cycle has been reported in HeLa cells [243]. Collectively, these findings suggest that nuclear volume is not solely determined by DNA content.

However, over shorter timescales, there is a significant reduction in nuclear volume, up to 11%, observed when cells undergo deformation while traversing narrow constrictions. These alterations in nuclear volume during confinement are of particular interest, as it has been proposed that changes in nuclear volume may occur in response to imbalances in inward and outward pressures, potentially facilitating fluid flow into or out of the nucleus through nuclear pore complexes embedded within the nuclear envelope [32, 244]. However, experimental validation of compressibility has been challenging [20]. Based on these observed volume changes, a Poisson's ratio for cell nuclei of $\nu_n = 0.40$ was determined.

Another interesting observation is the difference in slope between confined and unconfined states. The relatively flatter slope in the unconfined state suggests incomplete recovery of nuclear volume upon cell exit from the channel. Consequently, further investigations are required to determine the statistical significance of this observation, given that only one cell in our study exhibited this behavior.

Moreover, we employed the versatile PEG-NB hydrogel assay to experimentally assess the contact forces exerted by cells as they undergo deformation while traversing narrow constrictions. This approach enables us to investigate whether strong

confinement influences the elastic properties of the nucleus. Soft hydrogels were fabricated to facilitate detection of deformation in the corresponding hydrogel walls during cell transmigration through narrow channels. Additionally, fluorescent beads incorporated within the hydrogel served as means to quantify cellular forces exerted onto the hydrogel wall. Our findings suggest that, within our experimental setup, friction can be neglected due to the orientation of the bead displacement vectors. The experimentally determined normal forces exerted by the nucleus exhibit a non-linear increase with increasing confinement. Interestingly, comparison of these forces with contact forces predicted by the modified Hertz model, computed using an independently measured Young's modulus of unconfined cell nuclei, reveals a similar non-linear increase with increasing confinement. Prior investigations have indicated that certain cell lines actively modulate their nuclear stiffness under confinement [245, 246]. Thiam et al. demonstrated that dendritic cells migrating through narrow constrictions accumulate F-actin around the nucleus, leading to disruption of lamin A/C and subsequent nuclear softening [245]. However, our experimental and theoretically predicted results demonstrate a consistent trend, suggesting no evidence of nuclear mechanical adaptation effects, such as nuclear softening, within the timescale of our experimental system. Nevertheless, this area requires further investigation. For instance, utilizing cells labeled with an F-actin lifestain in conjunction with an adapted experimental setup involving elongation of the channels in the dumbbell-shaped cavities could provide valuable insights.

In summary, this chapter presents a comprehensive characterization of the mechanical properties of the cell nucleus in MDA-MB-231 cells, offering deeper insights into the cellular migration mechanisms during confined migration. The methodologies employed to obtain these mechanical properties introduce novel approaches, highlighting the versatility of the PEG-NB based dumbbell-shaped experimental assay. Particularly noteworthy is the integration of confocal microscopy to analyze changes in nuclear volume over time during multiple transmigrations through confinement, as well as the use of embedded fluorescent nanobeads to investigate potential alterations in nuclear elastic properties under conditions of strong confinement. These methodologies offer promising possibilities for adaptation and utilization in future work.

7. Adaptive Cellular Force Generation in Physical Confinement

In the previous chapter, we analyzed the mechanical properties of the cell nucleus to gain a more profound understanding of its role as a rate-limiting factor in confined migration. A fundamental aspect in this context is how cells generate sufficient forces to facilitate the translocation of their nuclei into constraining environments. Both pulling and pushing forces have been evidenced to exert substantial influence on the dynamics of confined cellular migration. Davidson et al. investigated the behavior of embryonic mouse fibroblasts traversing narrow constrictions, indicating a strong reliance on actomyosin contractile forces, generated predominantly in the front of the nucleus [19]. Subsequent laser ablation experiments, targeting the cytoskeleton in cells located within the confinement, served to validate the significance of pulling-based migration. Laser ablation anterior to the nucleus induced significant rearward cellular movement, contrasting with ablation performed at the cell's posterior, which failed to induce comparable forward retraction of the nucleus. Furthermore, laser ablation experiments conducted at the front, employing cells with disrupted LINC complexes, revealed no significant rearward movement, highlighting the role of the LINC complex in pulling-based migration. However, Thomas et al. investigated the behavior of MDA-MB-231 cells within the same experimental framework, dissecting the distinct contributions of myosin IIA and myosin IIB [33]. Interestingly, myosin IIA exhibited preferential localization anterior, whereas myosin IIB exhibited posterior localization. Notably, cells lacking myosin IIB displayed reduced migration efficiency through confinement, indicating the pivotal role of rear-generated forces in MDA-MB-231 cell migration.

Recent publications have performed a comprehensive investigation into the intricate mechanisms underlying rear contractility-driven translocation [34, 35]. Keys et al. categorized migrating cells into 'cortex-driven' and 'non-cortex-driven' migration based on cellular morphology. Cortex-driven migration entails posterior pushing forces, whereas non-cortex-driven migration relies on anterior pulling forces. Their findings revealed that MDA-MB-231 cells predominantly migrate based on the non-cortex mechanism in wide constrictions. Conversely, in narrow constrictions, the predominant migration mechanism shifts towards cortex-driven processes, indicating an adaptive modulation of dominant force generation mechanisms. Overall, these studies highlight the pivotal role of nuclear deformations in increased rear contractility. This increased cortical contractility is postulated to be facilitated by a mechanism wherein nuclear deformations trigger an elevated release of Ca^{2+} and

subsequent cortical contractility [30, 31].

In this chapter, we utilize the mechanical characterization of the nucleus to obtain deeper insights into the cellular force generation during confined migration and elucidate the impact of confinement levels therein. Here, we assess alterations in nuclear morphology relative to their natural spherical shape across a broad spectrum of confinement widths, aiming to determine whether the nucleus is primarily 'pulled' or 'pushed'. The nuclear dimensions in the two unconfined directions serve as indication for the applied forces. To challenge our interpretation of nuclear morphology, we selectively perturb this mechanism by targeting focal adhesions and the LINC-complex separately. Additionally, we quantify cytosolic calcium levels under various degrees of confinement to validate the recently proposed role of Ca^{2+} for the generation of 'pushing' forces. Lastly, we explore the concept of an adaptive force generation mechanism by developing a model for cellular force generation during confined migration. The key aspect of this model lies in the combination of two confinement-dependent force generation mechanisms: pulling forces, stemming from actomyosin contractility at the cell front, and pushing forces, modulated by cortical tension at the rear.

7.1 Nuclear Shape Analysis Indicate Pulling and Pushing Forces

To gain initial insights into the influence of external forces on the confined nucleus located in the center of the channel, we quantify the deviation from isotropic (force free) expansion of the nucleus when subjected to compression against the channel walls. Employing the previously determined Poisson ratio of the nucleus, we utilize the 2D time-lapse microscopy data to assess alterations in the $x - z$ aspect ratios (AR) as cells transition from a chamber to the channel (see Figure 7.1). In order to derive an approximate expression for the dimensions of the compressed nucleus under the influence of pulling and pushing forces along the x-direction, we initially determine the shape of the unconfined nucleus when subjected to these forces. Subsequently, we incorporate confinement-induced deformation in the y-direction along with isotropic expansion in the x and z-direction.

The combined effect of pushing and pulling forces results in a strain u_{xx} along the x-direction. Subsequently, the strains in the orthogonal directions are determined by the relationship [247]: $u_{yy} = -\nu_n u_{xx}$ and $u_{zz} = -\nu_n u_{xx}$, where ν_n is the Poisson ratio of the nucleus. For small deformations along the x-direction, the strains can be as [248]: $u_{xx} = \frac{dx}{x}$, $u_{yy} = \frac{dz}{z}$. To determine the induced deformations Δy and Δz resulting from forces acting in the x-direction, we integrate the infinitesimal strains, utilizing the relationship $u_{yy} = u_{zz} = -\nu_n u_{xx}$. This leads to the following expression:

$$\int_{y_0}^{y_0+\Delta y} \frac{dy}{y} = \int_{z_0}^{z_0+\Delta z} \frac{dz}{z} = -\nu_n \int_{x_0}^{x_0+\Delta x} \frac{dx}{x}, \quad (7.1)$$

from which we derive:

$$\frac{y_0 + \Delta y}{y_0} = \frac{z_0 + \Delta z}{z_0} = \left(\frac{x_0 + \Delta x}{x_0} \right)^{-\nu_n}. \quad (7.2)$$

Expressing the deformation of the nucleus induced by the combined pulling and

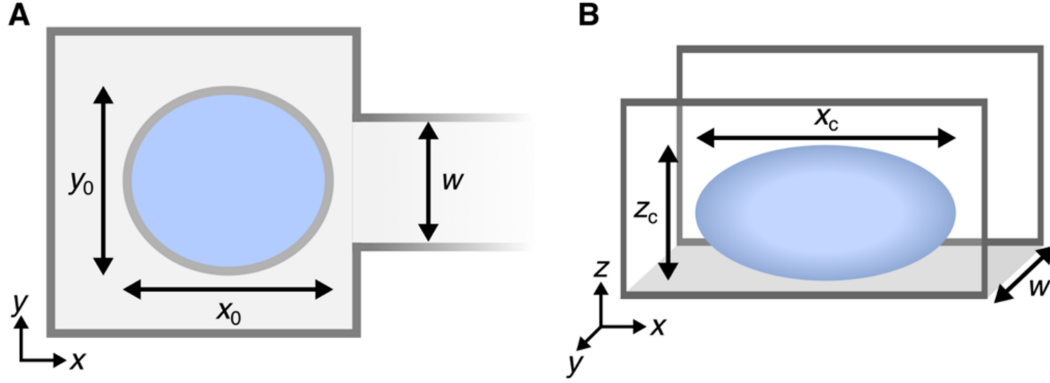


Figure 7.1: **Illustration of the nuclear dimensions** (A) Nuclear dimensions on the island and (B) in the channel. Figure adapted from [135].

pushing forces along the x -direction as Δx_{forces} , resulting in the new length of the nucleus $x_{forces} = x_0 + \Delta x_{forces}$. We can utilize Eq. (7.2) to express the corresponding nuclear dimensions in the perpendicular directions:

$$y_{forces} = y_0 + \Delta y_{forces} = y_0 \left(1 + \frac{\Delta x_{forces}}{x_0} \right)^{-\nu_n} \quad (7.3)$$

and

$$z_{forces} = z_0 + \Delta z_{forces} = z_0 \left(1 + \frac{\Delta x_{forces}}{x_0} \right)^{-\nu_n}, \quad (7.4)$$

where $x_0/y_0/z_0$ represent the force-free width of the nucleus in the $x/y/z$ -direction, respectively. We now introduce the confinement effect imposed by the channel of width w , such that the width of the nucleus within the channel becomes $y_c = w$. Consequently, the diameter of the nucleus in the other dimensions is determined as follows:

$$x_c = x_{forces} \left(\frac{w}{y_{forces}} \right)^{-\nu_n} \quad (7.5)$$

and

$$z_c = z_{forces} \left(\frac{w}{y_{forces}} \right)^{-\nu_n}. \quad (7.6)$$

The aspect ratio between the two unconfined dimensions of the nucleus within the channel can be expressed as:

$$AR_{confined} = \frac{x_c}{z_c} = \frac{x_0}{z_0} \left(\frac{x_{forces}}{x_0} \right)^{1+\nu_n}. \quad (7.7)$$

In cases where the pulling force dominates over the pushing force, we expect $\Delta x_{\text{forces}} > 0$ and thus $AR_{\text{confined}} > x_0/z_0 = AR_{\text{free}}$. Conversely, if pushing forces prevail over pulling forces, we expect $\Delta x_{\text{forces}} < 0$ and hence $AR_{\text{confined}} < AR_{\text{free}}$. Accordingly, we introduce the shape parameter ϵ defined as:

$$\epsilon = \frac{AR_{\text{confined}}}{AR_{\text{free}}} = \left(\frac{x_{\text{forces}}}{x_0} \right)^{1+\nu_n} \quad (7.8)$$

When $\epsilon > 0$, pulling emerges as the predominant force governing nucleus translocation, while for $\epsilon < 0$, pushing dominates. Nevertheless, direct experimental access to x_{forces} remains unavailable. To represent ϵ in terms of measurable quantities, we utilize the relations $x_{\text{forces}} = x_c \left(\frac{w}{y_{\text{forces}}} \right)^{\nu_n}$ and $y_{\text{forces}} = y_0 \left(\frac{x_{\text{forces}}}{x_0} \right)^{-\nu_n}$, yielding:

$$\frac{x_{\text{forces}}}{x_0} = \left[\frac{x_c}{x_0} \left(\frac{w}{y_0} \right)^{\nu_n} \right]^{\frac{1}{1-\nu_n^2}} \quad (7.9)$$

and consequently:

$$\epsilon = \left[\frac{x_c}{x_0} \left(\frac{w}{y_0} \right)^{\nu_n} \right]^{\frac{1+\nu_n^2}{1-\nu_n^2}} \quad (7.10)$$

Using Eq. (7.10), we characterize the observed nuclear deformations experimen-

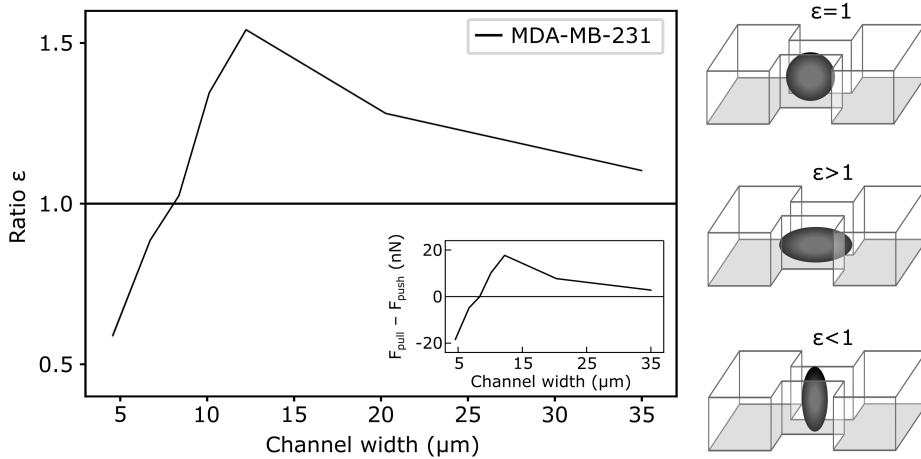


Figure 7.2: **Nuclear shape analysis.** The alteration in the nuclear aspect ratio indicates either elongation ($\epsilon > 1$) or compression ($\epsilon < 1$) of the nuclear shape along the migration direction, aligning with the prevailing mechanism of either pulling or pushing-dominated translocation, respectively. Figure adapted from [135].

tally (see Figure 7.2). Values exceeding 1 indicate that under confinement, the nucleus undergoes stretching along the migration direction, resulting in a more elongated morphology than anticipated for isotropic expansion under lateral compression. Conversely, values below 1 indicate compression of the nucleus in the migration direction, yielding a less elongated morphology compared to isotropic expansion. In

instances where nuclear deformations are absent ($w \geq 12 \mu\text{m}$), ϵ initially increases with increasing confinement width, reaching a maximum of 1.4 at a channel width of $12 \mu\text{m}$. However, upon entering a regime where confinement induces notable nuclear deformations ($w < 12 \mu\text{m}$), ϵ begins to decrease, eventually dropping below 1 for channel widths less than $7 \mu\text{m}$, reaching a value of 0.5 at a confinement width of $4 \mu\text{m}$. Consequently, wild-type MDA-MB-231 cells exhibit a non-monotonic dependence of the shape parameter ϵ on channel width, indicative of varying forces acting on the nucleus with varying levels of confinement.

Based on our characterisation of the mechanical properties of the nucleus under confinement, we establish a correlation between variations in nuclear deformations and alterations in the applied forces. We assume two primary components contributing to these forces: a pulling force F_{pull} generated in front of the nucleus and a pushing force F_{push} acting from its rear. Collectively, these forces yield a total deformation force ($F_{\text{deform}} = (F_{\text{pull}} - F_{\text{push}})/2$) exerted on the nucleus in the direction of migration (see Figure 7.2 inset). Further insights into the estimation of nuclear deformation forces from experimentally observed nuclear shapes can be found in [135].

In scenarios where pulling forces predominate, a positive deformation force in the migration direction leading to an elongated nucleus ($\epsilon > 1$). Conversely, a dominant contribution from pushing forces yields a negative deformation force, leading to nucleus compression ($\epsilon < 1$) (see Figure 7.2 inset). Therefore, our mechanical model of the nucleus suggests that the shift in the nuclear deformation behavior with varying channel widths can be interpreted as a transition from a migration regime primarily driven by pulling forces in wider channels to one dominated by pushing forces in channels narrower than $7 \mu\text{m}$.

7.2 Perturbation of Pulling Force Generation

In order to generate pulling forces, cells rely on the transmission of forces between focal adhesions located at the cell's leading edge and the nucleus via actin fibers [20]. To challenge our interpretation of nuclear shape, we aim to selectively disrupt this mechanism by targeting focal adhesions and the linkage between the cytoskeleton and the nucleus separately. We expect that such interventions will result in reduced pulling forces, thereby reflecting as reduced values of ϵ . To validate this reduction in cell adhesion, we conducted experiments involving the transfection of MDA-MB-231 cells with GFP-labeled paxillin (see Appendix A for further experimental details). Subsequently, these cells were seeded onto both fibronectin-coated and uncoated dumbbell structures, followed by examination using confocal microscopy. Despite the adhesive properties of the underlying COC-substrate of the microscopy slide, cells are still able to migrate and adhere along the bottom of the dumbbell cavities.

The depletion of fibronectin experiments revealed that in both cases, cells about to transmigrate through the channel and located in the chamber, show pronounced focal adhesions in the case of fibronectin-coated dumbbell-structures whereas cells adhered to the uncoated substrate lack focal adhesions (see Figure 7.3A). Moreover, we specifically targeted the LINC complex, comprising nesprin, SUN, and

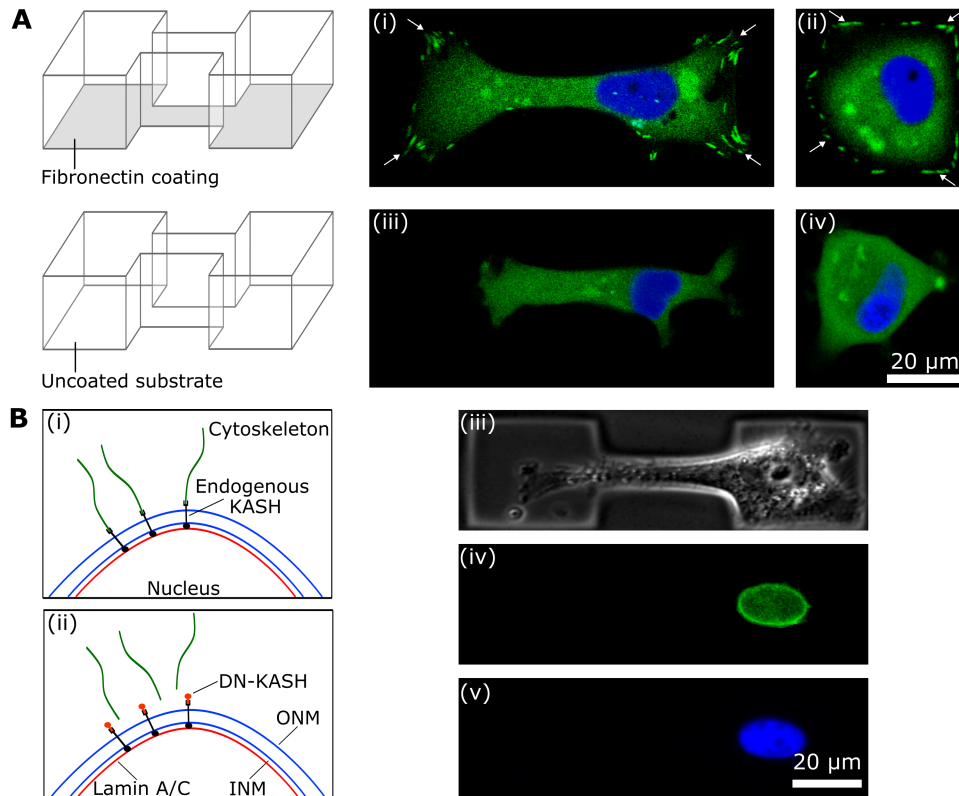


Figure 7.3: **Inhibition of pulling forces.** (A) Representative images depict paxillin-GFP transfected MDA-MB-231 cells adhered onto substrate with fibronectin coating ((i) and (ii)) and without fibronectin coating ((iii) and (iv)). In the presence of fibronectin, paxillin is integrated into focal adhesion complexes, as indicated by white arrows. (B) Illustration of the linkage between the cytoskeleton and nucleus following cell transfection with DN-KASH. Representative images show a transfected MDA-MB-231 cells expressing GFP-labeled DN-KASH and mCherry H2B (iii) - (v). Figure adapted from [135].

lamin proteins (see section 2.3 for further details). A pivotal role of the LINC complex is to tether the nucleus to the actin, microtubule, and intermediate filament cytoskeleton, thereby facilitating force transmission between the nucleus and the cytoskeleton [249]. To disrupt the mechanical linkage between actin fibers and the nucleus, we transfected MDA-MB-231 cells with GFP-labeled dominant negative KASH (DN-KASH), a dominant negative protein that displaces endogenous nesprins from the nuclear envelope, thereby disrupting nuclear-cytoskeletal connections (see Figure 7.3B). The overexpression of DN-KASH disrupts the LINC complex by saturating available binding sites at the nuclear envelope. The efficacy of the transfected cells was assessed by evaluating the GFP fluorescence signal accumulated at the nuclear envelope (see Figure 7.3B(iv)).

To investigate the impact of interfering with pulling force generation, we conducted further time-lapse microscopy experiments to obtain large amounts of data for analyzing ϵ values by either using uncoated-dumbbell structures or DN-KASH trans-

fectured cells. Additionally, we assessed the effects on transition rates and nuclear velocity within the center of the constriction. Both types of experiments were conducted across the entire range of constriction widths (see Figure 7.4).

The transition rates observed in DN-KASH transfected cells and experiments con-

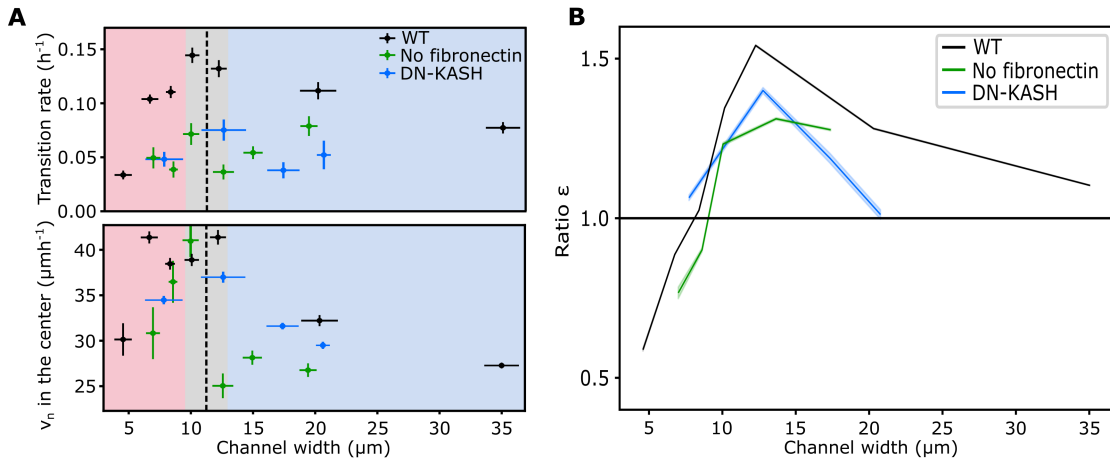


Figure 7.4: Effect of pulling inhibition on cell dynamics and nuclear shapes. (A) Transition rates with reduced pulling forces. In both scenarios, wherein fibronectin is absent (green) and the mechanical coupling between the cytoskeleton and nucleus is disrupted (blue), cellular transition rates decrease compared to wild-type cells adhered to fibronectin-coated substrates (black). Lower panel: nuclear velocities under conditions of reduced pulling forces. Within the pushing-dominated regime, nuclear velocities show small alteration in response to the absence of focal adhesions (green) or transfection with DN-KASH (blue). (B) Relative changes in nuclear aspect ratios. Selectively interfering with cellular pulling forces results in reduced ϵ values, particularly evident at wider channel widths. Figure adapted from [135].

ducted on substrates lacking fibronectin coating exhibit significant reduction across the entire range of constriction widths. This observation is particularly interesting, as the inhibition of pulling forces also impacts cellular transmigration within the pushing-dominated regime. Interestingly, nuclear velocity appears to remain unaffected throughout the entire range of confinement. Although cells transfected with DN-KASH exhibit a slight reduction in nuclear velocity across all channel widths, cells migrating on uncoated substrates experience more pronounced reductions in the pulling-dominated regime, with comparatively lesser effects in the pushing-dominated regime.

Consistent with our expectation, both approaches aimed at disrupting pulling force generation resulting in a less elongated nuclear morphology, reflected in lower ϵ values. Specifically, in the pulling-dominated regime, ϵ values are significantly lower compared to wildtype MDA-MB-231 cells, whereas for constriction widths approximately equal to or less than the nuclear diameter, ϵ values appear to be similar.

7.3 Quantification of the Cytosolic Calcium Levels

Inhibition of pulling forces reduces transition across the entire spectrum of channel widths, even within the pushing dominated regime. This observations suggests that, for cells to generate significant pushing forces, they must initially pull their nucleus into the constriction, thereby inducing deformation. Subsequently, Keys et al. demonstrated that pronounced nuclear deformation lead to the accumulation of myosin II at the rear cortex. In contrast, in cells migrating through larger control channels, myosin II localization was primarily observed at the front of the cell body or the leading edge of the nucleus [34]. This accumulation of myosin II triggers increased cortical tension, resulting in an osmotic pushing force that drives the nucleus through the channel. Recent investigations have highlighted the crucial role of calcium ions as a hallmark of this mechanism, as increased levels of Ca^{2+} are released from the nuclear envelope upon complete unfolding induced by nuclear deformation (see Section 2.2.3 for further details) [30,31]. To validate this mechanism within our experimental system, we quantified cytosolic calcium levels across varying degrees of confinement.

Hence, we employed the calcium indicator Calbryte520 AM, which was previously utilized by Venturini et al. to investigate calcium levels in relation to unfolding of the nuclear membrane [31]. Upon entry into the cell, Calbryte520 AM undergoes hydrolysis by intracellular esterases, leading to its activation and responsiveness to calcium. Subsequently, the activated indicator transforms into a polar molecule incapable of freely diffusing through the cell membrane, effectively sequestering it within the cell. Upon binding calcium ions, Calbryte520 AM generates a bright fluorescence signal characterized by a high signal-to-background ratio. These experiments involved fabricating dumbbell-shaped cavities within varying degrees of confinement. Cells were seeded onto these structures and allowed to adhere before the addition of Calbryte520 AM. To assess cellular calcium levels, the calcium signal was integrated across the entire cytosol (see Figure 7.5A), and the mean intensity per pixel was determined. Remarkably, under conditions of strong nuclear confinement, we observed significantly increased calcium levels compared to cells migrating through wider channels. Conversely, regardless of channel width, cells located within the chamber exhibited reduced calcium levels. This implies that calcium levels undergo a transient increase only during nuclear deformation while traversing the constriction. Overall, these findings support the release of calcium from the nuclear envelope upon complete unfolding induced by nuclear deformation.

7.4 Modification of Actomyosin Contractility

Given that both pulling and pushing forces are contingent upon actomyosin contractility, we explore how the balance between these forces is modulated by actomyosin contractility. To this end, we employ specific drugs to interfere with contractility. First, we utilize the drug Y-27632, a selective inhibitor of Rho-associated protein

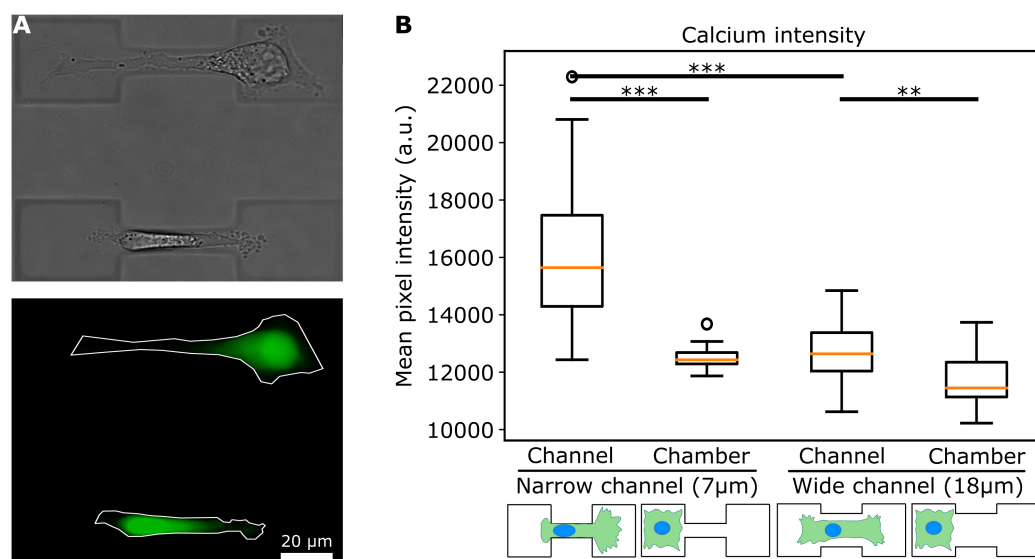


Figure 7.5: **Cytosolic calcium levels at different degrees of confinement.** (A) MDA-MB-231 cells with added Calbryte520 AM positioned within the dumbbell-shaped cavities. Outlines of the cells indicate the integrated cytosol. (B) The mean calcium intensity exhibits a significant increase in cells located within narrow constrictions (1st column) compared to those in the chamber (2nd and 4th column) and in wide constrictions (3rd column). Statistical analysis was performed using a box plot (with $n_1 = 20$; $n_2 = 20$; $n_3 = 30$; $n_4 = 20$ from two biological replicates for each condition), with whiskers extending to $\pm 1.5 \times \text{IQR}$. Statistical significance was determined using the Mann-Whitney-U test, with $***P < 0.001$ and $**P < 0.01$. Figure adapted from [135].

kinase (ROCK). ROCK serves as a pivotal regulator of the actin cytoskeleton and cellular contractility. By impeding its activity, Y-27632 disrupts downstream signaling cascades implicated in the organization of the actin cytoskeleton, thereby reducing cellular contractility [250, 251].

Furthermore, the inhibition of ROCK directly impedes downstream signaling and activation of RhoA [252]. The effects of this inhibitor are directly visible in the altered cellular morphology, characterized by the formation of thin and weak protrusions (see Figure 7.6A, top). Second, we employ Calyculin A, a selective activator of contractility. Cellular myosin homeostasis is achieved by the balance between phosphorylation-mediated activation and dephosphorylation-induced inactivation, with the latter predominantly mediated by myosin light chain phosphatase (MLCPase), likely targeted to its site by other regulatory proteins [253–255]. Calyculin A, derived from the marine sponge *Discodermia calyc*, functions as an inhibitor of serine/threonine phosphatases 1 and 2A, effectively blocking MLCPase activity [256]. Consequently, inhibition of MLCPase leads to sustained myosin activation and increased phosphorylation levels [257]. Calyculin A exerts diverse effects on non-muscle cells, predominantly attributable to its impact on myosin [258]. Thus, Calyculin A activates actomyosin contractility, thereby promoting robust and per-

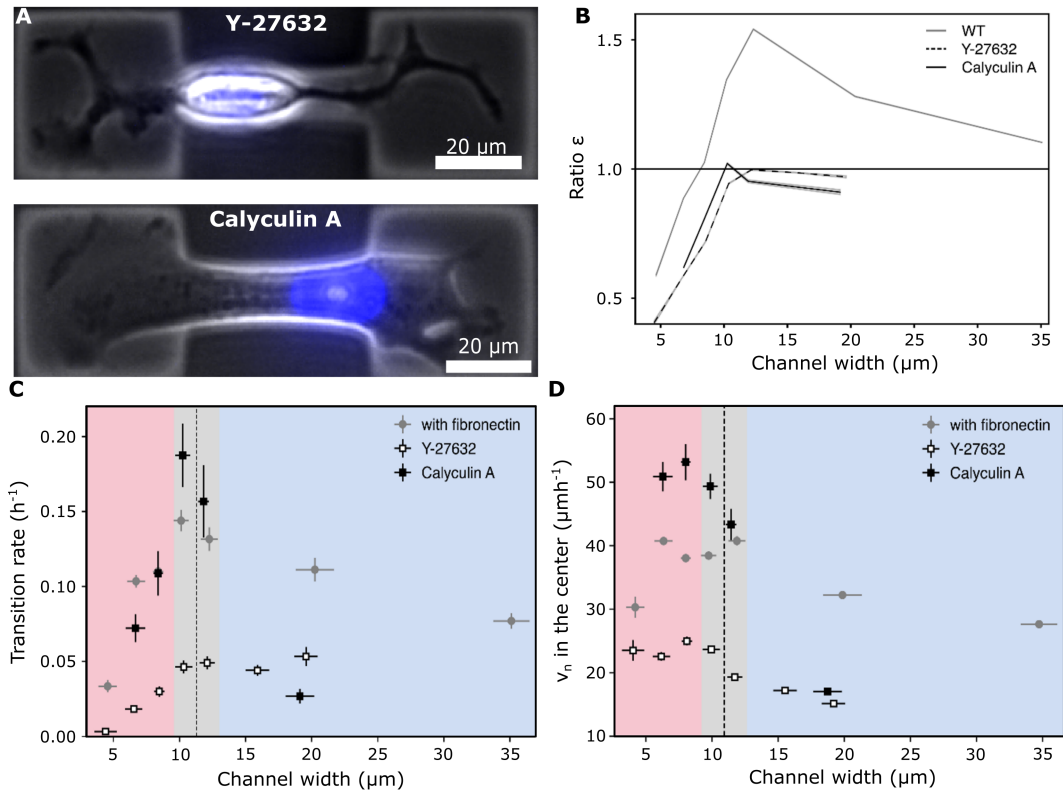


Figure 7.6: **Effect of increased and decreased actomyosin contractility.** (A) Cellular morphologies of Y-27632 and Calyculin A treated MDA-MB-231 cells. (B) Both treatments shift the relationship between pulling and pushing forces, favouring pushing forces compared to wildtype cells. (C) Transition rates observed in MDA-MB-231 cells treated with Y-27632 and Calyculin A, as well as in wild-type cells. (D) Nuclear velocities at the center of the channel in MDA-MB-231 cells treated with Y-27632 and Calyculin A, alongside wild-type cells. Figure adapted from [135].

sistent cellular protrusions (see Figure 7.6A, bottom).

These drugs were added to the cells prior to the start of time-lapse imaging and were maintained throughout the entire duration of the experiments (see appendix A for further experimental details). Our analysis indicates that in both Y-27632 and Calyculin A-treated cells, the balance between pulling and pushing forces shifts towards favoring pushing forces relative to wildtype cells across the entire spectrum of confinement widths (see Figure 7.6B). These contradictory findings are difficult to interpret, as both up- and down-regulation of actomyosin contractility appear to promote pushing forces. To further validate the impact of these drugs on the cell transmigration through the constriction, we assessed transition rates and nuclear velocities across the entire range of confinement widths (see Figure 7.6C and D). Irrespective of treatment conditions, cells exhibit a similar biphasic dependence on channel width. Treatment with Y-27632 leads to an overall reduction in transition rates compared to untreated cells. Nuclear velocities at the center of the channel follow a similar trend as the transition rates. However, mechanistic interpretation

of these results in terms of the interplay between pulling and pushing forces remains challenging due to the multifaceted effects of these drugs on cellular physiology.

7.5 Mechanistic Model for the Adaptation of Cellular Forces

We investigate the concept of an adaptive force generation by developing a model for cellular force generation during confined migration. A pivotal aspect of this model involves the integration of two confinement-responsive force generation mechanisms: pulling forces, originating from actomyosin contractility at the cells's leading edge, and pushing forces, governed by cortical tension at the rear (see section 2.3 for details). We incorporate these mechanisms by extending a simplified dynamical model, previously used to describe mesenchymal cell migration on 2D substrates [116], to three dimensions (see section 2.2 for details) and accounting for nuclear deformations under confinement. Our model comprises three degrees of freedom: the position of the nucleus, the location of the cell's leading protrusion, and a polarization parameter (see Figure 7.7A). The nucleus and protrusion are coupled via an elastic spring with stiffness k .

We absorb the friction coefficients associated with both the nucleus and the protrusion into the respective spring constants, denoting the adjusted spring constants as k_n and k_p , correspondingly. Previous studies have demonstrated that confinement of the protrusion can enhance its growth [116, 117], a phenomenon we represent by incorporating positive self-regulation on polarization under strong confinement (see Figure 7.7A)(i)). Motivated by our experimental results presented in Figure 7.5 and recent research indicating that nuclear deformations can induce an increase in cortical tension via calcium ion release [30, 31], we incorporate an augmentation in pushing forces in response to nuclear deformation (see Figure 7.7A(ii)). Furthermore, we address the confinement of the nucleus by enhancing the effective nuclear drag coefficient γ_n as the channel width decreases (see Figure 7.7A(iii)). Lastly, we model the impact of elastic nuclear deformations by introducing a progressively increasing elastic energy barrier with increasing nuclear confinement (see Figure 7.7A(iv)).

To allow a comparison to our experimental analysis of the nuclear shapes, we use our mechanical model for nuclear deformations to relate the pulling forces, exerted by the protrusion onto the nucleus, and the pushing forces in our model to nuclear deformation. In order to constrain the parameters of our mechanistic model, we simultaneously fit our model to several key experimental metrics: the deformation force acting in the migration direction, the nuclear velocity in the center of the pattern, and the transition rate. Our model offers a conceptual framework for interpreting the biphasic dependence on channel width observed in both nuclear deformations and migration dynamics. In the regime where channel widths exceed the size of the nucleus (CEM-regime), stronger confinement leads to amplified polarization and subsequent protrusion growth. Consequently, this results in a greater force pulling on the nucleus from the front, resulting in elevated nuclear velocities and transition rates. Conversely, in the regime where channel widths drop below the nuclear

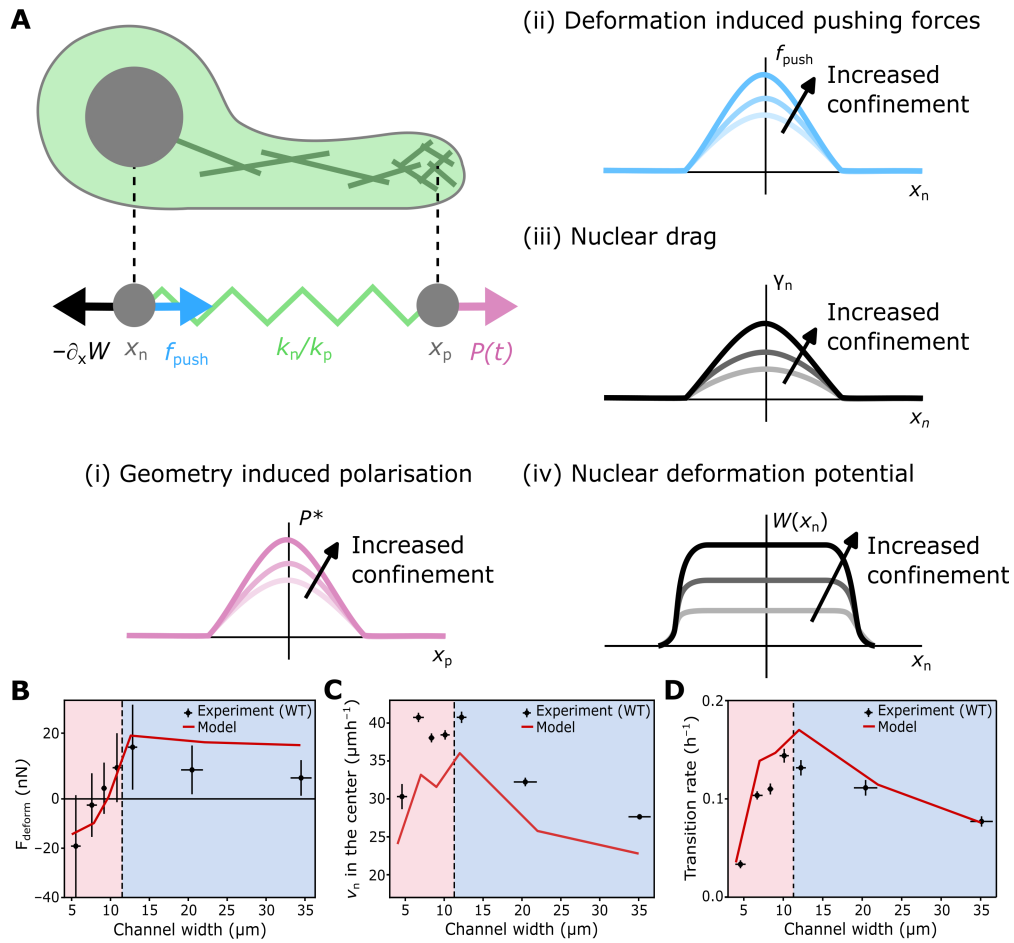


Figure 7.7: Mechanistic model for the adaptation of cellular forces to the degree of confinement. (A) Schematic representation of a simplified mechanistic model depicting mesenchymal cell migration. The protrusion and nucleus are interconnected via elastic coupling. (i) Protrusion growth is driven by a polarization force, reflecting the internal organization of the cell, which intensifies under confinement. (ii) Furthermore, deformation of the nucleus enables the cell to exert a pushing force directly on the nucleus itself. (iii) During passage through the channel, the nucleus encounters a resistance force that escalates with decreasing channel width. (iv) Confinement-induced deformations lead to a force that pushes the nucleus out of the channel. (B) - (D) Calibration of the mechanistic model to pivotal experimental findings. Error bars: (B) Indicate one standard deviation. Error bars in (C) and (D) associated with the y-axis denote the standard error, while those associated with the channel width signify the standard deviation. Figure adapted from [135].

width (CRM-regime), increased pushing forces from the cell's rear yield a decreased $F_{pull} - F_{push}$, eventually reaching negative values. Despite the increased polarization and additional pushing force, amplified nuclear friction leads to a reduction in predicted nuclear velocity within the channel. Additionally, the increasing elastic energy barrier associated with nuclear deformations impedes nucleus movement into

the channel, leading to a decline in transition rates (further information is shown in [135]). To evaluate the predictive power of our model, subsequent to constrain-

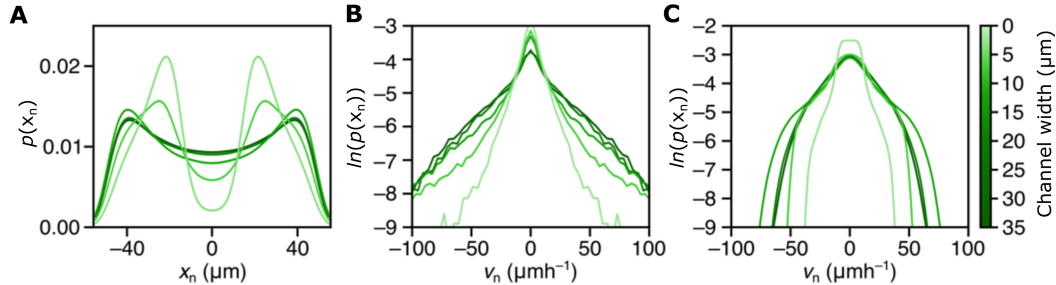


Figure 7.8: **Comparison of cell dynamics between simulation and experiment.** (A) Probability distribution of the nuclear position at varying channel widths predicted from the mechanistic model (B), (C) Probability distributions of the nuclear velocities at varying channel widths obtained experimentally (B) and via simulations (C). Figure adapted from [135].

ing all parameters, we compute the probability distributions of nuclear position in our simulations across various channel widths. The probability distribution of nuclear position shifts from a wide distribution at wider channel widths to a distinctly double-peaked distribution in narrower channels, aligning semi-quantitatively with our experimental findings (see Figure 5.4B and Figure 7.8A). In both, experiments and simulations, nuclear velocity distributions peak at zero, independent of channel width, yet exhibit reduced spread with decreasing channel width (see Figure 7.8B and C). Moreover, our mechanistic model facilitates the linkage of features in the NCMs to underlying cellular mechanisms (see section 5.3). To demonstrate this, we analyze the effective underdamped nuclear dynamics of our model (see [135] for detailed information). Mirroring the dynamics inferred from experiments, we observe deterministic flow from one chamber to another, characterized by marked acceleration within the channel. Additionally, our model successfully predicts the majority of key features observed in NCMs. At the channel entrance, the elastic barrier associated with nuclear deformations generates a region of $\Delta F_w < 0$, succeeded by a distinct region of $\Delta F_w > 0$ linked to the recoil of contractile actomyosin structures in the protrusion and supplementary pushing forces acting on the nucleus. Subsequently, as the cell exits the channel, we note a deceleration region ($\Delta F_w < 0$) as the nucleus catches up with the protrusion. In summary, our mechanistic model illustrates that cells transition from a pulling-dominated to pushing-dominated migration to generate sufficient deformation forces under confinement. This model not only explains the observed nuclear deformations but also provides a mechanistic interpretation of effective cellular dynamics inferred from experimental data.

7.6 Discussion

In this chapter, we utilized the mechanical characterization of the nucleus from the previous chapter to obtain deeper insights into cellular force generation dur-

ing repeated self-imposed migration of single cells through compliant 3D channels. Through this analysis, we examined nuclear deformation across various levels of confinement, offering a quantitative assessment of the balance between pulling and pushing forces, both of which have been qualitatively recognized as pivotal in confined cell migration [19, 26, 33, 34]. Our results suggest an adaptation of cellular force generation in response to confinement. Consequently, our mechanical nucleus model suggests that the alterations in nuclear deformation behavior with varying channel widths signify a transition from a regime dominated by pulling forces at wider channel widths to one dominated by pushing forces at widths below 7 μm .

To challenge our mechanical nucleus model, we disrupted the pulling force mechanisms in cells by depleting focal adhesions or disrupting the LINC complex, thereby saturating available binding sites at the nuclear envelope. As expected, both interventions led to less elongated nuclear shapes in the pulling-dominated regime, consistent with prior laser ablation experiments [19]. Interestingly, these experiments with reduced pulling forces also revealed a decrease in transition rates in the pushing-dominated regime. However, once the nucleus traverses into the channel, its movement appears relatively independent of the strength of the pulling force, consistent with previous findings in the context of 3D confined cell migration [34]. Furthermore, we conducted experiments to validate another mechanism involved in this adaptation of force generation, which is the increase in cytosolic calcium levels, which leads to an up-regulation of cortical contractility in response to externally induced nuclear confinement [30, 31]. Our results demonstrate transiently increased calcium levels for strongly deformed cell nuclei.

Furthermore, we manipulated the actomyosin contractility of MDA-MB-231 cells utilizing inhibitors and enhancers of contractility, respectively. In contrast to findings reported in a recent preprint by Keys et al., where inhibition of actomyosin contractility favored pulling forces and enhancement favored pushing forces, our results indicate that pushing forces are favored in both cases [34]. We validated the behavior of these drugs, Y-27632 and Calyculin A, by examining transition rates and nuclear velocities, revealing distinct up- and down-regulation of cellular dynamics. However, the observed reduction in the nuclear shape parameter, ϵ , for both drugs only signifies a relative alteration in the balance between pulling and pushing forces, which could originate from a decrease in pulling forces or an increase in pushing forces. Given that both forces are likely affected by the drugs under consideration, formulating expectations for their effects on nuclear shapes is challenging. Additionally, it remains unclear whether these drugs might have other side effects that could impact the calculated ϵ values, such as altering the nuclear Poisson ratio. Thus, further experiments, such as mechanical characterization of the nucleus as conducted in the previous chapter for wildtype MDA-MB-231 cells, would be necessary to gain a deeper understanding of the used drug effects.

Based on these experimental insights, we extended the mechanistic model for mesenchymal cell migration proposed by Flommersfeld et al. by incorporating adaptive modulation of forces in response to 3D confinement [117]. The increase in pushing forces within confinement, along with elastic deformation of the nucleus and

increased effective friction in the channel, explains both the observed nuclear deformations and the overall migration dynamics of the cells across a wide range of channel widths. Overall, our findings contribute to a more comprehensive mechanistic understanding of the complex interplay among confinement, the nucleus, and the cytoskeleton during mesenchymal cell migration. This work suggests that the force-generating cytoskeleton adapts by transitioning from pulling to pushing forces to overcome constrictions. However, one limitation of our study is the focus on a single cell line. Future research could explore additional cell lines with diverse mechanical properties to enhance the generality of our work. For instance, increased nuclear plasticity could lead to memory effects, altering cellular dynamics or force generation.

8. Conclusion and Outlook

In this presented work, we employed photo-lithographic microfabrication to produce artificial experimental assays utilizing synthetic PEG-NB hydrogels. These assays were designed to investigate cellular migration behavior and nuclear mechanics within precisely defined 3D confinement. The synthetic hydrogel's modular design facilitates the polymerization of synthetic cell environments, allowing for the replication of a wide spectrum of native ECMs, ranging from relatively soft brain tissue (0.1-1.0 kPa) [259] to stiffness levels similar to muscle tissue (8-17 kPa) [260]. Furthermore, the hydrogel can be customized through the integration of small peptide sequences, promoting cell-hydrogel interactions in an otherwise inert matrix. These adjustable properties make the hydrogel a valuable tool for generating extensive datasets of cell trajectories, facilitating quantitative analyses of cellular behavior under controlled and standardized conditions. Moreover, it serves as an appropriate experimental platform for investigating nuclear mechanics, such as nuclear stiffness, as cells navigate through compliant hydrogel channels. This is achieved through the incorporation of tracer beads within the hydrogel, which function as force sensors.

To investigate the invasive behavior of cancer cells, we fabricated micro-structured clefts utilizing PEG-NB hydrogels. These hydrogel structures, termed as 'sponge clamp', are pressurized against each other and thus, forming compliant channels for cell invasion. This experimental setup enables real-time imaging of the invasion process and provides data on cell trajectories and velocities through image analysis. Notably, this approach offers advantages over conventional invasion assays like the Boyden chamber, which simply quantifies the total number of transmigrated cells over a certain period of time. Our findings indicate distinct differences in migration velocity among cell lines MDA-MB-231 and HT-1080 depending upon constriction width and hydrogel stiffness. We hypothesize that MDA-MB-231 cells are particularly responsive to variations in ECM stiffness compared to HT-1080 cells.

To gain further insights into the invasion behavior of specific cell lines, future investigations could focus on quantifying hydrogel stiffness after the anisotropical swelling within the channels. While the previously assessed hydrogel mechanical properties using bulk measurements with a plate-plate rheometer, subsequent studies could employ passive micro-rheology. This approach could provide more precise stiffness measurements within the channels, elucidating invasion dependency on surrounding hydrogel stiffness. Besides the mechanical properties of the hydrogel, the 'sponge clamp' assay can also be adapted to other scientific questions by

changing the ligands presented in the hydrogel composition. By including different ligands, such as E-cadherins instead of integrin-targeting adhesive peptides, the assay could simulate the endothelial barrier of blood vessels, enabling analysis of cancer cell intravasation. This approach promises insights into a crucial aspect of cancer metastasis.

In order to study repeated, self-imposed 3D confined cell migration, we introduced a novel experimental assay distinct from the 'sponge clamp', which is restricted to study repeated migration due to the applied chemotactic gradient. This setup, adapted from the two-state system proposed by Brückner et al. [23], facilitates the exploration of 3D confined cell migration. The assay comprises 3D dumbbell-shaped cavities embedded within a 20 μm thick layer of PEG-NB hydrogel, enabling high-throughput cell migration experiments under controllable geometric conditions. Our findings reveal a bi-phasic behavior of the cell dynamics to varying degrees of confinement. In wide channels, both transition rates and nuclear velocities increase with confinement, whereas migration under sub-nucleus confinement is impeded. The complex impact of required nuclear deformations in narrow channels manifests in varied cell dynamics, evidenced by deceleration during the entry phase, as observed in acceleration maps inferred from nonlinear migration dynamics analysis across varying channel widths.

While these results offer valuable insights into 3D confined cell migration, the experimental platform offers diverse applications for future work. For instance, functionalizing the surrounding hydrogel with ligands could enable cell adhesion and thus, mimicking more physiological conditions. Another potential adaptation involves pre-polymerizing a thin hydrogel layer with cell-adhesive ligands onto the substrate. This would ensure consistent conditions for cells in all three dimensions and enable traction force analysis via embedding fluorescent nanobeads into the underlying hydrogel layer. Moreover, modifying properties of the dumbbell-shaped cavities, such as dimensions or mechanical characteristics, holds promise. This is particularly relevant in elucidating migration mode alterations in response to constriction width and matrix stiffness, as demonstrated in previous research [261]. This could be of particular interest in combination with the underlying experimental platform allowing for high-throughput data collection.

To obtain a deeper understanding of the role of the nucleus as a rate-limiting factor in confined cell migration, we examined the mechanical properties of the nucleus within the dumbbell-shaped cavities. Our investigation reveals a predominantly elastic response of the nucleus, with no observed memory effect from repeated cell transmigration. Additionally, we assessed nuclear volume changes during transmigration using 4D confocal imaging, observing transient reductions in volume during complete nucleus deformation within narrow constrictions. Our analysis yielded a Poisson's ratio of the nucleus of $\nu_n = 0.40$. Generalizing this finding, analyzing further cell lines could elucidate variations in nucleus compressibility. This would prompt further examination of chromatin and A-type lamin organization, key determinants of nuclear mechanical properties. Furthermore, we employed the experimental versatility to assess the forces exerted by the nucleus on compliant hydrogel walls by analyzing displacement fields of embedded fluorescent beads.

Our results suggest a non-linear increase in nuclear deformation with increasing confinement, consistent with prediction from a modified Hertz model assuming a Young's modulus for unconfined cell nuclei. The comparison of experimental and theoretical results indicate no significant adaptation of nuclear mechanical properties under confinement. Interestingly, these findings diverge from previous work, where strongly confined dendritic cells exhibited F-actin accumulation around the nucleus, resulting in lamin A/C disruption and subsequent nuclear softening [245]. This discrepancy requires further investigation to validate whether it stems from differences in cell lines or necessitates adjustments to our experimental setup. One potential strategy to challenge our experimental approach could involve analyzing bead displacement in the same dendritic cell line and applying the same analysis procedures employed in our study.

Furthermore, we contributed to the ongoing debate within the cell migration community, whether cells are pushed or pulled through constrictions. To address this, we analyzed the nuclear shapes across a wide spectrum of confinement widths. Our findings revealed transient deformations into oblate as well as prolate nuclear shapes, suggesting adaptive adjustment in cellular force generation in response to confinement. Specifically, pulling forces appear to dominate in wider constrictions, whereas pushing forces are dominant in narrower constrictions. We challenged our model by experimentally interfering with pulling forces and confirmed the increase in cytosolic calcium levels induced by significant nuclear deformations, leading to an increase of pushing forces. However, further experimental investigation into the mechanisms underlying force generation would be enlightening. For example, myosin II, a key player in both pulling and pushing forces, could provide deeper insights into the proposed adaptive force generation in response to confinement. Furthermore, our contradictory results from manipulating actomyosin contractility require further analysis. Both inhibition and enhancement of contractility resulted in a shift of force balance towards pushing, contrary to recent findings [34]. Subsequent investigations should include determining the mechanical properties of treated cells to comprehend the full effects of these drugs. Moreover, exploring these mechanisms in other cell lines with varying mechanical properties is essential, as increased nuclear plasticity could induce memory effects, thereby altering force generation. In sum, our work adds to this ongoing debate by providing evidence, that the force generating cytoskeleton adapts by switching from pulling to pushing forces to overcome constrictions.

Beyond the experimental assays developed in this study, photolithographic microstructuring holds promise for fabricating other 3D matrices for investigating cellular behavior. For example, the emerging field of microfluidics-based organ-on-a-chip technologies is gaining importance due to its potential to rapidly screen for personalized immunotherapy and facilitate the study of tumor-immune interactions in a patient-specific manner [154]. These technologies offer the potential of overcoming the limitations of traditional drug screening and testing by providing more physiological 3D microenvironments in a well-defined and highly reproducible manner. Hence, the polymerization of trapping structures based on PEG-NB hydrogel integrated into a microfluidic system could advance this emerging field.

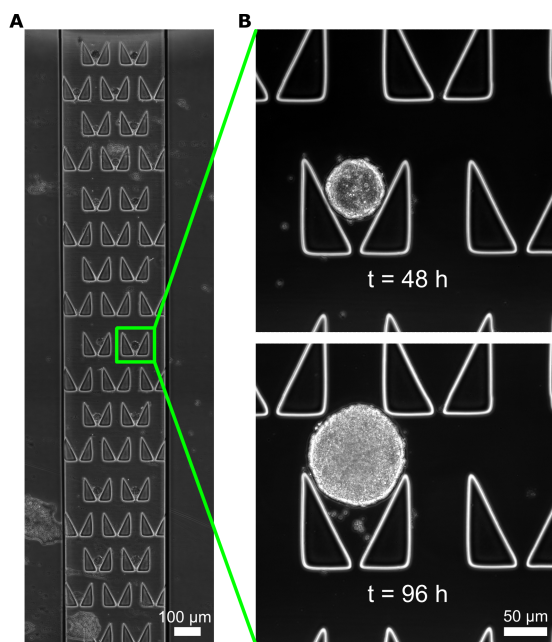


Figure 8.1: **Hydrogel structures for controlled development.** (A) Overview image of the trapping process of stem cell spheroids within a microfluidic chip (μ -slide VI 0.1, ibidi). (B) Illustration of the growth process of a trapped spheroid over 96 hours. Image courtesy of Ziya Göcergi.

This approach enables encapsulation of stem cell spheroids in a controlled manner, facilitating high-throughput processing (see Figure 8.1A). Microfluidic accessibility ensures sustained survivability and facilitates easy drug application. Meanwhile, the spheroids remain confined within the trapping structures for several days (see Figure 8.1B). Another approach within this microfluidic framework involves investigating stem cell fate in response to fluid flow.

In summary, the photo-lithographic micro-fabrication of synthetic hydrogel described in this study provides versatile artificial architectures for the study of cell mechanics. Initially, our focus was on elucidating the invasion behavior of distinct cancer cell lines, revealing variations in their responsiveness to environmental conditions. Additionally, we investigated repeated, self-imposed cell migration through compliant 3D channels, revealing a bi-phasic transition rate behavior relative to confinement width. To understand this phenomenon, we conducted an analysis of nuclear mechanics, characterizing the nucleus as a compressible elastic object with a Poisson ratio of 0.40. Furthermore, we explored the mechanisms underlying force generation to navigate through constrictions, observing a transition from pulling to pushing forces. These findings contribute to a more comprehensive understanding of the complex interplay between confinement, the nucleus, and the cytoskeleton during mesenchymal cell migration.

A. Materials and Methods

A.1 Microfabrication of Hydrogel-Based Structures

Microfabrication of 'Sponge clamp' Structures

To microstructure hydrogels in confinement, the precursor solution is pipetted into the channel of a μ -slide chemotaxis ibiTreat (ibidi). This precursor consists of polyethylene glycol norbornene (PEG-NB, JenKem Technology) with a molecular weight of 20 kDa at a concentration of 2-3 mM in phosphate-buffered saline (PBS). Additionally, an off-stoichiometric quantity of 1 kDa polyethylene glycol dithiol (PEG-dithiol, Sigma) 1 mM CRGDS peptide (Iris Biotech), and 3 mM lithium phenyl-trimethylbenzoylphosphinate (LAP, Sigma) photo-initiator are included in the precursor. The mechanical properties of the resulting hydrogel can be modified by adjusting the concentration of PEG-NB monomer and/or the amount of cross-linker. The cross-link ratio, denoted as r_c , is defined as the ratio between the functional groups of the cross-linker (two thiol groups per cross-linker molecule) and the functional groups of the PEG-NB monomer (four norbornene groups per monomer molecule).

$$r_c = \frac{2c(\text{dithiol})}{4c(\text{PEG} - \text{NB})} \quad (\text{A.1})$$

Subsequently, the precursor is illuminated at 40 mW cm^{-2} for 8 seconds. To achieve this, a collimated UV light source emitting at 365 nm (Rapp Optoelectronic GmbH) is directed through a structured chromium mask. The mask is designed with specifications for the hydrogel stripes: 700 μm in length, 100 μm in width, and 70 μm in height, with an initial block-to-block separation distance of 30-50 μm . Upon completion of polymerization of the hydrogel blocks, both reservoirs of the channel slide are thoroughly rinsed with PBS and allowed to swell fully overnight.

Microfabrication of Dumbbell-shaped Cavities

The experimental protocol employs a μ -Dish ibiTreat (ibidi) platform. To achieve a defined height for the hydrogel layer containing the desired structures, PDMS stamps were utilized. PDMS, with a monomer-to-cross-linker ratio of 10:1, was cast onto a specific silicon wafer, subjected to degassing, and left to cure overnight at

50°C. Subsequently, PDMS stamps, featuring small square pillars measuring $200 \times 200 \times 50 \mu\text{m}$, underwent a 3-minute O_2 activation process in a UV cleaner (PSD-UV, novascan). Following activation, the stamps were placed onto the μ -Dish. A droplet of PEG-NB hydrogel precursor was poured adjacent to the stamps and drawn into the free space created by the small pillars of the PDMS stamp. The precursor solution for hydrogel formation was formulated using PBS containing 5 mM of 20 kDa 8-armed PEG-norbornene (PEG-NB, JenKem Technology). To facilitate crosslinking, an off-stoichiometric amount (0.4 - 0.8) of 1 kDa PEG-dithiol was supplemented, along with 3 mM of the photo-initiator LAP. Incorporating the PEG-dithiol cross-linker and LAP enables the formation of a robust cross-linked hydrogel mesh. The mechanical characteristics of the resulting hydrogel can be directly tailored by adjusting the quantity of PEG-NB monomers and/or the amount of cross-linker. The cross-link ratio r_c is defined as the ratio of functional groups present in the cross-linker (two thiol groups per crosslinker) to the functional groups present in the PEG-NB monomer (eight norbornene groups per monomer).

$$r_c = \frac{2c(\text{dithiol})}{8c(\text{PEG} - \text{NB})} \quad (\text{A.2})$$

Fluorescent nano-beads, measuring $0.2 \mu\text{m}$ in diameter, were introduced into the precursor solution at a total concentration of $5.8\text{E}+08 \text{ ml}^{-1}$ (Distrilab). These embedded nano-beads serve as mechanical sensors owing to their elastic behavior within the hydrogel matrix. The hydrogel precursor was subsequently patterned selectively using the PRIMO module (Alvéole), which is integrated into an automated inverted microscope (Nikon Eclipse Ti). Design specifications for the desired hydrogel structures were generated using vector-based software (Inkscape) and then transferred into Leonardo software (Alvéole). Upon exposure to UV light at a wavelength of 365 nm, at a dosage of $3\text{mJ}/\text{mm}^2$, the precursor material was polymerized according to the predetermined pattern. Following photopolymerization, the PDMS stamps were removed, and the dish was thoroughly washed with milliQ water, followed by rehydration with PBS for 5 minutes. Subsequently, the μ -Dish was treated with a solution of human fibronectin (YO Proteins) at a concentration of $50 \mu\text{g ml}^{-1}$ for 45 minutes. The ECM protein selectively adheres to the bottom of the dumb-bell structures, which are composed of the μ -Dish substrate, due to the passivating properties of the PEG-NB hydrogel. After the incubation period, the μ -Dish was rinsed three times with PBS. Following a 45-minute interval, the μ -Dish was rinsed again with PBS and cells were seeded onto it.

A.2 Cell Culture

MDA-MB-231 human breast carcinoma epithelial cells, co-expressing histone-2B mCherry (provided by Timo Betz, Göttingen, and authenticated using a Cell Line Authentication Service from Eurofins Genomics), were maintained in standard growth medium, specifically L-15 (Sigma), supplemented with 10% fetal bovine serum (FBS, Thermo Fisher). Cell cultures were maintained at 37°C until reaching a confluency level of 80-90%. Subsequently, cells were rinsed and detached using

trypsin/EDTA (Thermo Fisher) for 4 minutes. For experimental procedures, the cell suspension was centrifuged at 1,000 r.c.f. for 3 minutes, followed by re-suspension in L-15 medium. Approximately 20,000 cells were seeded per μ -Dish (ibidi) and allowed to adhere for a minimum duration of 3 hours. In inhibitor experiments, 0.5 nM Calyculin A (Thermofisher) or 30 μ M Y-27632 (Sigma) were added 2 hours prior the start of the experiment. For live cell imaging of actin dynamics, MDA-MB-231 cells stably expressing LifeAct GFP (provided by Timo Betz, Göttingen) were utilized. HT-1080 cells were cultured in MEM (Thermo Fisher) supplemented with 10% FBS as standard growth conditions.

A.3 Transfection Procedure

Plasmid Vectors

The pDNA Paxillin-EGFP plasmid was graciously provided by Klemens Rottner (TU Braunschweig), while the mCherry DN-KASH plasmid was a generous gift from Daniel Conway (Addgene plasmid #125553). The pEGFP-N1 vector was purchased from Clontech. Additionally, the pVAX-A120-vector and the pSTI-A120-vector were kindly provided by Carsten Rudolph (ethris GmbH). To construct the desired vectors, the Gibson DNA assembly method was employed using the NEBuilder HiFi DNA Assembly kit from NEB (NEB, NEBuilder HiFi DNA Assembly Cloning Kit, E5520S) following standard protocols. Initially, a pVAX-KASH-EGFP vector was generated by integrating the KASH sequence from the mCherry DN-KASH vector and the EGFP sequence from the pSTIA120-vector into the pVAX-A120-vector. Specifically, the KASH and EGFP coding region were amplified by PCR using the Q5 High-Fidelity PCR Kit (NEB, E0555S). All oligonucleotide primers were designed to ensure at least a 25 bp overlap between the DNA fragments to be assembled. The assembly reaction mixture contained approximately 10 pmol of insert DNA and 2 pmol of NheI/EcoRI-linearized pVAX-A120-vector, and it was incubated at 50°C for 15 minutes. Following completion of the Gibson DNA assembly reaction, the mixture was transformed into chemically competent *E. coli* cells (NEB, NEB #C2987). Subsequently, 100 μ l of the transformed LB (Lysogeny Broth)-*E. coli* mixture was spread onto LB/Kanamycin plates and incubated at 37°C overnight. Individual colonies were selected, and positive clones were confirmed by DNA sequencing. One clone was chosen for further cloning steps to generate the pDNA-DN-KASH-EGFP vector. Briefly, the KASH-EGFP coding region was PCR amplified using the Q5 High-Fidelity PCR Kit (NEB, E0555S). Oligonucleotide primers for the KASH-EGFP fragment were designed to ensure at least a 26 bp overlap between the DNA fragments to be assembled. The assembly reaction mixture contained approximately 60 pmol of insert DNA and 20 pmol of AgeI/NotI-linearized mCherry DN-KASH vector, and it was incubated at 50°C for 15 minutes. After completion of the Gibson DNA assembly reaction, the mixture was transformed into chemically competent *E. coli* cells. Subsequently, 100 μ l of the transformed LB-*E. coli* mixture was spread onto LB/Kanamycin plates and incubated at 37°C overnight. Individual colonies were selected and positive clones were confirmed by DNA sequencing.

Transfection of MDA-MB-231 cells

MDA-MB-231 cells stably expressing H2B m-Cherry were plated in 6-well plates with an initial confluency ranging from 70% to 80%. Transfection was performed using a commercially available transfection reagent, TransIT-BrCa (Mirus), at a concentration of 1 μg of plasmid DNA (pDNA) per well, with a TransIT-BrCa to pDNA ratio of 2.0 μl TransIT-BRCa per 1 μg pDNA, following the manufacturer's protocol. Briefly, the pDNA was diluted in OptiMEM to a final volume of 200 μl , and TransIT-BrCa was added to the pDNA-OptiMEM solution. The mixture was incubated for 30 minutes at 3 room temperature before being added dropwise to the cells in complete growth media. The cells were then incubated with the TransIT-BRCa reagent:DNA complexes for 24 hours at 37°C in a total transfection volume of 2.5 ml. Subsequently, the transfected cells were detached and seeded into hydrogel-based dumbbell structures.

A.4 Time-Lapse Microscopy

Time-lapse measurements were conducted over 40 hours duration using either an inverted Nikon Eclipse Ti microscope or an inverted Nikon Eclipse Ti2 microscope. Observations were performed utilizing either 10x or 20x objective. Cells were either incubated with the Okulab incubation system (cage incubator with active humidity and temperature control) or the ibidi-incubation system (chamber incubator with active humidity and temperature control) under physiological conditions.

The samples were maintained within a controlled incubation environment at 37°C, facilitated by either an Okolabs or ibidi incubation chamber. Image acquisition was employed at 10-minute intervals with either 10x magnification (Nikon objective, MRH00101) or 20x magnification (Nikon objective, MRH00201). To enable cell tracking alternating brightfield and fluorescence imaging were taken. Brightfield illumination was carried out with a 100W warm white LED (MHLED100W), fluorescence illumination with a LED light source (lumencor, SOLA-SE II). EGFP fluorescence was captured with the EGFP filterset (Chroma, F46-002), mCherry fluorescence with the DsRed filterset (Chroma, F46-005). Images were captured using a CMOS camera (PCO, pco.edge4.2). Acquisition control was performed with the NIS-Elements Advanced Research software (Nikon). To enhance data acquisition efficiency, the setup was configured to capture multiple positions, allowing the microscope to cycle through them within each 10-minute interval.

For confocal microscopy, a Zeiss LSM9 980 with Airyscan 2 microscope was employed. Imaging of the samples was conducted using a 20x air objective. The microscope was equipped with gas incubation and a heating system (Okolab) to maintain consistent incubation conditions throughout the experiments. Z-Stacks with a depth of up to 20 μm were acquired to capture images of paxillin-GFP and nuclear volume, respectively.

A.5 Stiffness Evaluation via AFM

Atomic force microscopy (AFM) was utilized to evaluate the mechanical properties, including Young's modulus, of both the hydrogel matrix and the cell nuclei. Measurements were performed using a JPK NanoWizard II system (JPK instruments) interfaced with an inverted optical microscope (Zeiss, Axiovert 200M). Cantilevers with modified beads were employed, with diameters of either 3.5 μm (NanoAndMore GmbH; type: CP-PNPL-SiO-B, nominal spring constants of 0.08 N/M) or 3.6 μm (sQUBE, type: CP-CONT-PS-B, nominal force constants ranging between 0.02 and 0.77 N/m). To calibrate the cantilever sensitivity, the slope of the force-distance curve against a rigid petri dish substrate was recorded. Subsequently, the spring constant of the cantilevers were determined using the thermal noise method provided by the AFM software (JPK SPM). Young's modulus of the hydrogel was assessed by applying substantial forces (> 10 nN) through the bead, resulting in indentation depths of up to 2 μm . Similarly, the stiffness of cell nuclei was evaluated using the same AFM-based approach by applying a force of 5 nN of the nuclei. Typically, a square grid consisting of 64 points with 1 μm spacing between adjacent points was examined at a single position to ensure statistically robust results. Force-distance curves were acquired with an extension speed of 2.5 $\mu\text{m/s}$. The Young's moduli of the tested samples were determined by fitting the force-distance curves to a Hertz contact model.

B. Image and Data Analysis

B.1 Microscopy and Cell Tracking

Bright-field and fluorescence images of the fibronectin-coated pattern and the co-expressed labeled histones were captured every 10 minutes. To improve the clarity of the nuclei images, a bandpass filter was applied. Subsequently, the images were subjected to binarization, and the positions of the nuclei's center-of-mass were determined using the Analyze Particles plugin in ImageJ.

B.2 Measurement of the Hydrogel-Hydrogel Gap Width

The gap between hydrogel strips is visualized using GFP-labeled Dextran (MW 10 kDa), which is hindered from diffusing into the polymerized hydrogel owing to its molecular size. Subsequently, the intensity profile perpendicular to the hydrogel clefts is quantified, and a Gaussian fit is applied. The gap width is determined as the full width at half maximum (FWHM) of these Gaussian fits.

B.3 Cell Exclusion Criteria in 3D Dumbbells

We track the movement of numerous cells to ascertain the statistical transitions of cell migration through constrictions characterized by different bridge widths. To mitigate the influence of uncertain or anomalous migration patterns, we implement the following inclusion criteria during the analysis of migration within our hydrogel micro-cavities.

1. Only a single cell occupies the micro pattern. Trajectories are cut when the cell rounds up for division.
2. The cell and its protrusions are entirely confined within the borders of the microstructure.
3. Throughout the entirety of the experiment, the cell shows no abnormalities such as the presence of multiple nuclei, cell death, or detachment from the substrate.

4. Cell dynamic statistics are included when a protrusion forms and extends to the second adhesion-site, even if the cell is unable to transmigrate through the constriction.

Criteria 1-3 establish essential prerequisites for single-cell experiments conducted within micro-cavities, and these criteria are solely enforced for cells migrating within cavities devoid of constriction. Criterion 4, conversely, pertains exclusively to our dumbbell-shaped hydrogel cavities, as the migratory behavior of cells within these structures is significantly impacted by the width of the constricted region, notably with regard to physical confinement. Despite the incapacity of cells to traverse through these narrow constrictions, we include such cells in our analysis, as such behavior is deemed typical within this experimental framework.

B.4 Bead Displacement Analysis

Fluorescent nano-beads incorporated within the hydrogel matrix and the cell nuclei were tracked using the TrackPy Python package. To track particle movement, their displacement relative to a neutral reference position was calculated. For quantitative analysis of gel deformation, the tracking algorithm was utilized to trace the positions of a minimum of twenty embedded fluorescent nano-beads in each experiment. The displacement of these marker beads was visualized by determining the difference between their positions at each time point and their initial neutral positions. Given that the marker beads are embedded within the gel and possess a larger diameter of 200 nm compared to the approximate mesh size of the hydrogel (about 40 nm), their displacement field reflects the deformation field of the surrounding hydrogel.

B.5 Calcium Level Analysis

Cytosolic calcium concentrations were quantified under different degrees of spatial confinement employing the calcium indicator Calbryte 520 AM (aat bioquest). Experimental protocols comprised the fabrication of dumbbell-shaped micro-cavities, cell seeding, and subsequent administration of Calbryte520 AM at a concentration of 10 μ M following a two-hour incubation period. After a 45-minute incubation with the calcium indicator, dishes were gently rinsed prior to fluorescence microscopy imaging. Calcium levels within the cytosol were evaluated by integrating the fluorescent signal throughout the entire cytosolic region.

B.6 Nuclear Growth Analysis

To analyze temporal alterations in nuclear volume, z-stacks were acquired during a 20-hour time-lapse recording of MDA-MB-231 cells transmigrating through a constriction using confocal microscopy. For nuclear volume analysis, acquired data were imported into Arivis Vision 4D software (Zeiss). Subsequently, each dataset underwent initial bleach correction. Following this correction, individual nuclei were

segmented and subjected to size-based filtration to eliminate extraneous noise components. The segmented objects underwent manual proofreading, with parameters adjusted as necessary, facilitating the determination of nuclear volume within the software.

B.7 Collected Cell Statistics

Cell line	Bridge width	Cells	Transitions	Timepoints	Replicates
MDA-MB-231 FN	4.6 ± 0.7	144	82	16468	14
	6.7 ± 0.7	333	639	41127	16
	8.4 ± 0.4	211	434	26256	16
	10.1 ± 0.6	164	449	20770	16
	12.2 ± 0.6	102	279	13939	6
	20.4 ± 1.5	99	206	12351	4
	35.1 ± 1.4	249	318	27760	4
MDA-MB-231 w/o FN	7.1 ± 0.6	24	28	3725	4
	8.6 ± 0.3	43	37	6324	4
	10.0 ± 0.6	46	61	5695	4
	12.8 ± 0.8	52	38	6999	4
	15.0 ± 0.8	117	131	15957	4
	20.8 ± 0.4	13	19	2328	3
MDA-MB-231 Collagen	8 ± 1	101	450	14262	6
	14 ± 2	32	150	4000	6
	15.9 ± 0.7	35	161	5273	3
	24 ± 2	45	99	6123	3
MDA-MB-231 Laminin	7 ± 2	62	200	9747	6
	12 ± 2	61	248	9184	6
	16 ± 2	8	35	1282	6
	19.4 ± 0.8	45	72	6096	2
MDA-MB-231 DN-KASH	8 ± 2	50	60	8063	6
	13 ± 2	31	56	4796	6
	17 ± 2	31	26	4495	6
	22 ± 2	59	103	8121	3
MDA-MB-231 Calyculin A	6.8 ± 0.8	41	67	6007	2
	8.4 ± 0.3	29	57	3439	4
	10.2 ± 0.6	23	75	2672	4
	12.1 ± 0.7	12	37	1535	2
	19.2 ± 1.1	41	29	7005	2
MDA-MB-231 Y27632	4.3 ± 0.9	125	9	18101	10
	6.6 ± 0.7	237	85	30516	10
	8.5 ± 0.4	142	73	16333	8
	10.3 ± 0.7	115	98	14197	6
	12.1 ± 0.5	109	104	14144	4
	16.0 ± 0.9	153	133	20006	6
	19.7 ± 0.9	49	55	7005	4

Table B.1: Bridge widths w (in μm) of the micro-cavities and number of statistics collected. Number of cell trajectories, number of timepoints recorded, and amount of biological replicates for each bridge width w .

List of Abbreviations

1D	One Dimension(al)
2D	Two Dimensions/two-Dimensional
3D	Three Dimensions/Three-Dimensional
AFM	Atomic Force Microscopy
BC	Boundary Condition
BF	Brightfield
CLASP	Cytoplasmic Linker-Associated Proteins
CEM	Confinement Enhanced Migration
CRGDS	Cys-Arg-Gly-Asp-Ser
CRM	Confinement Reduced Migration
DMD	Digital Micromirror Device
DNA	Deoxyribonucleic Acid
ECM	Extracellular Matrix
EGFP	Enhanced Green Fluorescent Protein
EMT	Epithelial-to-Mesenchymal Transition
FA	Focal Adhesion
FBS	Fetal Bovine Serum
INM	Unncer Nuclear Membrane
LAP	Lithium Phenyl- 2,4,6-Trimethylbenzoylphosphinate
LINC	Linker of Nucleoskeleton and Cytoskeleton

MAT	Mesenchymal-Amoeboid Transition
MMP	Matrix Metalloproteinase
MSD	Mean Squared Displacement
NE	Nuclear Envelope
OU	Ornstein-Uhlenbeck process
PA	Poly(acrylamide)
PBS	Phosphate-Buffered Saline
PC	Phase Contrast
PDMS	Polydimethylsiloxane
PEG	Polyethylene Glycol
PEG-NB	PEG-norbornene
PMT	Photomultiplier Tube
PLL	Poly-L-Lysine
PVA	Poly(Vinyl Alcohol)
ROCK	Rho-associated Coiled-coil-containing protein Kinases
RGD	Tripeptide Motif Arg-Gly-Asp
TFM	Traction Force Microscopy
ULI	Underdamped Langevin Inference
UV	Ultraviolet

List of Figures

2.1	Illustration of the pivotal cytoskeletal components.	6
2.2	Single cell migration modes.	8
2.3	Illustration of the ECM impact on cell migration behavior.	9
2.4	Depiction of guidance cues.	11
2.5	Sketch of the cellular force generation mechanisms.	18
2.6	Sketch of the nuclear ruler model	19
2.7	Illustration of 2D and 3D cell culture.	21
2.8	Hydrogel classes.	22
2.9	Microfabrication processes.	25
2.10	Hookean solid.	28
2.11	Non-Newtonian behavior.	30
2.12	The Poisson's ratio experiences alteration due to geometric changes.	31
2.13	Illustration of contact mechanics.	33
3.1	Schematic overview of the PEG-NB hydrogel network components and characteristic swelling.	35
3.2	Schematic visualization of the epifluorescence microscope technique.	38
3.3	Working principle of AFM.	39
4.1	Visualization of the fabrication process and work principle of migratable hydrogel clefts.	42
4.2	Characterization of hydrogel properties.	43
4.3	Illustration of the final hydrogel-hydrogel interface.	44
4.4	Reproducibility and long-term stability of the hydrogel clefts.	45
4.5	Illustration of the invasion in hydrogel-hydrogel interfaces.	46
4.6	Characterization of the invasion capacity of cancerous cell lines within hydrogel clefts exhibiting different mechanical properties.	47
4.7	Comparison of migration dynamics between two distinct cancer cell lines invading hydrogel-hydrogel interfaces.	48
5.1	Schematic depiction of the fabrication process of 3D dumbbell-shaped micro-cavities.	52
5.2	Microscopic characterization of the 3D dumbbells.	53

5.3	Exemplary time-series of MDA-MB-231 cells.	55
5.4	Cell migration statistics for varying channel widths.	56
5.5	Cell migration statistics with different surface coatings.	57
5.6	Inferred non-linear dynamics of the nucleus for varying channel widths (from left to right: 4 μ m, 7 μ m, 9 μ m).	59
6.1	Aspect ratio of the nucleus for different channel widths (x-dimension/y-dimension).	65
6.2	Analysis of nuclear volume alterations over time.	66
6.3	Poisson ratio of MDA-MB-231 cell nuclei.	67
6.4	Analysis of the bead displacement.	69
6.5	Stiffness measurements of hydrogel and cell nuclei performed with an AFM.	70
6.6	Schematic visualization of the relevant contact mechanics setups.	71
6.7	Contact forces exerted from the nucleus to the hydrogel walls as a function of channel width.	72
7.1	Illustration of the nuclear dimensions.	77
7.2	Nuclear shape analysis.	78
7.3	Inhibition of pulling forces.	80
7.4	Effect of pulling inhibition on cell dynamics and nuclear shapes.	81
7.5	Cytosolic calcium levels at different degrees of confinement.	83
7.6	Effect of increased and decreased actomyosin contractility.	84
7.7	Mechanistic model for the adaptation of cellular forces to the degree of confinement.	86
7.8	Comparison of cell dynamics between simulation and experiment.	87
8.1	Hydrogel structures for controlled development.	94

List of Tables

- B.1 Bridge widths w (in μm) of the micro-cavities and number of statistics collected. Number of cell trajectories, number of timepoints recorded, and amount of biological replicates for each bridge width w 104

Bibliography

- [1] Bainbridge P. Wound healing and the role of fibroblasts. *Journal of Wound Care*, 22(8):407–412, August 2013.
- [2] H el ene D. Moreau, Matthieu Piel, Rapha el Voituriez, and Ana-Maria Lennon-Dum enil. Integrating Physical and Molecular Insights on Immune Cell Migration. *Trends in Immunology*, 39(8):632–643, August 2018.
- [3] Marcello Guarino, Barbara Rubino, and Gianmario Ballabio. The role of epithelial-mesenchymal transition in cancer pathology. *Pathology*, 39(3):305–318, June 2007.
- [4] Patrick Mehlen and Alain Puisieux. Metastasis: a question of life or death. *Nature Reviews Cancer*, 6(6):449–458, June 2006.
- [5] Christoph Schreiber, Behnam Amiri, Johannes C. J. Heyn, Joachim O. R adler, and Martin Falcke. On the adhesion–velocity relation and length adaptation of motile cells on stepped fibronectin lanes. *Proceedings of the National Academy of Sciences*, 118(4), January 2021. Publisher: Proceedings of the National Academy of Sciences.
- [6] Christoph Schreiber, Felix J. Segerer, Ernst Wagner, Andreas Roidl, and Joachim O. R adler. Ring-Shaped Microlanes and Chemical Barriers as a Platform for Probing Single-Cell Migration. *Scientific Reports*, 6(1), May 2016. Publisher: Springer Science and Business Media LLC.
- [7] Felix J. Segerer, Florian Th uroff, Alicia Piera Alberola, Erwin Frey, and Joachim O. R adler. Emergence and Persistence of Collective Cell Migration on Small Circular Micropatterns. *Physical Review Letters*, 114(22):228102, June 2015.
- [8] Kenneth M. Yamada and Edna Cukierman. Modeling Tissue Morphogenesis and Cancer in 3D. *Cell*, 130(4):601–610, August 2007.
- [9] Linda G. Griffith and Melody A. Swartz. Capturing complex 3D tissue physiology in vitro. *Nature Reviews Molecular Cell Biology*, 7(3):211–224, March 2006.
- [10] Christian Frantz, Kathleen M. Stewart, and Valerie M. Weaver. The extracellular matrix at a glance. *Journal of Cell Science*, 123(24):4195–4200, December 2010.

- [11] Lucas T. Vu, Gaurav Jain, Brandon D. Veres, and Padmavathy Rajagopalan. Cell Migration on Planar and Three-Dimensional Matrices: A Hydrogel-Based Perspective. *Tissue Engineering Part B: Reviews*, 21(1):67–74, February 2015.
- [12] Guoyou Huang, Fei Li, Xin Zhao, Yufei Ma, Yuhui Li, Min Lin, Guorui Jin, Tian Jian Lu, Guy M. Genin, and Feng Xu. Functional and Biomimetic Materials for Engineering of the Three-Dimensional Cell Microenvironment. *Chemical Reviews*, 117(20):12764–12850, October 2017. Publisher: American Chemical Society (ACS).
- [13] Christophe Helary, Alexandrine Foucault-Bertaud, Gaston Godeau, Bernard Coulomb, and Marie Madeleine Giraud Guille. Fibroblast populated dense collagen matrices: cell migration, cell density and metalloproteinases expression. *Biomaterials*, 26(13):1533–1543, May 2005.
- [14] Shomita S. Mathew-Steiner, Sashwati Roy, and Chandan K. Sen. Collagen in Wound Healing. *Bioengineering*, 8(5):63, May 2021.
- [15] Gabriel Benton, Irina Arnaoutova, Jay George, Hynda K. Kleinman, and Jennifer Koblinski. Matrigel: From discovery and ECM mimicry to assays and models for cancer research. *Advanced Drug Delivery Reviews*, 79-80:3–18, December 2014.
- [16] Renaud Poincloux, Olivier Collin, Floria Lizárraga, Maryse Romao, Marcel Debray, Matthieu Piel, and Philippe Chavrier. Contractility of the cell rear drives invasion of breast tumor cells in 3D Matrigel. *Proceedings of the National Academy of Sciences*, 108(5):1943–1948, February 2011.
- [17] Murat Guvendiren and Jason A Burdick. Engineering synthetic hydrogel microenvironments to instruct stem cells. *Current Opinion in Biotechnology*, 24(5):841–846, October 2013.
- [18] Chien-Chi Lin, Chang Seok Ki, and Han Shih. Thiol-norbornene photoclick hydrogels for tissue engineering applications. *Journal of Applied Polymer Science*, 132(8):n/a–n/a, October 2014. Publisher: Wiley.
- [19] Patricia M. Davidson, Aude Battistella, Théophile Déjardin, Timo Betz, Julie Plastino, Nicolas Borghi, Bruno Cadot, and Cécile Sykes. Nesprin-2 accumulates at the front of the nucleus during confined cell migration. *EMBO reports*, 21(7), May 2020. Publisher: EMBO.
- [20] Patricia M. Davidson, Josiah Sliz, Philipp Isermann, Celine Denais, and Jan Lammerding. Design of a microfluidic device to quantify dynamic intra-nuclear deformation during cell migration through confining environments. *Integrative Biology*, 7(12):1534–1546, 2015. Publisher: Oxford University Press (OUP).
- [21] Alexandros Afthinos, Kaustav Bera, Junjie Chen, Altug Ozcelikkale, Alice Amitrano, Mohammad Iqbal Choudhury, Randy Huang, Pavlos Pachidis,

- Panagiotis Mistriotis, Yun Chen, and Konstantinos Konstantopoulos. Migration and 3D Traction Force Measurements inside Compliant Microchannels. *Nano Letters*, 22(18):7318–7327, September 2022. Publisher: American Chemical Society (ACS).
- [22] Meng Wang, Bo Cheng, Yaowei Yang, Han Liu, Guoyou Huang, Lichun Han, Fei Li, and Feng Xu. Microchannel Stiffness and Confinement Jointly Induce the Mesenchymal-Amoeboid Transition of Cancer Cell Migration. *Nano Letters*, 19(9):5949–5958, August 2019. Publisher: American Chemical Society (ACS).
- [23] David B. Brückner, Alexandra Fink, Christoph Schreiber, Peter J. F. Röttgermann, Joachim O. Rädler, and Chase P. Broedersz. Stochastic nonlinear dynamics of confined cell migration in two-state systems. *Nature Physics*, 15(6):595–601, March 2019. Publisher: Springer Science and Business Media LLC.
- [24] Farshid Guilak, John R. Tedrow, and Rainer Burgkart. Viscoelastic Properties of the Cell Nucleus. *Biochemical and Biophysical Research Communications*, 269(3):781–786, March 2000.
- [25] Christopher Beadle, Marcela C. Assanah, Pascale Monzo, Richard Vallee, Steven S. Rosenfeld, and Peter Canoll. The Role of Myosin II in Glioma Invasion of the Brain. *Molecular Biology of the Cell*, 19(8):3357–3368, August 2008.
- [26] Alexandra Lynn McGregor, Chieh-Ren Hsia, and Jan Lammerding. Squish and squeeze — the nucleus as a physical barrier during migration in confined environments. *Current Opinion in Cell Biology*, 40:32–40, June 2016. Publisher: Elsevier BV.
- [27] Yi Fu, Lip Ket Chin, Tarik Bourouina, Ai Qin Liu, and Antonius M. J. Van Dongen. Nuclear deformation during breast cancer cell transmigration. *Lab on a Chip*, 12(19):3774, 2012. Publisher: Royal Society of Chemistry (RSC).
- [28] Peter Friedl, Katarina Wolf, and Jan Lammerding. Nuclear mechanics during cell migration. *Current Opinion in Cell Biology*, 23(1):55–64, February 2011. Publisher: Elsevier BV.
- [29] Takamasa Harada, Joe Swift, Jerome Irianto, Jae-Won Shin, Kyle R. Spinler, Avathamsa Athirasala, Rocky Diegmiller, P. C. Dave P. Dingal, Irena L. Ivanovska, and Dennis E. Discher. Nuclear lamin stiffness is a barrier to 3D migration, but softness can limit survival. *Journal of Cell Biology*, 204(5):669–682, February 2014. Publisher: Rockefeller University Press.
- [30] A. J. Lomakin, C. J. Cattin, D. Cuvelier, Z. Alraies, M. Molina, G. P. F. Nader, N. Srivastava, P. J. Sáez, J. M. Garcia-Arcos, I. Y. Zhitnyak, A. Bhargava, M. K. Driscoll, E. S. Welf, R. Fiolka, R. J. Petrie, N. S. De Silva,

- J. M. González-Granado, N. Manel, A. M. Lennon-Duménil, D. J. Müller, and M. Piel. The nucleus acts as a ruler tailoring cell responses to spatial constraints. *Science*, 370(6514):eaba2894, October 2020. Publisher: American Association for the Advancement of Science (AAAS).
- [31] Valeria Venturini, Fabio Pezzano, Frederic Català Castro, Hanna-Maria Häkkinen, Senda Jiménez-Delgado, Mariona Colomer-Rosell, Monica Marro, Queralt Tolosa-Ramon, Sonia Paz-López, Miguel A. Valverde, Julian Weghuber, Pablo Loza-Alvarez, Michael Krieg, Stefan Wieser, and Verena Ruprecht. The nucleus measures shape changes for cellular proprioception to control dynamic cell behavior. *Science*, 370(6514):eaba2644, October 2020. Publisher: American Association for the Advancement of Science (AAAS).
- [32] Xuan Cao, Emad Moeendarbary, Philipp Isermann, Patricia M. Davidson, Xiao Wang, Michelle B. Chen, Anya K. Burkart, Jan Lammerding, Roger D. Kamm, and Vivek B. Shenoy. A Chemomechanical Model for Nuclear Morphology and Stresses during Cell Transendothelial Migration. *Biophysical Journal*, 111(7):1541–1552, October 2016. Publisher: Elsevier BV.
- [33] Dustin G. Thomas, Aishwarya Yenepalli, Celine Marie Denais, Andrew Rape, Jordan R. Beach, Yu-li Wang, William P. Schiemann, Harihara Baskaran, Jan Lammerding, and Thomas T. Egelhoff. Non-muscle myosin IIB is critical for nuclear translocation during 3D invasion. *Journal of Cell Biology*, 210(4):583–594, August 2015. Publisher: Rockefeller University Press.
- [34] Jeremy T. Keys, Brian C. H. Cheung, Mingming Wu, and Jan Lammerding. Rear cortex contraction aids in nuclear transit during confined migration by increasing pressure in the cell posterior. September 2022. Publisher: Cold Spring Harbor Laboratory.
- [35] Robert J. Ju, Alistair D. Falconer, Kevin M. Dean, Reto P. Fiolka, David P. Sester, Max Nobis, Paul Timpson, Alexis J. Lomakin, Gaudenz Danuser, Melanie D. White, Dietmar B. Oelz, Nikolas K. Haass, and Samantha J. Stehbens. Compression-dependent microtubule reinforcement comprises a mechanostat which enables cells to navigate confined environments. preprint, *Cell Biology*, February 2022.
- [36] A. C. Rowat, J. Lammerding, and J. H. Ipsen. Mechanical Properties of the Cell Nucleus and the Effect of Emerin Deficiency. *Biophysical Journal*, 91(12):4649–4664, December 2006. Publisher: Elsevier BV.
- [37] Peter Friedl and Katarina Wolf. Plasticity of cell migration: a multiscale tuning model. *Journal of Cell Biology*, 188(1):11–19, December 2009. Publisher: Rockefeller University Press.
- [38] Stephan Barrientos, Olivera Stojadinovic, Michael S. Golinko, Harold Brem, and Marjana Tomic-Canic. PERSPECTIVE ARTICLE: Growth factors and cytokines in wound healing. *Wound Rep Reg*, 16(5):585–601, September 2008. Publisher: Wiley.

- [39] Feini Qu, Farshid Guilak, and Robert L. Mauck. Cell migration: implications for repair and regeneration in joint disease. *Nature Reviews Rheumatology*, 15(3):167–179, January 2019. Publisher: Springer Science and Business Media LLC.
- [40] Andrew D. Doyle, Ryan J. Petrie, Matthew L. Kutys, and Kenneth M. Yamada. Dimensions in cell migration. *Current Opinion in Cell Biology*, 25(5):642–649, October 2013. Publisher: Elsevier BV.
- [41] Daniel A. Fletcher and R. Dyche Mullins. Cell mechanics and the cytoskeleton. *Nature*, 463(7280):485–492, January 2010.
- [42] F Julicher, K Kruse, J Prost, and J Joanny. Active behavior of the Cytoskeleton. *Physics Reports*, 449(1-3):3–28, September 2007.
- [43] Douglas A Lauffenburger and Alan F Horwitz. Cell Migration: A Physically Integrated Molecular Process. *Cell*, 84(3):359–369, February 1996.
- [44] Thomas D. Pollard. The cytoskeleton, cellular motility and the reductionist agenda. *Nature*, 422(6933):741–745, April 2003.
- [45] Richard H. Wade. On and Around Microtubules: An Overview. *Molecular Biotechnology*, 43(2):177–191, October 2009.
- [46] Kari Barlan and Vladimir I. Gelfand. Microtubule-Based Transport and the Distribution, Tethering, and Organization of Organelles. *Cold Spring Harbor Perspectives in Biology*, 9(5):a025817, May 2017.
- [47] Martin Bähler. Myosins on the move to signal transduction. *Current Opinion in Cell Biology*, 8(1):18–22, February 1996.
- [48] Hans M. Warrick and James A. Spudich. Myosin Structure and Function in Cell Motility. *Annual Review of Cell Biology*, 3(1):379–421, November 1987.
- [49] Adrian F. Pegoraro, Paul Janmey, and David A. Weitz. Mechanical Properties of the Cytoskeleton and Cells. *Cold Spring Harbor Perspectives in Biology*, 9(11):a022038, November 2017.
- [50] Harald Herrmann and Ueli Aebi. Intermediate Filaments: Structure and Assembly. *Cold Spring Harbor Perspectives in Biology*, 8(11):a018242, November 2016.
- [51] Fang Cheng and John E. Eriksson. Intermediate Filaments and the Regulation of Cell Motility during Regeneration and Wound Healing. *Cold Spring Harbor Perspectives in Biology*, 9(9):a022046, September 2017.
- [52] Emily S. Bell, Pragma Shah, Noam Zuela-Sopilniak, Dongsung Kim, Alice-Anais Varlet, Julien L. P. Morival, Alexandra L. McGregor, Philipp Isermann, Patricia M. Davidson, Joshua J. Elacqua, Jonathan N. Lakins, Linda Vahdat, Valerie M. Weaver, Marcus B. Smolka, Paul N. Span, and Jan Lammerding.

- Low lamin A levels enhance confined cell migration and metastatic capacity in breast cancer. *Oncogene*, 41(36):4211–4230, September 2022.
- [53] Alexia I. Bachir, Alan Rick Horwitz, W. James Nelson, and Julie M. Bianchini. Actin-Based Adhesion Modules Mediate Cell Interactions with the Extracellular Matrix and Neighboring Cells. *Cold Spring Harbor Perspectives in Biology*, 9(7):a023234, July 2017.
- [54] Benjamin Geiger, Joachim P. Spatz, and Alexander D. Bershadsky. Environmental sensing through focal adhesions. *Nature Reviews Molecular Cell Biology*, 10(1):21–33, January 2009.
- [55] Peter Friedl and Darren Gilmour. Collective cell migration in morphogenesis, regeneration and cancer. 10(7):445–457, July 2009. Publisher: Springer Science and Business Media LLC.
- [56] Miguel Vicente-Manzanares, Xuefei Ma, Robert S. Adelstein, and Alan Rick Horwitz. Non-muscle myosin II takes centre stage in cell adhesion and migration. *Nature Reviews Molecular Cell Biology*, 10(11):778–790, November 2009.
- [57] Katarina Wolf, Regina Müller, Stefan Borgmann, Eva.-B. Bröcker, and Peter Friedl. Amoeboid shape change and contact guidance: T-lymphocyte crawling through fibrillar collagen is independent of matrix remodeling by MMPs and other proteases. *Blood*, 102(9):3262–3269, November 2003.
- [58] Brian Knight, Christina Laukaitis, Nasreen Akhtar, Neil A. Hotchin, Magnus Edlund, and Alan Rick Horwitz. Visualizing muscle cell migration in situ. *Current Biology*, 10(10):576–585, May 2000.
- [59] Kunito Yoshida and Thierry Soldati. Dissection of amoeboid movement into two mechanically distinct modes. *Journal of Cell Science*, 119(18):3833–3844, September 2006.
- [60] Tim Lämmermann and Michael Sixt. Mechanical modes of ‘amoeboid’ cell migration. *Current Opinion in Cell Biology*, 21(5):636–644, October 2009.
- [61] Remi-Martin Laberge, Pierre Awad, Judith Campisi, and Pierre-Yves Desprez. Epithelial-Mesenchymal Transition Induced by Senescent Fibroblasts. *Cancer Microenvironment*, 5(1):39–44, April 2012.
- [62] Robin J. McAnulty. Fibroblasts and myofibroblasts: Their source, function and role in disease. *The International Journal of Biochemistry & Cell Biology*, 39(4):666–671, 2007.
- [63] Peter Friedl and Katarina Wolf. Proteolytic interstitial cell migration: a five-step process. *Cancer and Metastasis Reviews*, 28(1-2):129–135, June 2009.

- [64] Kolade Adebawale, Ze Gong, Jay C. Hou, Katrina M. Wisdom, Damien Garbett, Hong-pyo Lee, Sungmin Nam, Tobias Meyer, David J. Odde, Vivek B. Shenoy, and Ovijit Chaudhuri. Enhanced substrate stress relaxation promotes filopodia-mediated cell migration. *Nature Materials*, 20(9):1290–1299, September 2021.
- [65] Hayri E. Balcioglu, Lakshmi Balasubramaniam, Tomita Vasilica Stirbat, Bryant L. Doss, Marc-Antoine Fardin, René-Marc Mège, and Benoit Ladoux. A subtle relationship between substrate stiffness and collective migration of cell clusters. *Soft Matter*, 16(7):1825–1839, 2020.
- [66] A. Y. Alexandrova. Evolution of cell interactions with extracellular matrix during carcinogenesis. *Biochemistry (Moscow)*, 73(7):733–741, July 2008.
- [67] Caroline Bonnans, Jonathan Chou, and Zena Werb. Remodelling the extracellular matrix in development and disease. *Nature Reviews Molecular Cell Biology*, 15(12):786–801, December 2014.
- [68] Ovijit Chaudhuri, Justin Cooper-White, Paul A. Janmey, David J. Mooney, and Vivek B. Shenoy. Effects of extracellular matrix viscoelasticity on cellular behaviour. *Nature*, 584(7822):535–546, August 2020.
- [69] Muhammad H. Zaman, Roger D. Kamm, Paul Matsudaira, and Douglas A. Lauffenburger. Computational Model for Cell Migration in Three-Dimensional Matrices. *Biophysical Journal*, 89(2):1389–1397, August 2005.
- [70] Muhammad H. Zaman, Linda M. Trapani, Alisha L. Sieminski, Drew MacKellar, Haiyan Gong, Roger D. Kamm, Alan Wells, Douglas A. Lauffenburger, and Paul Matsudaira. Migration of tumor cells in 3D matrices is governed by matrix stiffness along with cell-matrix adhesion and proteolysis. *Proceedings of the National Academy of Sciences*, 103(29):10889–10894, July 2006.
- [71] Katrina M. Wisdom, Kolade Adebawale, Julie Chang, Joanna Y. Lee, Sungmin Nam, Rajiv Desai, Ninna Struck Rossen, Marjan Rafat, Robert B. West, Louis Hodgson, and Ovijit Chaudhuri. Matrix mechanical plasticity regulates cancer cell migration through confining microenvironments. *Nature Communications*, 9(1), October 2018. Publisher: Springer Science and Business Media LLC.
- [72] Florian Geiger, Daniel Rüdiger, Stefan Zahler, and Hanna Engelke. Fiber stiffness, pore size and adhesion control migratory phenotype of MDA-MB-231 cells in collagen gels. *PLOS ONE*, 14(11):e0225215, November 2019. Publisher: Public Library of Science (PLOS).
- [73] Lena A. Lautscham, Christoph Kämmerer, Janina R. Lange, Thorsten Kolb, Christoph Mark, Achim Schilling, Pamela L. Strissel, Reiner Strick, Caroline Gluth, Amy C. Rowat, Claus Metzner, and Ben Fabry. Migration in Confined 3D Environments Is Determined by a Combination of Adhesiveness, Nuclear

- Volume, Contractility, and Cell Stiffness. *Biophysical Journal*, 109(5):900–913, September 2015. Publisher: Elsevier BV.
- [74] Laurent Fattet, Hae-Yun Jung, Mike W. Matsumoto, Brandon E. Aubol, Aditya Kumar, Joseph A. Adams, Albert C. Chen, Robert L. Sah, Adam J. Engler, Elena B. Pasquale, and Jing Yang. Matrix Rigidity Controls Epithelial-Mesenchymal Plasticity and Tumor Metastasis via a Mechanoresponsive EPHA2/LYN Complex. *Developmental Cell*, 54(3):302–316.e7, August 2020.
- [75] Andres Rubiano, Daniel Delitto, Song Han, Michael Gerber, Carly Galitz, Jose Trevino, Ryan M. Thomas, Steven J. Hughes, and Chelsey S. Simmons. Viscoelastic properties of human pancreatic tumors and in vitro constructs to mimic mechanical properties. *Acta Biomaterialia*, 67:331–340, February 2018.
- [76] Ralph Sinkus, Katja Siegmann, Tanja Xydeas, Mickael Tanter, Claus Claussen, and Mathias Fink. MR elastography of breast lesions: Understanding the solid/liquid duality can improve the specificity of contrast-enhanced MR mammography. *Magnetic Resonance in Medicine*, 58(6):1135–1144, December 2007.
- [77] Shuvasree SenGupta, Carole A. Parent, and James E. Bear. The principles of directed cell migration. *Nature Reviews Molecular Cell Biology*, 22(8):529–547, May 2021. Publisher: Springer Science and Business Media LLC.
- [78] Laura Lara Rodriguez and Ian C. Schneider. Directed cell migration in multicue environments. *Integrative Biology*, 5(11):1306–1323, November 2013.
- [79] Pavlo G. Gritsenko, Olga Ilina, and Peter Friedl. Interstitial guidance of cancer invasion. *The Journal of Pathology*, 226(2):185–199, January 2012.
- [80] P. Clark, P. Connolly, A. S. G. Curtis, J. A. T. Dow, and C. D. W. Wilkinson. Cell guidance by ultrafine topography *in vitro*. *Journal of Cell Science*, 99(1):73–77, May 1991.
- [81] Liesbeth Micholt, Annette Gärtner, Dimitar Prodanov, Dries Braeken, Carlos G. Dotti, and Carmen Bartic. Substrate Topography Determines Neuronal Polarization and Growth In Vitro. *PLoS ONE*, 8(6):e66170, June 2013.
- [82] Anastasios Marmaras, Tobias Lendenmann, Gianluca Civenni, Davide Franco, Dimos Poulidakos, Vartan Kurtcuoglu, and Aldo Ferrari. Topography-mediated apical guidance in epidermal wound healing. *Soft Matter*, 8(26):6922, 2012.
- [83] Bin Wang, Jian Shi, Jin Wei, Xiaolong Tu, and Yong Chen. Fabrication of elastomer pillar arrays with elasticity gradient for cell migration, elongation and patterning. *Biofabrication*, 11(4):045003, July 2019.
- [84] Chun-Min Lo, Hong-Bei Wang, Micah Dembo, and Yu-li Wang. Cell Movement Is Guided by the Rigidity of the Substrate. *Biophysical Journal*, 79(1):144–152, July 2000.

- [85] Brett C. Isenberg, Paul A. DiMilla, Matthew Walker, Sooyoung Kim, and Joyce Y. Wong. Vascular Smooth Muscle Cell Durotaxis Depends on Substrate Stiffness Gradient Strength. *Biophysical Journal*, 97(5):1313–1322, September 2009.
- [86] Matthew Raab, Joe Swift, P.C. Dave P. Dingal, Palak Shah, Jae-Won Shin, and Dennis E. Discher. Crawling from soft to stiff matrix polarizes the cytoskeleton and phosphoregulates myosin-II heavy chain. *Journal of Cell Biology*, 199(4):669–683, November 2012.
- [87] Raimon Sunyer, Vito Conte, Jorge Escribano, Alberto Elosegui-Artola, Anna Labernadie, Léo Valon, Daniel Navajas, José Manuel García-Aznar, José J. Muñoz, Pere Roca-Cusachs, and Xavier Trepap. Collective cell durotaxis emerges from long-range intercellular force transmission. *Science*, 353(6304):1157–1161, September 2016.
- [88] Lingling Liu, Qing Luo, Jinghui Sun, and Guanbin Song. Nucleus and nucleus-cytoskeleton connections in 3D cell migration. 348(1):56–65, October 2016. Publisher: Elsevier BV.
- [89] Brian J. DuChes, Andrew D. Doyle, Emiliós K. Dimitriadis, and Kenneth M. Yamada. Durotaxis by Human Cancer Cells. *Biophysical Journal*, 116(4):670–683, February 2019.
- [90] Andrew J. McKenzie, Stephanie R. Hicks, Kathryn V. Svec, Hannah Naughton, Zöe L. Edmunds, and Alan K. Howe. The mechanical microenvironment regulates ovarian cancer cell morphology, migration, and spheroid disaggregation. *Scientific Reports*, 8(1), May 2018. Publisher: Springer Science and Business Media LLC.
- [91] O. Moreno-Arotzena, C. Borau, N. Movilla, M. Vicente-Manzanares, and J. M. García-Aznar. Fibroblast Migration in 3D is Controlled by Haptotaxis in a Non-muscle Myosin II-Dependent Manner. *Annals of Biomedical Engineering*, 43(12):3025–3039, December 2015.
- [92] S Aznavoorian, M L Stracke, H Krutzsch, E Schiffmann, and L A Liotta. Signal transduction for chemotaxis and haptotaxis by matrix molecules in tumor cells. *The Journal of cell biology*, 110(4):1427–1438, April 1990.
- [93] Michele Weber, Robert Hauschild, Jan Schwarz, Christine Moussion, Ingrid De Vries, Daniel F. Legler, Sanjiv A. Luther, Tobias Bollenbach, and Michael Sixt. Interstitial Dendritic Cell Guidance by Haptotactic Chemokine Gradients. *Science*, 339(6117):328–332, January 2013.
- [94] Amit Kumar Rana, Yang Li, Qiujié Dang, and Fan Yang. Monocytes in rheumatoid arthritis: Circulating precursors of macrophages and osteoclasts and, their heterogeneity and plasticity role in RA pathogenesis. *International Immunopharmacology*, 65:348–359, December 2018.

- [95] A. Planagumà, T. Domènech, M. Pont, E. Calama, V. García-González, R. López, M. Aulí, M. López, S. Fonquerna, I. Ramos, J. De Alba, A. Nueda, N. Prats, V. Segarra, M. Miralpeix, and M.D. Lehner. Combined anti CXC receptors 1 and 2 therapy is a promising anti-inflammatory treatment for respiratory diseases by reducing neutrophil migration and activation. *Pulmonary Pharmacology & Therapeutics*, 34:37–45, October 2015.
- [96] Carole A. Parent and Peter N. Devreotes. A Cell’s Sense of Direction. *Science*, 284(5415):765–770, April 1999.
- [97] Anna Bagorda and Carole A. Parent. Eukaryotic chemotaxis at a glance. *Journal of Cell Science*, 121(16):2621–2624, August 2008.
- [98] Peter J. M. Van Haastert and Peter N. Devreotes. Chemotaxis: signalling the way forward. *Nature Reviews Molecular Cell Biology*, 5(8):626–634, August 2004.
- [99] Marc Tessier-Lavigne and Corey S. Goodman. The Molecular Biology of Axon Guidance. *Science*, 274(5290):1123–1133, November 1996.
- [100] David E Koser, Amelia J Thompson, Sarah K Foster, Asha Dwivedy, Eva K Pillai, Graham K Sheridan, Hanno Svoboda, Matheus Viana, Luciano Da F Costa, Jochen Guck, Christine E Holt, and Kristian Franze. Mechanosensing is critical for axon growth in the developing brain. *Nature Neuroscience*, 19(12):1592–1598, December 2016.
- [101] A. R. Bausch and K. Kroy. A bottom-up approach to cell mechanics. *Nature Physics*, 2(4):231–238, April 2006.
- [102] C.P. Broedersz and F.C. MacKintosh. Modeling semiflexible polymer networks. *Reviews of Modern Physics*, 86(3):995–1036, July 2014.
- [103] Paolo Maiuri, Jean-François Rupprecht, Stefan Wieser, Verena Ruprecht, Olivier Bénichou, Nicolas Carpi, Mathieu Coppey, Simon De Beco, Nir Gov, Carl-Philipp Heisenberg, Carolina Lage Crespo, Franziska Lautenschlaeger, Maël Le Berre, Ana-Maria Lennon-Dumenil, Matthew Raab, Hawa-Racine Thiam, Matthieu Piel, Michael Sixt, and Raphaël Voituriez. Actin Flows Mediate a Universal Coupling between Cell Speed and Cell Persistence. *Cell*, 161(2):374–386, April 2015.
- [104] Frank Jülicher, Stephan W Grill, and Guillaume Salbreux. Hydrodynamic theory of active matter. *Reports on Progress in Physics*, 81(7):076601, July 2018.
- [105] David B Brückner and Chase P Broedersz. Learning dynamical models of single and collective cell migration: a review. *Reports on Progress in Physics*, 87(5):056601, May 2024.

- [106] Philipp J. Albert and Ulrich S. Schwarz. Dynamics of Cell Shape and Forces on Micropatterned Substrates Predicted by a Cellular Potts Model. *Biophysical Journal*, 106(11):2340–2352, June 2014.
- [107] Danying Shao, Herbert Levine, and Wouter-Jan Rappel. Coupling actin flow, adhesion, and morphology in a computational cell motility model. *Proceedings of the National Academy of Sciences*, 109(18):6851–6856, May 2012.
- [108] Reinhold Frth. Die Brownsche Bewegung bei Berücksichtigung einer Persistenz der Bewegungsrichtung. Mit Anwendungen auf die Bewegung lebender Infusorien. *Zeitschrift für Physik*, 2(3):244–256, June 1920.
- [109] Daniel Campos, Vicenç Méndez, and Isaac Llopis. Persistent random motion: Uncovering cell migration dynamics. *Journal of Theoretical Biology*, 267(4):526–534, December 2010.
- [110] G. A. Dunn and A. F. Brown. A Unified Approach to Analysing Cell Motility. *Journal of Cell Science*, 1987(Supplement_8):81–102, March 1987.
- [111] Mitchell H. Gail and Charles W. Boone. The Locomotion of Mouse Fibroblasts in Tissue Culture. *Biophysical Journal*, 10(10):980–993, October 1970.
- [112] Pierre Sens. Stick–slip model for actin-driven cell protrusions, cell polarization, and crawling. *Proceedings of the National Academy of Sciences*, 117(40):24670–24678, October 2020.
- [113] Grégory Giannone, Benjamin J. Dubin-Thaler, Olivier Rossier, Yunfei Cai, Oleg Chaga, Guoying Jiang, William Beaver, Hans-Günther Döbereiner, Yoav Freund, Gary Borisy, and Michael P. Sheetz. Lamellipodial Actin Mechanically Links Myosin Activity with Adhesion-Site Formation. *Cell*, 128(3):561–575, February 2007.
- [114] Grégory Giannone, Benjamin J Dubin-Thaler, Hans-Günther Döbereiner, Nelly Kieffer, Anne R Bresnick, and Michael P Sheetz. Periodic Lamellipodial Contractions Correlate with Rearward Actin Waves. *Cell*, 116(3):431–443, February 2004.
- [115] Patricia T. Yam, Cyrus A. Wilson, Lin Ji, Benedict Hebert, Erin L. Barnhart, Natalie A. Dye, Paul W. Wiseman, Gaudenz Danuser, and Julie A. Theriot. Actin–myosin network reorganization breaks symmetry at the cell rear to spontaneously initiate polarized cell motility. *The Journal of Cell Biology*, 178(7):1207–1221, September 2007.
- [116] David B. Brückner, Matthew Schmitt, Alexandra Fink, Georg Ladurner, Johannes Flommersfeld, Nicolas Arlt, Edouard Hannezo, Joachim O. Rädler, and Chase P. Broedersz. Geometry Adaptation of Protrusion and Polarity Dynamics in Confined Cell Migration. *Physical Review X*, 12(3):031041, September 2022. Publisher: American Physical Society (APS).

- [117] Johannes Flommersfeld, Stefan Stöberl, Omar Shah, Joachim O. Rädler, and Chase P. Broedersz. Geometry-Sensitive Protrusion Growth Directs Confined Cell Migration. *Physical Review Letters*, 132(9):098401, February 2024.
- [118] Katarina Wolf, Mariska te Lindert, Marina Krause, Stephanie Alexander, Joost te Riet, Amanda L. Willis, Robert M. Hoffman, Carl G. Figdor, Stephen J. Weiss, and Peter Friedl. Physical limits of cell migration: Control by ECM space and nuclear deformation and tuning by proteolysis and traction force. *J. Cell Biol.*, 201(7):1069–1084, June 2013. Publisher: Rockefeller University Press.
- [119] Zongjian Jia, Laurence Barbier, Heather Stuart, Mohammad Amraei, Steven Pelech, James W. Dennis, Pavel Metalnikov, Paul O’Donnell, and Ivan R. Nabi. Tumor Cell Pseudopodial Protrusions. *Journal of Biological Chemistry*, 280(34):30564–30573, August 2005.
- [120] Patricia M. Davidson and Jan Lammerding. Broken nuclei – lamins, nuclear mechanics, and disease. *Trends in Cell Biology*, 24(4):247–256, April 2014.
- [121] ZiQiu Tong, Eric M. Balzer, Matthew R. Dallas, Wei-Chien Hung, Kathleen J. Stebe, and Konstantinos Konstantopoulos. Chemotaxis of Cell Populations through Confined Spaces at Single-Cell Resolution. *PLoS ONE*, 7(1):e29211, January 2012.
- [122] C. M. Denais, R. M. Gilbert, P. Isermann, A. L. McGregor, M. te Lindert, B. Weigelin, P. M. Davidson, P. Friedl, K. Wolf, and J. Lammerding. Nuclear envelope rupture and repair during cancer cell migration. *Science*, 352(6283):353–358, March 2016. Publisher: American Association for the Advancement of Science (AAAS).
- [123] Kavitha Sarma and Danny Reinberg. Histone variants meet their match. *Nature Reviews Molecular Cell Biology*, 6(2):139–149, February 2005.
- [124] Ashwin Unnikrishnan, Philip R Gafken, and Toshio Tsukiyama. Dynamic changes in histone acetylation regulate origins of DNA replication. *Nature Structural & Molecular Biology*, 17(4):430–437, April 2010.
- [125] Katalin Fejes Tóth, Tobias A. Knoch, Malte Wachsmuth, Monika Frank-Stöhr, Michael Stöhr, Christian P. Bacher, Gabriele Müller, and Karsten Rippe. Trichostatin A-induced histone acetylation causes decondensation of interphase chromatin. *Journal of Cell Science*, 117(18):4277–4287, August 2004.
- [126] Kevin J. Chalut, Markus Höpfler, Franziska Lautenschläger, Lars Boyde, Chii Jou Chan, Andrew Ekpenyong, Alfonso Martinez-Arias, and Jochen Guck. Chromatin Decondensation and Nuclear Softening Accompany Nanog Downregulation in Embryonic Stem Cells. *Biophysical Journal*, 103(10):2060–2070, November 2012.

- [127] Gabi Gerlitz and Michael Bustin. Efficient cell migration requires global chromatin condensation. *Journal of Cell Science*, 123(13):2207–2217, July 2010.
- [128] Andrew D. Stephens, Edward J. Banigan, Stephen A. Adam, Robert D. Goldman, and John F. Marko. Chromatin and lamin A determine two different mechanical response regimes of the cell nucleus. *Molecular Biology of the Cell*, 28(14):1984–1996, July 2017.
- [129] E.J.Th. Belt, R.J.A. Fijneman, E.G. Van Den Berg, H. Bril, P.M. Delis-van Diemen, M. Tijssen, H.F. Van Essen, E.S.M. De Lange-de Klerk, J.A.M. Beliën, H.B.A.C. Stockmann, S. Meijer, and G.A. Meijer. Loss of lamin A/C expression in stage II and III colon cancer is associated with disease recurrence. *European Journal of Cancer*, 47(12):1837–1845, August 2011.
- [130] Clare R. Foster, Stefan A. Przyborski, Robert G. Wilson, and Christopher J. Hutchison. Lamins as cancer biomarkers. *Biochemical Society Transactions*, 38(1):297–300, February 2010.
- [131] Amy C. Rowat, Diana E. Jaalouk, Monika Zwerger, W. Lloyd Ung, Irwin A. Eydelnant, Don E. Olins, Ada L. Olins, Harald Herrmann, David A. Weitz, and Jan Lammerding. Nuclear Envelope Composition Determines the Ability of Neutrophil-type Cells to Passage through Micron-scale Constrictions. *Journal of Biological Chemistry*, 288(12):8610–8618, March 2013. Publisher: Elsevier BV.
- [132] Gregg G. Gundersen and Howard J. Worman. Nuclear Positioning. *Cell*, 152(6):1376–1389, March 2013.
- [133] Melissa Crisp, Qian Liu, Kyle Roux, J.B. Rattner, Catherine Shanahan, Brian Burke, Phillip D. Stahl, and Didier Hodzic. Coupling of the nucleus and cytoplasm: Role of the LINC complex. *The Journal of Cell Biology*, 172(1):41–53, January 2006.
- [134] Mirjam Ketema, Maaïke Kreft, Pablo Secades, Hans Janssen, and Arnoud Sonnenberg. Nesprin-3 connects plectin and vimentin to the nuclear envelope of Sertoli cells but is not required for Sertoli cell function in spermatogenesis. *Molecular Biology of the Cell*, 24(15):2454–2466, August 2013.
- [135] Stefan Stöberl, Johannes Flommersfeld, Maximilian M. Kreft, Martin Benoit, Chase P. Broedersz, and Joachim O. Rädler. Nuclear deformation and dynamics of migrating cells in 3D confinement reveal adaptation of pulling and pushing forces. preprint, Biophysics, November 2023.
- [136] Jessica M. Stukel and Rebecca Kuntz Willits. Mechanotransduction of Neural Cells Through Cell–Substrate Interactions. *Tissue Engineering Part B: Reviews*, 22(3):173–182, June 2016.

- [137] LiKang Chin, Yuntao Xia, Dennis E Discher, and Paul A Janmey. Mechano-transduction in cancer. *Current Opinion in Chemical Engineering*, 11:77–84, February 2016.
- [138] Jenny Z. Kechagia, Johanna Ivaska, and Pere Roca-Cusachs. Integrins as biomechanical sensors of the microenvironment. *Nature Reviews Molecular Cell Biology*, 20(8):457–473, August 2019.
- [139] George T. Eisenhoffer, Patrick D. Loftus, Masaaki Yoshigi, Hideo Otsuna, Chi-Bin Chien, Paul A. Morcos, and Jody Rosenblatt. Crowding induces live cell extrusion to maintain homeostatic cell numbers in epithelia. *Nature*, 484(7395):546–549, April 2012.
- [140] Jörg Renkawitz, Aglaja Kopf, Julian Stopp, Ingrid De Vries, Meghan K. Driscoll, Jack Merrin, Robert Hauschild, Erik S. Welf, Gaudenz Danuser, Reto Fiolka, and Michael Sixt. Nuclear positioning facilitates amoeboid migration along the path of least resistance. *Nature*, 568(7753):546–550, April 2019.
- [141] Britta Trappmann, Julien E. Gautrot, John T. Connelly, Daniel G. T. Strange, Yuan Li, Michelle L. Oyen, Martien A. Cohen Stuart, Heike Boehm, Bojun Li, Viola Vogel, Joachim P. Spatz, Fiona M. Watt, and Wilhelm T. S. Huck. Extracellular-matrix tethering regulates stem-cell fate. *Nature Materials*, 11(7):642–649, July 2012.
- [142] Mathieu Pinot, Villier Steiner, Benoit Dehapiot, Byung-Kuk Yoo, Franck Chesnel, Laurent Blanchoin, Charles Kervrann, and Zoher Gueroui. Confinement induces actin flow in a meiotic cytoplasm. *Proceedings of the National Academy of Sciences*, 109(29):11705–11710, July 2012.
- [143] Michael D Vahey and Daniel A Fletcher. The biology of boundary conditions: cellular reconstitution in one, two, and three dimensions. *Current Opinion in Cell Biology*, 26:60–68, February 2014.
- [144] Jung-Hwan Lee, Dong-Hwee Kim, Hae-Hyoung Lee, and Hae-Won Kim. Role of nuclear mechanosensitivity in determining cellular responses to forces and biomaterials. *Biomaterials*, 197:60–71, March 2019.
- [145] Harvey M. Levy and Elizabeth M. Ryan. Evidence that Calcium activates the Contraction of Actomyosin by overcoming Substrate Inhibition. *Nature*, 205(4972):703–705, February 1965.
- [146] M. Raab, M. Gentili, H. de Belly, H.-R. Thiam, P. Vargas, A. J. Jimenez, F. Lautenschlaeger, R. Voituriez, A.-M. Lennon-Dumenil, N. Manel, and M. Piel. ESCRT III repairs nuclear envelope ruptures during cell migration to limit DNA damage and cell death. *Science*, 352(6283):359–362, March 2016. Publisher: American Association for the Advancement of Science (AAAS).
- [147] Julien Barthes, Hayriye Özçelik, Mathilde Hindié, Albana Ndreu-Halili, Anwarul Hasan, and Nihal Engin Vrana. Cell Microenvironment Engineering

- and Monitoring for Tissue Engineering and Regenerative Medicine: The Recent Advances. *BioMed Research International*, 2014:1–18, 2014.
- [148] Fergal J. O’Brien. Biomaterials & scaffolds for tissue engineering. *Materials Today*, 14(3):88–95, March 2011.
- [149] Huan Wang, Mark W. Tibbitt, Stephen J. Langer, Leslie A. Leinwand, and Kristi S. Anseth. Hydrogels preserve native phenotypes of valvular fibroblasts through an elasticity-regulated PI3K/AKT pathway. *Proceedings of the National Academy of Sciences*, 110(48):19336–19341, November 2013.
- [150] Chentian Zhang, Maria P. Barrios, Rhoda M. Alani, Mario Cabodi, and Joyce Y. Wong. A microfluidic Transwell to study chemotaxis. *Experimental Cell Research*, 342(2):159–165, March 2016. Publisher: Elsevier BV.
- [151] Andreia Ribeiro, Shelby Vargo, Elizabeth M. Powell, and Jennie B. Leach. Substrate Three-Dimensionality Induces Elemental Morphological Transformation of Sensory Neurons on a Physiologic Timescale. *Tissue Engineering Part A*, 18(1-2):93–102, January 2012.
- [152] Ryan J. Petrie, Núria Gavara, Richard S. Chadwick, and Kenneth M. Yamada. Nonpolarized signaling reveals two distinct modes of 3D cell migration. *Journal of Cell Biology*, 197(3):439–455, April 2012.
- [153] Miriam Dietrich, Hugo Le Roy, David B. Brückner, Hanna Engelke, Roman Zantl, Joachim O. Rädler, and Chase P. Broedersz. Guiding 3D cell migration in deformed synthetic hydrogel microstructures. *Soft Matter*, 14(15):2816–2826, 2018. Publisher: Royal Society of Chemistry (RSC).
- [154] Yansong Peng and Esak Lee. Microphysiological Systems for Cancer Immunotherapy Research and Development. *Advanced Biology*, page 2300077, July 2023.
- [155] Faezeh Koohestani, Andrea G. Braundmeier, Arash Mahdian, Jane Seo, JiaJia Bi, and Romana A. Nowak. Extracellular Matrix Collagen Alters Cell Proliferation and Cell Cycle Progression of Human Uterine Leiomyoma Smooth Muscle Cells. *PLoS ONE*, 8(9):e75844, September 2013.
- [156] Matthew T. Wolf, Christopher L. Dearth, Sonya B. Sonnenberg, Elizabeth G. Loba, and Stephen F. Badylak. Naturally derived and synthetic scaffolds for skeletal muscle reconstruction. *Advanced Drug Delivery Reviews*, 84:208–221, April 2015.
- [157] Steven R Caliarì and Jason A Burdick. A practical guide to hydrogels for cell culture. *Nature Methods*, 13(5):405–414, May 2016.

- [158] Doris Lam, Heather A. Enright, Sandra K.G. Peters, Monica L. Moya, David A. Soscia, Jose Cadena, Javier A. Alvarado, Kristen S. Kulp, Elizabeth K. Wheeler, and Nicholas O. Fischer. Optimizing cell encapsulation condition in ECM-Collagen I hydrogels to support 3D neuronal cultures. *Journal of Neuroscience Methods*, 329:108460, January 2020.
- [159] Rui Zhang, Min Ma, Xia-Hui Lin, Hua-Hua Liu, Jie Chen, Jun Chen, Dong-Mei Gao, Jie-Feng Cui, Zheng-Gang Ren, and Rong-Xin Chen. Extracellular matrix collagen I promotes the tumor progression of residual hepatocellular carcinoma after heat treatment. *BMC Cancer*, 18(1):901, December 2018.
- [160] Joseph M. Wallace, Qishui Chen, Ming Fang, Blake Erickson, Bradford G. Orr, and Mark M. Banaszak Holl. Type I Collagen Exists as a Distribution of Nanoscale Morphologies in Teeth, Bones, and Tendons. *Langmuir*, 26(10):7349–7354, May 2010.
- [161] David M. Reilly and Jennifer Lozano. Skin collagen through the lifestages: importance for skin health and beauty. *Plastic and Aesthetic Research*, 8:2, 2021.
- [162] Uyen N. Nguyen, Fei San Lee, Sydney M. Caparaso, Jack T. Leoni, Adan L. Redwine, and Rebecca A. Wachs. Type I collagen concentration affects neurite outgrowth of adult rat DRG explants by altering mechanical properties of hydrogels. *Journal of Biomaterials Science, Polymer Edition*, 35(2):164–189, January 2024.
- [163] Gabriel Benton, Hynda K. Kleinman, Jay George, and Irina Arnaoutova. Multiple uses of basement membrane-like matrix (BME/Matrigel) *in vitro* and *in vivo* with cancer cells. *International Journal of Cancer*, 128(8):1751–1757, April 2011.
- [164] Hynda K. Kleinman and George R. Martin. Matrigel: Basement membrane matrix with biological activity. *Seminars in Cancer Biology*, 15(5):378–386, October 2005.
- [165] Justin R. Tse and Adam J. Engler. Preparation of Hydrogel Substrates with Tunable Mechanical Properties. *Current Protocols in Cell Biology*, 47(1), June 2010. Publisher: Wiley.
- [166] Saahil Sheth, Era Jain, Amin Karadaghy, Sana Syed, Hunter Stevenson, and Silviya P. Zustiak. UV Dose Governs UV-Polymerized Polyacrylamide Hydrogel Modulus. *International Journal of Polymer Science*, 2017:1–9, 2017. Publisher: Hindawi Limited.
- [167] Cole A. DeForest and Kristi S. Anseth. Cytocompatible click-based hydrogels with dynamically tunable properties through orthogonal photoconjugation and photocleavage reactions. *Nature Chemistry*, 3(12):925–931, December 2011.

- [168] Jordan S. Miller, Colette J. Shen, Wesley R. Legant, Jan D. Baranski, Brandon L. Blakely, and Christopher S. Chen. Bioactive hydrogels made from step-growth derived PEG-peptide macromers. *Biomaterials*, 31(13):3736–3743, May 2010. Publisher: Elsevier BV.
- [169] Shan Jiang, Sha Liu, and Wenhao Feng. PVA hydrogel properties for biomedical application. *Journal of the Mechanical Behavior of Biomedical Materials*, 4(7):1228–1233, October 2011.
- [170] Jorge I. Daza Agudelo, María R. Ramirez, Eduardo R. Henquin, and Ignacio Rintoul. Modelling of swelling of PVA hydrogels considering non-ideal mixing behaviour of PVA and water. *Journal of Materials Chemistry B*, 7(25):4049–4054, 2019.
- [171] Shuaijiang Ma, Shiwei Wang, Qian Li, Yuting Leng, Lianhui Wang, and Guo-Hua Hu. A Novel Method for Preparing Poly(vinyl alcohol) Hydrogels: Preparation, Characterization, and Application. *Industrial & Engineering Chemistry Research*, 56(28):7971–7976, July 2017.
- [172] Jungwook Paek, Joseph W. Song, Ehsan Ban, Yuma Morimitsu, Chinedum O. Osuji, Vivek B. Shenoy, and Dan Dongeun Huh. Soft robotic constrictor for in vitro modeling of dynamic tissue compression. *Scientific Reports*, 11(1):16478, August 2021.
- [173] R. J. Pelham and Y.-l Wang. Cell locomotion and focal adhesions are regulated by substrate flexibility. *Proceedings of the National Academy of Sciences*, 94(25):13661–13665, December 1997. Publisher: Proceedings of the National Academy of Sciences.
- [174] Benedikt Sabass, Margaret L. Gardel, Clare M. Waterman, and Ulrich S. Schwarz. High Resolution Traction Force Microscopy Based on Experimental and Computational Advances. *Biophysical Journal*, 94(1):207–220, January 2008. Publisher: Elsevier BV.
- [175] Venkat Maruthamuthu, Benedikt Sabass, Ulrich S. Schwarz, and Margaret L. Gardel. Cell-ECM traction force modulates endogenous tension at cell-cell contacts. *Proceedings of the National Academy of Sciences*, 108(12):4708–4713, March 2011.
- [176] Margaret L. Gardel, Benedikt Sabass, Lin Ji, Gaudenz Danuser, Ulrich S. Schwarz, and Clare M. Waterman. Traction stress in focal adhesions correlates biphasically with actin retrograde flow speed. *The Journal of Cell Biology*, 183(6):999–1005, December 2008.
- [177] Nicolas Schierbaum, Johannes Rheinlaender, and Tilman E. Schäffer. Combined atomic force microscopy (AFM) and traction force microscopy (TFM) reveals a correlation between viscoelastic material properties and contractile prestress of living cells. *Soft Matter*, 15(8):1721–1729, 2019. Publisher: Royal Society of Chemistry (RSC).

- [178] Yu-li Wang and David Li. Creating Complex Polyacrylamide Hydrogel Structures Using 3D Printing with Applications to Mechanobiology. *Macromolecular Bioscience*, 20(7):2000082, July 2020.
- [179] Zhongliang Jiang, Bingzhao Xia, Ralph McBride, and John Oakey. A microfluidic-based cell encapsulation platform to achieve high long-term cell viability in photopolymerized PEGNB hydrogel microspheres. *Journal of Materials Chemistry B*, 5(1):173–180, 2017. Publisher: Royal Society of Chemistry (RSC).
- [180] Christine Wang, Xinming Tong, and Fan Yang. Bioengineered 3D Brain Tumor Model To Elucidate the Effects of Matrix Stiffness on Glioblastoma Cell Behavior Using PEG-Based Hydrogels. *Molecular Pharmaceutics*, 11(7):2115–2125, April 2014. Publisher: American Chemical Society (ACS).
- [181] Chien-Chi Lin, Asad Raza, and Han Shih. PEG hydrogels formed by thiol-ene photo-click chemistry and their effect on the formation and recovery of insulin-secreting cell spheroids. *Biomaterials*, 32(36):9685–9695, December 2011.
- [182] April M. Kloxin, Christopher J. Kloxin, Christopher N. Bowman, and Kristi S. Anseth. Mechanical Properties of Cellularly Responsive Hydrogels and Their Experimental Determination. *Advanced Materials*, 22(31):3484–3494, May 2010. Publisher: Wiley.
- [183] Stefan Stöberl, Miriam Balles, Thomas Kellerer, and Joachim O. Rädler. Photolithographic microfabrication of hydrogel clefts for cell invasion studies. *Lab on a Chip*, 23(7):1886–1895, 2023.
- [184] Matthew S. Rehmann, Kelsi M. Skeens, Prathamesh M. Kharkar, Eden M. Ford, Emanuel Maverakis, Kelvin H. Lee, and April M. Kloxin. Tuning and Predicting Mesh Size and Protein Release from Step Growth Hydrogels. *Biomacromolecules*, 18(10):3131–3142, October 2017.
- [185] Tiziana Canal and Nikolaos A. Peppas. Correlation between mesh size and equilibrium degree of swelling of polymeric networks. *Journal of Biomedical Materials Research*, 23(10):1183–1193, October 1989.
- [186] Eric M. Balzer, Ziqiu Tong, Colin D. Paul, Wei-Chien Hung, Kimberly M. Stroka, Amanda E. Boggs, Stuart S. Martin, and Konstantinos Konstantopoulos. Physical confinement alters tumor cell adhesion and migration phenotypes. *The FASEB Journal*, 26(10):4045–4056, June 2012. Publisher: Wiley.
- [187] Daniel Irimia, Guillaume Charras, Nitin Agrawal, Timothy Mitchison, and Mehmet Toner. Polar stimulation and constrained cell migration in microfluidic channels. *Lab on a Chip*, 7(12):1783, 2007. Publisher: Royal Society of Chemistry (RSC).
- [188] Amit Pathak and Sanjay Kumar. Independent regulation of tumor cell migration by matrix stiffness and confinement. *Proceedings of the National Academy*

- of Sciences*, 109(26):10334–10339, June 2012. Publisher: Proceedings of the National Academy of Sciences.
- [189] Pinar Zorlutuna, Jae Hyun Jeong, Hyunjoon Kong, and Rashid Bashir. Stereolithography-Based Hydrogel Microenvironments to Examine Cellular Interactions. *Advanced Functional Materials*, 21(19):3642–3651, October 2011.
- [190] Joseph C. Hoffmann and Jennifer L. West. Three-dimensional photolithographic micropatterning: a novel tool to probe the complexities of cell migration. *Integrative Biology*, 5(5):817, 2013.
- [191] Haoyi Yu, Haibo Ding, Qiming Zhang, Zhongze Gu, and Min Gu. Three-Dimensional Direct Laser Writing of PEGda Hydrogel Microstructures with Low Threshold Power using a Green Laser Beam. *Light: Advanced Manufacturing*, 2(1):31, 2021.
- [192] Maria Farsari and Boris N. Chichkov. Two-photon fabrication. *Nature Photonics*, 3(8):450–452, August 2009.
- [193] Adina I. Ciuciu and Piotr J. Cywiński. Two-photon polymerization of hydrogels – versatile solutions to fabricate well-defined 3D structures. *RSC Adv.*, 4(85):45504–45516, September 2014.
- [194] Robert Hooke. *De Potentia Restitutiva, or of Spring. Explaining the Power of Springing Bodies*. Martin John, London, 1678.
- [195] Isaac Newton. *Philosophiae Naturalis Principia Mathematica. Auctore Js. Newton ...* [object Object], 1687. Medium: S.[I-VI], 1-383, 400-510, [1] ; 26 cm : Ill., 1 Falttaf.
- [196] Z D Jastrzebski. *Nature and properties of engineering materials*. United States, 1976.
- [197] H. Gercek. Poisson’s ratio values for rocks. *International Journal of Rock Mechanics and Mining Sciences*, 44(1):1–13, January 2007.
- [198] Robert James Thomas Park. Seismic performance of steel-encased concrete piles. 1986. Publisher: [object Object].
- [199] Rod Lakes and K. W. Wojciechowski. Negative compressibility, negative Poisson’s ratio, and stability. *physica status solidi (b)*, 245(3):545–551, March 2008.
- [200] Z. Y. Wei, Z. V. Guo, L. Dudte, H. Y. Liang, and L. Mahadevan. Geometric Mechanics of Periodic Pleated Origami. *Physical Review Letters*, 110(21):215501, May 2013.
- [201] Valentin L. Popov. *Contact Mechanics and Friction*. Springer Berlin Heidelberg, Berlin, Heidelberg, 2010.

- [202] K. L. Johnson. *Contact Mechanics*. Cambridge University Press, 1 edition, May 1985.
- [203] Heinrich Hertz. Ueber die Berührung fester elastischer Körper. *crll*, 1882(92):156–171, 1882.
- [204] Emi Y. Tokuda, Jennifer L. Leight, and Kristi S. Anseth. Modulation of matrix elasticity with PEG hydrogels to study melanoma drug responsiveness. *Biomaterials*, 35(14):4310–4318, May 2014. Publisher: Elsevier BV.
- [205] Samir P. Singh, Michael P. Schwartz, Justin Y. Lee, Benjamin D. Fairbanks, and Kristi S. Anseth. A peptide functionalized poly(ethylene glycol) (PEG) hydrogel for investigating the influence of biochemical and biophysical matrix properties on tumor cell migration. *Biomaterials Science*, 2(7):1024, 2014. Publisher: Royal Society of Chemistry (RSC).
- [206] Charles\hspace0 25emE Hoyle and Christopher\hspace0 25emN Bowman. Thiol-Ene Click Chemistry. *Angewandte Chemie International Edition*, 49(9):1540–1573, February 2010. Publisher: Wiley.
- [207] Benjamin D. Fairbanks, Michael P. Schwartz, Christopher N. Bowman, and Kristi S. Anseth. Photoinitiated polymerization of PEG-diacrylate with lithium phenyl-2,4,6-trimethylbenzoylphosphinate: polymerization rate and cytocompatibility. *Biomaterials*, 30(35):6702–6707, December 2009. Publisher: Elsevier BV.
- [208] Paul J. Flory and John Rehner. Statistical Mechanics of Cross-Linked Polymer Networks II. Swelling. *The Journal of Chemical Physics*, 11(11):521–526, November 1943.
- [209] Paul J. Flory and John Rehner. Statistical Mechanics of Cross-Linked Polymer Networks II. Swelling. *The Journal of Chemical Physics*, 11(11):521–526, November 1943. Publisher: AIP Publishing.
- [210] Kurt Thorn. A quick guide to light microscopy in cell biology. *Molecular Biology of the Cell*, 27(2):219–222, January 2016.
- [211] C R Burch and J P P Stock. Phase-Contrast Microscopy. *Journal of Scientific Instruments*, 19(5):71–75, May 1942.
- [212] Donna J. Webb and Claire M. Brown. Epi-Fluorescence Microscopy. In Douglas J. Taatjes and Jürgen Roth, editors, *Cell Imaging Techniques*, volume 931, pages 29–59. Humana Press, Totowa, NJ, 2012. Series Title: Methods in Molecular Biology.
- [213] Gary Wnek and Gary Bowlin, editors. *Encyclopedia of Biomaterials and Biomedical Engineering*. CRC Press, 0 edition, May 2008.
- [214] G. Binnig, C. F. Quate, and Ch. Gerber. Atomic Force Microscope. *Physical Review Letters*, 56(9):930–933, March 1986.

- [215] Yang Gan. Atomic and subnanometer resolution in ambient conditions by atomic force microscopy. *Surface Science Reports*, 64(3):99–121, March 2009.
- [216] Sergey Belikov, John Alexander, Craig Wall, Ivan Yermolenko, Sergei Magonov, and Ivan Malovichko. Thermal tune method for AFM oscillatory resonant imaging in air and liquid. In *2014 American Control Conference*, pages 1009–1014, Portland, OR, USA, June 2014. IEEE.
- [217] M. Radmacher. Measuring the elastic properties of biological samples with the AFM. *IEEE Engineering in Medicine and Biology Magazine*, 16(2):47–57, March 1997.
- [218] Nicola Galvanetto. Single-cell unroofing: probing topology and nanomechanics of native membranes. *Biochimica et Biophysica Acta (BBA) - Biomembranes*, 1860(12):2532–2538, December 2018.
- [219] Lea Tomasova, Zeno Guttenberg, Bernd Hoffmann, and Rudolf Merkel. Advanced 2D/3D cell migration assay for faster evaluation of chemotaxis of slow-moving cells. *PLOS ONE*, 14(7):e0219708, July 2019.
- [220] Verena Biswenger, Nina Baumann, Johannes Jürschick, Martina Häckl, Christopher Battle, Jan Schwarz, Elias Horn, and Roman Zantl. Characterization of EGF-guided MDA-MB-231 cell chemotaxis in vitro using a physiological and highly sensitive assay system. *PLOS ONE*, 13(9):e0203040, September 2018. Publisher: Public Library of Science (PLoS).
- [221] G. P. Raeber, M. P. Lutolf, and J. A. Hubbell. Molecularly Engineered PEG Hydrogels: A Novel Model System for Proteolytically Mediated Cell Migration. *Biophysical Journal*, 89(2):1374–1388, August 2005. Publisher: Elsevier BV.
- [222] Manuel Quesada-Pérez, José Alberto Maroto-Centeno, Jacqueline Forcada, and Roque Hidalgo-Alvarez. Gel swelling theories: the classical formalism and recent approaches. *Soft Matter*, 7(22):10536, 2011. Publisher: Royal Society of Chemistry (RSC).
- [223] J. M. Tse, G. Cheng, J. A. Tyrrell, S. A. Wilcox-Adelman, Y. Boucher, R. K. Jain, and L. L. Munn. Mechanical compression drives cancer cells toward invasive phenotype. *Proceedings of the National Academy of Sciences*, 109(3):911–916, December 2011. Publisher: Proceedings of the National Academy of Sciences.
- [224] Katarina Wolf, Yi I. Wu, Yueying Liu, Jörg Geiger, Eric Tam, Christopher Overall, M. Sharon Stack, and Peter Friedl. Multi-step pericellular proteolysis controls the transition from individual to collective cancer cell invasion. *Nature Cell Biology*, 9(8):893–904, July 2007. Publisher: Springer Science and Business Media LLC.

- [225] M. BROWN, C. WALLACE, C. ANAMELECHI, E. CLERMONT, W. REICHERT, and G. TRUSKEY. The use of mild trypsinization conditions in the detachment of endothelial cells to promote subsequent endothelialization on synthetic surfaces. *Biomaterials*, 28(27):3928–3935, September 2007. Publisher: Elsevier BV.
- [226] Kristina Goetze. Lactate enhances motility of tumor cells and inhibits monocyte migration and cytokine release. *International Journal of Oncology*, May 2011. Publisher: Spandidos Publications.
- [227] Erwin Berthier, Jill Surfus, James Verbsky, Anna Huttenlocher, and David Beebe. An arrayed high-content chemotaxis assay for patient diagnosis. *Integrative Biology*, 2(11-12):630–638, October 2010. Publisher: Oxford University Press (OUP).
- [228] David B. Brückner, Pierre Ronceray, and Chase P. Broedersz. Inferring the Dynamics of Underdamped Stochastic Systems. *Physical Review Letters*, 125(5):058103, July 2020.
- [229] Marina Krause, Feng Wei Yang, Mariska te Lindert, Philipp Isermann, Jan Schepens, Ralph J. A. Maas, Chandrasekhar Venkataraman, Jan Lammerding, Anotida Madzvamuse, Wiljan Hendriks, Joost te Riet, and Katarina Wolf. Cell migration through three-dimensional confining pores: speed accelerations by deformation and recoil of the nucleus. *Philosophical Transactions of the Royal Society B: Biological Sciences*, 374(1779):20180225, July 2019. Publisher: The Royal Society.
- [230] Katharina Siemsen, Sunil Rajput, Florian Rasch, Fereydoon Taheri, Rainer Adelung, Jan Lammerding, and Christine Selhuber-Unkel. Tunable 3D Hydrogel Microchannel Networks to Study Confined Mammalian Cell Migration. *Advanced Healthcare Materials*, 10(23):2100625, December 2021.
- [231] Özlem Ertekin, Mahshid Monavari, René Krüger, Miguel Fuentes-Chandía, Beatrice Parma, Gaelle Letort, Philipp Tripal, Aldo R. Boccaccini, Anja K. Bosserhoff, Paolo Ceppi, Melanie Kappelmann-Fenzl, and Aldo Leal-Egaña. 3D hydrogel-based microcapsules as an in vitro model to study tumorigenicity, cell migration and drug resistance. *Acta Biomaterialia*, 142:208–220, April 2022.
- [232] Jerome Irianto, Yuntao Xia, Charlotte R. Pfeifer, Avathamsa Athirasala, Jiazheng Ji, Cory Alvey, Manu Tewari, Rachel R. Bennett, Shane M. Harding, Andrea J. Liu, Roger A. Greenberg, and Dennis E. Discher. DNA Damage Follows Repair Factor Depletion and Portends Genome Variation in Cancer Cells after Pore Migration. *Current Biology*, 27(2):210–223, January 2017. Publisher: Elsevier BV.
- [233] Bin Sheng Wong, Sagar R. Shah, Christopher L. Yankaskas, Vivek K. Bajpai, Pei-Hsun Wu, Deborah Chin, Brent Ifemembi, Karim ReFaey, Paula Schiap-

- parelli, Xiaobin Zheng, Stuart S. Martin, Chen-Ming Fan, Alfredo Quiñones-Hinojosa, and Konstantinos Konstantopoulos. A microfluidic cell-migration assay for the prediction of progression-free survival and recurrence time of patients with glioblastoma. *Nature Biomedical Engineering*, 5(1):26–40, September 2020.
- [234] H K Kleinman, R J Klebe, and G R Martin. Role of collagenous matrices in the adhesion and growth of cells. *The Journal of cell biology*, 88(3):473–485, March 1981.
- [235] Qing Luo, Dongdong Kuang, Bingyu Zhang, and Guanbin Song. Cell stiffness determined by atomic force microscopy and its correlation with cell motility. *Biochimica et Biophysica Acta (BBA) - General Subjects*, 1860(9):1953–1960, September 2016.
- [236] Oren Wintner, Nivi Hirsch-Attas, Miriam Schlossberg, Fani Brofman, Roy Friedman, Meital Kupervaser, Danny Kitsberg, and Amnon Buxboim. A Unified Linear Viscoelastic Model of the Cell Nucleus Defines the Mechanical Contributions of Lamins and Chromatin. *Advanced Science*, 7(8):1901222, April 2020.
- [237] Xian Wang, Haijiao Liu, Min Zhu, Changhong Cao, Zhensong Xu, Yonit Tsatskis, Kimberly Lau, Chikin Kuok, Tobin Filleter, Helen McNeill, Craig A. Simmons, Sevan Hopyan, and Yu Sun. Mechanical stability of the cell nucleus: roles played by the cytoskeleton in nuclear deformation and strain recovery. *Journal of Cell Science*, page jcs.209627, January 2018.
- [238] Jerry S.H. Lee, Christopher M. Hale, Porntula Panorchan, Shyam B. Khatau, Jerry P. George, Yiider Tseng, Colin L. Stewart, Didier Hodzic, and Denis Wirtz. Nuclear Lamin A/C Deficiency Induces Defects in Cell Mechanics, Polarization, and Migration. *Biophysical Journal*, 93(7):2542–2552, October 2007.
- [239] Daniel B. Allan, Thomas Caswell, Nathan C. Keim, Casper M. van der Wel, and Ruben W. Verweij. soft-matter/trackpy: v0.6.2, February 2024.
- [240] Thwaite E. Puttock, M. *Elastic compression of spheres and cylinders at point and line contact*. Commonwealth Scientific and Industrial Research Organization Melbourne, 1969.
- [241] Paul Jorgensen, Nicholas P. Edgington, Brandt L. Schneider, Ivan Rupeš, Mike Tyers, and Bruce Futcher. The Size of the Nucleus Increases as Yeast Cells Grow. *Molecular Biology of the Cell*, 18(9):3523–3532, September 2007.
- [242] Helena Cantwell and Paul Nurse. Unravelling nuclear size control. *Current Genetics*, 65(6):1281–1285, December 2019.
- [243] Kazuhiro Maeshima, Haruki Iino, Saera Hihara, and Naoko Imamoto. Nuclear size, nuclear pore number and cell cycle. *Nucleus*, 2(2):113–118, March 2011.

- [244] Dan Deviri and Samuel A. Safran. Balance of osmotic pressures determines the nuclear-to-cytoplasmic volume ratio of the cell. *Proceedings of the National Academy of Sciences*, 119(21):e2118301119, May 2022.
- [245] Hawa-Racine Thiam, Pablo Vargas, Nicolas Carpi, Carolina Lage Crespo, Matthew Raab, Emmanuel Terriac, Megan C. King, Jordan Jacobelli, Arthur S. Alberts, Theresia Stradal, Ana-Maria Lennon-Dumenil, and Matthieu Piel. Perinuclear Arp2/3-driven actin polymerization enables nuclear deformation to facilitate cell migration through complex environments. *Nature Communications*, 7(1), March 2016. Publisher: Springer Science and Business Media LLC.
- [246] Carmela Rianna, Manfred Radmacher, and Sanjay Kumar. Direct evidence that tumor cells soften when navigating confined spaces. *Molecular Biology of the Cell*, 31(16):1726–1734, July 2020. Publisher: American Society for Cell Biology (ASCB).
- [247] Lifshitz E. M. Landau L. D. *Theory of Elasticity*, volume 7. Elsevier, 1986.
- [248] Hencky H. Über die Form es Elastizitätsgesetzes bei ideal elastischen Stoffen. pages 215–220, 1928.
- [249] Ruth Jinfen Chai, Hendrikje Werner, Peter Yiqing Li, Yin Loon Lee, Khaing Thet Nyein, Irina Solovei, Tuan Danh Anh Luu, Bhavya Sharma, Raju Navasankari, Martina Maric, Lois Yu En Sim, Ying Jie Loh, Edita Aliwarga, Jason Wen Long Cheong, Alexandre Chojnowski, Matias Ilmari Autio, Yu Haiyang, Kenneth Kian Boon Tan, Choong Tat Keng, Shi Ling Ng, Wei Leong Chew, Michael Ferenczi, Brian Burke, Roger Sik Yin Foo, and Colin L. Stewart. Disrupting the LINC complex by AAV mediated gene transduction prevents progression of Lamin induced cardiomyopathy. *Nature Communications*, 12(1):4722, August 2021.
- [250] Kirsi Riento and Anne J. Ridley. ROCKs: multifunctional kinases in cell behaviour. *Nature Reviews Molecular Cell Biology*, 4(6):446–456, June 2003.
- [251] Dana M. Pirone, Wendy F. Liu, Sami Alom Ruiz, Lin Gao, Srivatsan Raghavan, Christopher A. Lemmon, Lewis H. Romer, and Christopher S. Chen. An inhibitory role for FAK in regulating proliferation: a link between limited adhesion and RhoA-ROCK signaling. *The Journal of Cell Biology*, 174(2):277–288, July 2006.
- [252] Olivier Pertz. Spatio-temporal Rho GTPase signaling – where are we now? *Journal of Cell Science*, 123(11):1841–1850, June 2010.
- [253] Kazuhito Ichikawa, Katsuya Hirano, Masaaki Ito, Junko Tanaka, Takeshi Nakano, and David J. Hartshorne. Interactions and Properties of Smooth Muscle Myosin Phosphatase. *Biochemistry*, 35(20):6313–6320, January 1996.

- [254] Frank V. Brozovich. Myosin Light Chain Phosphatase: It Gets Around. *Circulation Research*, 90(5):500–502, March 2002.
- [255] Paul R. Andreassen, Françoise B. Lacroix, Emma Villa-Moruzzi, and Robert L. Margolis. Differential Subcellular Localization of Protein Phosphatase-1, 1, and Isoforms during Both Interphase and Mitosis in Mammalian Cells. *The Journal of Cell Biology*, 141(5):1207–1215, June 1998.
- [256] Maja Holy and David L. Brautigan. Calyculin A from *Discodermia calyx* Is a Dual Action Toxin that Blocks Calcium Influx and Inhibits Protein Ser/Thr Phosphatases. *Toxins*, 4(10):940–954, October 2012.
- [257] Lynn Chartier, Lucinda L. Rankin, Ronald E. Allen, Yuko Kato, Nobuhiro Fusetani, Hideaki Karaki, Shugo Watabe, and David J. Hartshorne. Calyculin-A increases the level of protein phosphorylation and changes the shape of 3T3 fibroblasts. *Cell Motility*, 18(1):26–40, January 1991.
- [258] Lynda J. Peterson, Zenon Rajfur, Amy S. Maddox, Christopher D. Freel, Yun Chen, Magnus Edlund, Carol Otey, and Keith Burridge. Simultaneous Stretching and Contraction of Stress Fibers In Vivo. *Molecular Biology of the Cell*, 15(7):3497–3508, July 2004.
- [259] Lisa A. Flanagan, Yo-El Ju, Beatrice Marg, Miriam Osterfield, and Paul A. Janmey. Neurite branching on deformable substrates. *NeuroReport*, 13(18):2411–2415, December 2002.
- [260] J. David Pajerowski, Kris Noel Dahl, Franklin L. Zhong, Paul J. Sammak, and Dennis E. Discher. Physical plasticity of the nucleus in stem cell differentiation. *Proceedings of the National Academy of Sciences*, 104(40):15619–15624, October 2007.
- [261] Andrew W. Holle, Neethu Govindan Kutty Devi, Kim Clar, Anthony Fan, Taher Saif, Ralf Kemkemer, and Joachim P. Spatz. Cancer Cells Invade Confined Microchannels via a Self-Directed Mesenchymal-to-Amoeboid Transition. *Nano Letters*, 19(4):2280–2290, February 2019. Publisher: American Chemical Society (ACS).

Danksagung

Ich möchte mich bei allen herzlich bedanken, die zur Entstehung dieser Arbeit beigetragen haben und mich in all den Jahren begleitet und unterstützt haben:

Ein großes Dankeschön geht an **Prof. Dr. Joachim Rädler** für seine Betreuung während meiner Doktorarbeit und die Möglichkeit, sie an seinem Lehrstuhl anzufertigen. Das mir entgegengebrachte Vertrauen und die gewährten Freiheiten haben es mir ermöglicht, die Projekte eigenständig mitzugestalten. Die unzähligen Kommentare und Diskussionen während unserer Projektbesprechungen waren äußerst wertvoll und regten stets zum Weiterdenken an.

Desweiteren möchte ich mich bei **Prof. Dr. Chase Broedersz** bedanken, der nicht nur die Zweitkorrektur meiner Arbeit übernimmt, sondern auch durch unsere sehr spannende Kollaboration maßgeblich zum Erfolg dieser Arbeit beigetragen hat.

Meinem theoretischen 'Gegenstück' **Johannes Flommersfeld**, ohne dem die Arbeit in etwa halb so interessant geworden wäre. Ich möchte mich bei Dir ganz herzlich für die unzähligen Zoom-Meetings und Deine stetige Bereitschaft für unser Projekt bedanken. Unsere Kollaboration hat meine Zeit über die Doktorarbeit fachlich und persönlich sehr bereichert. Und lass Dir gesagt sein, eine Schachpartie steht noch aus!

Dem gesamten **Lehrstuhl Rädler** möchte ich für die sehr angenehme Atmosphäre danken. Besonders die Aufenthalte in Antholz, die Wandertage und die Weihnachtsfeiern waren Highlights. Dank zahlreicher interessanter "Lunch-Seminare", "Coffee-Seminare" und "After-Tea-Seminare" ist auch die Wissenschaft nicht zu kurz gekommen.

Ein besonderer Dank geht an **Gerlinde Schwake**, für die immense Hilfe sowohl im Labor, aber auch auf menschlicher Ebene. Die Zeiten angefangen von "Stöberls Knochen" über "Best Day Ever" bis hin zu den späten Abendsessions während den Revisionmessungen werde ich nicht vergessen. Frau Schwake, es war mir ein innerliches Blumenpflücken!

Ein großes Dankeschön an **Charlott Leu** für den Support aus dem Reinraum und die Projektdiskussionen mit obligatorischem Kaffee.

Ein großer Dank auch an **Emily Brieger** für die ausführlichen Formel 1 Diskussionen mit stetigem Blick auf den entsprechenden Kalender. Auch das glühende Slack während der gemeinsamen Leidenszeit beim Schreiben der Doktorarbeit hat es etwas erträglicher gemacht.

Einen herzlichen Dank an die Kellerkinder **Nathalie Schäffler** und **Judith Müller**, für die sehr angenehme Zeit im Büro sowie die unzähligen konsumierten Kannen Kaffee. Es war immer eine Freude, ins Büro zu kommen, was ich teilweise auch ohne praktische Arbeiten im Labor getan habe.

Vielen Dank auch an **Johannes Heyn** für die geteilten Räumlichkeiten während unseren Konferenzausflügen. Danke, dass Du meine nächtlichen Schnarcheinheiten ertragen hast. Richte bitte bei Gelegenheit unserem Freund Peter Peperoni noch liebe Grüße aus.

Herzlichen Dank an meine Korrekturleser, bei denen ich, neben den bereits erwähnten Personen, besonders **Chris Sikeler** hervorheben möchte. Ohne euch würde wohl noch so mancher Fehler in der Arbeit stecken.

Allen meinen Freunden, die in der Freizeit für den nötigen Ausgleich gesorgt haben.

Meiner gesamten Familie für die immerwährende Unterstützung in allen Bereichen meines Lebens. Besonders erwähnen möchte ich hierbei meine **Oma**, welche für mich eine große Bereicherung und Inspiration ist!

Und natürlich noch einen besonderen Dank an **Bina**, welche so manche Höhen und Tiefen in den letzten Jahren anhören durfte. Sehr schön, dass es Dich gibt!